Spectroscopic Study of Localized States in Twisted Semiconducting Heterostructures and Charge Transfer Driven Phenomena in α-$RuCl_3$ Heterointerfaces

Sara Shabani

Submitted in partial fulfillment of the
requirements for the degree of
Doctor of Philosophy
under the Executive Committee
of the Graduate School of Arts and Sciences

COLUMBIA UNIVERSITY

2023

© 2023

Sara Shabani

All Rights Reserved

Abstract

Spectroscopic Study of Localized States in Twisted Semiconducting Heterostructures and Charge Transfer Driven Phenomena in α-$RuCl_3$ Heterointerfaces

Sara Shabani

This thesis investigates the unique properties of 2D devices such as twisted semiconducting bilayers and α-$RuCl_3$ heterostructures employing scanning tunneling microscopy (STM) and spectroscopy (STS) probes. The research presented here sheds light on the vast opportunities that 2D materials provide in condensed matter systems as well as future device applications. Among 2D materials, transition metal dichalcogenide (TMD) heterobilayers provide a promising platform to study many quantum phenomena such as excitonic states due to their tunability of band gap. In addition, TMDs are excellent candidates to achieve localized states and carrier confinement, crucial for single photon emitters used in quantum computation and information. We begin this thesis with a brief overview of STM/STS and utilizing these techniques on 2D materials in the first and second chapters. The third chapter of this work investigates the twisted bilayer of WSe_2 and $MoSe_2$ in the H-stacking configuration using STM/STS which was previously challenging to measure. The spectroscopic results obtained from the heterobilayer indicate that a combination of

structural rippling and electronic coupling generates unexpectedly large moiré potentials, in the range of several hundred meV. Our analysis reveals that the moiré structure and internal strain, rather than interlayer coupling, are the main factors of the moiré potential. Large moiré potentials lead to deeply trapped carriers such as electron-hole pairs, so-called excitons. Our findings open new routes toward investigating excitonic states in twisted TMDs.

In the next chapter, we investigate the ultralocalized states of twisted $WSe_2/MoSe_2$ nanobubbles. Mechanical and electrical nanostructurings are expected to modify the band properties of transition metal dichalcogenides at the nanoscale. To visualize this effect, we use STM and near-field photoluminescence to examine the electronic and optical properties of nanobubbles in the semiconducting heterostructures. Our findings reveal a significant change in the local bandgap at the nanobubble, with a continuous evolution towards the edge of the bubble. Moreover, at the edge of the nanobubble, we show the formation of in gap bound states. A continuous redshift of the interlayer exciton on entering the bubble is also detected by the nano-PL. Using self-consistent Schrodinger-Poisson simulations, we further show that strong doping in the bubble region leading to band bending is responsible for achieving ultralocalized states. Overall, this work demonstrates the potential of 2D TMDs for developing well-controlled optical emitters for quantum technologies and photonics.

We next turn to the effect of the electric field in band gap tuning of WSe_2/WS_2 heterobilayer. Tunability of band gap is a crucial element in device engineering to achieve quantum emitters. The electrostatic gate generates doping and an electric field giving access to continuous tunability, higher doping level, and integration capability to nanoelectronic devices. We employ scanning tunneling microscopy (STM) and spectroscopy (STS) to probe the band properties of twisted heterobilayer with high energy and spatial resolution. We observe continuous band gap tuning up to several hundreds of meV change by sweeping the back gate. We introduced a capacitance model to take into account the finite tip size leading to an enhanced electric field. The result of our calculation captures well the band gap change observed by STS measurements. Our study offers a new route toward creating highly tunable semiconductors for carrier confinement in

quantum technology.

In the next chapters, we focus on α-$RuCl_3$ heterointerfaces. We first explore the nanobubble of graphene/α-$RuCl_3$ to create sharp p-n junctions. The ability to create sharp lateral p-n junctions is a critical requirement for the observation of numerous quantum phenomena. To accomplish this, we used a charge-transfer based heterostructure consisting of graphene and α-$RuCl_3$ to create nanoscale lateral p-n junctions in the vicinity of nanobubbles. Our approach relied on a combination of scanning tunneling microscopy (STM) and spectroscopy (STS), as well as scattering-type scanning near-field optical microscopy (s-SNOM), which allowed us to examine both the electronic and optical responses of these nanobubble p-n junctions. Our results showed a massive doping variation across the nanobubble with a band offset of 0.6 eV. Further, we observe the formation of an abrupt junction along nanobubble boundaries with an exceptionally sharp lateral width (<3 nm). This is one order of magnitude smaller length scale than previous lithographic methods. Our work paves the way toward device engineering via interfacial charge transfer in graphene and other low-density 2D materials.

In chapter 7, we describe the use of low-temperature scanning tunneling microscopy (STM) measurements to observe the moiré pattern in graphene/α-$RuCl_3$ heterostructure to validate the InterMatch method. This method is effective in predicting the charge transfer, strain, and stability of an interface. The InterMatch method was applied to moire patterns of graphene/α-$RuCl_3$ to predict the stable interface structure. STM topographs show three regions with distinct moire wavelengths due to atomic reconstructions. Using the InterMatch method, we perform a comprehensive mapping of the space of superlattice configurations and we identify the energetically favorable superlattices that occur in a small range of twist angles. This range is consistent with the STM results. Moreover, the spectra on these regions exhibit strong resonances with the spacing between resonances following the expectation from Landau levels on a Dirac spectrum due to strain and doping. The results of our scanning tunneling microscopy (STM) measurements confirm that the InterMatch method is effective in predicting the charge transfer and stability of interfaces between materials.

We next investigate WSe_2/α-$RuCl_3$ heterostructure through a multi-faceted approach. Our exploration encompassed diverse techniques such as STM, optical measurements. We detect a significant charge transfer between the two layers by STM measurements, leading to a shift in the Fermi level towards the valence band of WSe_2. Our findings are supported by optical measurements and DFT calculations, which confirm the p-doped WSe_2 observed through STM. The results of this work highlight α-$RuCl_3$ potential for contact engineering of TMDs and unlocking their functionalities for the next generation optoelectronic devices.

In the last chapter of this thesis, I provide a brief conclusion as well as a few future directions and insights for investigating 2D materials.

Table of Contents

List of Figures

List of Tables

Acknowledgements

The PhD journey was full of surprises and joys for me. This journey helped me to grow not only as a researcher but also as a person. It shaped my character to become resilient and proactive in learning. It all began five years ago when I moved from Iran to the United States to pursue my degree, filled with fear of uncertainty but also with hope for the future. I was full of excitement to learn from the pioneers of condensed matter and conduct cutting-edge research. My dream had come true and I was at Columbia, however, I soon realized that scientific research comes with its own share of challenges and triumphs. I could not have successfully navigated this path without the guidance and support of great mentors along the way. I am incredibly appreciative of every moment I spent in the physics department at Columbia and of everyone who showed me care and support during this time.

This journey would have not been possible without the invaluable support and guidance from my PhD advisor, Professor Abhay Pasupathy. He is a brilliant scientist and his patience with the students is remarkable. He has always taken the time to listen to my concerns and provide thoughtful advice, both professionally and personally. I am very grateful for his mentorship, which has been crucial in shaping my academic and personal growth. I appreciate the countless hours Abhay spent with me discussing physics and new ideas as well as showing me how to think like a scientist. When I faced any difficulty in projects, he reminded me that it would have not been interesting physics, if we already knew the solution and that kept me motivated to move forward and dig into it. He always encouraged me to explore new ideas, to challenge assumptions, and to think simply about complex problems. I would like to express my gratitude

to him for always pushing me to do my best, for challenging me to think deeply about science, and for providing me with endless opportunities to learn and grow both academically and personally throughout my PhD. Abhay, I feel incredibly lucky to have you as my mentor, and I will carry the lessons you have taught me with me for the rest of my life.

I would like to thank Professor Dmitri Basov who showed great support during my PhD. His expertise in the field and willingness to share his knowledge and insights have been invaluable in shaping my research and helping me achieve my goals. His positive attitude and constant encouragement have made my journey more memorable. I am deeply grateful for his mentorship and the time and effort he has invested in me. His influence has left a lasting impact, and I am honored to have had the opportunity to learn from him. I am confident that the skills and knowledge I gained under his mentorship will be invaluable to me in my future career.

I would like to express my appreciation to Professor James Schuck for being so supportive throughout the projects. His expertise and genuine enthusiasm to the projects were inspirational to me to move forward with research. I am deeply thankful for all the fruitful and engaging discussions we had together. I am very grateful for his invaluable insights and guidance.

I would like to thank Professor Xiaoyang Zhu for his invaluable expertise, guidance, and insights during my research projects. Professor Zhu's vast knowledge and experience in the field were crucial in my successful completion of these projects. Collaborating with his team was an enjoyable experience that led to multiple papers. I am thankful for his constant encouragement and motivation.

I would like to express my sincere gratitude to my parents, Azam and Ali, for their love, support, and encouragement throughout my academic journey. Their belief in my abilities and their willingness to sacrifice to help me achieve my goals. They provided me with the resources, both financial and emotional, to pursue my dreams and begin my journey at Columbia. The sacrifices my parents have made for me over these years cannot be overstated. Due to special circumstances, I was unable to see my parents during the last 5 years and it was an extremely difficult period of time for them. Their selflessness and dedication to my success have been a

source of inspiration for me, and I am forever grateful for their love and support. I am immensely grateful to my father for showing me to dream big, work hard, and never give up. In moments of disappointment, he provided me with invaluable guidance on how to approach obstacles with a fresh perspective and encouraged me to push harder to overcome them. I owe everything I have achieved in my academic and personal life to my parents' guidance and support.

Through the ups and downs of my academic journey, my brother, Javad, has been my rock. He is a wonderful person, a brilliant scientist, and an extraordinary mentor who has had the most significant influence on my personal and professional growth from a young age. I am deeply grateful for his presence in my life. He has been an essential source of support, providing me with the guidance and motivation I needed to achieve my goals throughout my life. Whenever I felt overwhelmed, he was always there to listen to me and offer practical advice. His belief in me has given me the confidence to overcome even the most significant obstacles. His mentorship has been invaluable to me and I could not have achieved any milestone in my life without his support. I also appreciate my sister's constant support and encouragement during my program. I am deeply grateful to her for always being there for me.

I would like to thank Qianhui Shi for investing countless hours in the lab teaching me how to approach condensed matter problems and measurements. She has been a source of inspiration to me. Her mentorship not only taught me how to tackle scientific problems but also gave me the confidence to actively participate in academic discussions. Qianhui's dedication, expertise, and passion for science have had a profound impact on my research journey. I am deeply grateful for her guidance and support.

I would like to thank Mitali Banerjee for being an outstanding mentor through my PhD study. She is a brilliant scientist and wonderful person. She was always there to encourage me to push forward when I was facing difficulties. She provided me with the big picture of research and that kept me motivated to focus on the main goals and move forward. I am very grateful for her invaluable guidance.

I would like to thank all of my colleagues and friends in the lab who made this journey fun

and enjoyable for me. We shared so many moments together in the lab; working on different projects, fixing tools, and discussing different topics. Thank you Carmen Rubio-Verdu, Alexander Kerelskey, Eric Seewald, Augusto Ghiotto, Minghao Cheng, Daniel Rhodes, Simon Turkel, Apoorv Jindal, Aya Tazi, Giancarlo Pereira, Madisen Holbrook, Mark Ziffer, Morgan Thinel, Tatiana Webb, Tom Darlington, Xuehao Wu, Yuan Song, Xiong Huang. I feel so fortunate to learn from your knowledge and work with you during my program.

I am also grateful to my colleagues and collaborators for their valuable feedback and insights throughout the PhD, which helped to shape and refine my ideas. Thank you Daniel Rizzo, Daniel Rohdes, Song Liu, Enmin Shih, and Wenjing Wu. Your willingness to engage in meaningful discussions and provide constructive feedback was invaluable and greatly contributed to the quality of this work.

I am also very thankful to all my friends I have made at Columbia. Thank you Ioanna Kourkoulou, Adam Williams, Emily Tiberi, Colin Adams, Barbara Cruvinel, Elena Busch, Valerie Hsieh, Anjaly Thekkevi and Jordan Pack.

I would like to take this opportunity to express my endless gratitude to my Persian friends, who have been an important part of my life through PhD days and have supported me in numerous ways on difficult days away from my home country.

I would like to thank all the friends and colleagues who may not be mentioned by name, but who have played an important role in making this journey more enjoyable and memorable for me. Your presence has been invaluable, and I am grateful to have you in my life.

Dedication

To women who have not had the opportunity to enjoy the beauty of science

Chapter 1: Introduction to Scanning Tunneling Microscopy

The Nobel Prize in Physics was awarded to Gerd Binnig and Heinrich Rohrer in 1986 for their invention of scanning tunneling microscopy (STM). STM is a powerful technique to study the structural and electronic properties of a wide range of materials including metals, semiconductors, and superconductors. With the advent of 2D materials by discovering graphene in 2004[1], new opportunities to study numerous quantum phenomena have been unlocked[2, 3, 4]. Understanding the emergent physics and developing the next generation of optoelectronic devices both require a thorough characterization of 2D materials. Among the existing characterization probes, STM stands out as a powerful approach for exploring material properties such as strongly correlated states due to high spatial and energy resolution. To fully utilize the functionalities of STM for investigating novel physics, it is essential to comprehend its principles of operation. This chapter provides a brief overview of STM principles. I will begin by discussing the fundamental theory of STM, the quantum tunneling effect, and the tunneling current equation. The chapter then proceeds to introduce two unique modes of STM: topography and spectroscopy, both of which rely on the tunneling current theory. Additionally, the chapter elaborates on the three types of spectroscopy extensively utilized in this thesis. Finally, the chapter provides an overview of the experimental setup and operation.

1.1 Theory: Tunneling Effect

Scanning tunneling microscopy relies on the quantum phenomenon of particle tunneling through a region that is considered classically forbidden. This chapter begins with an overview of the single-particle concept of the tunneling effect and subsequently presents a more precise model of the tunneling current utilized in STM. According to quantum mechanics, a particle can transmit or

tunnel through a potential barrier even when the kinetic energy is lower than the potential energy. The wave function of the particle, $\psi(x)$, is derived in an exponential form as the solution of the Schrodinger equation as the following[5].

$$\psi(x) \propto e^{-kx} \tag{1.1}$$

$$k = \sqrt{\frac{2m(U-E)}{\hbar}} \tag{1.2}$$

Here x is defined as the particle position inside the barrier, U is the potential energy barrier, E is the particle energy, m is the mass of the particle and $\hbar$ is the reduced Planck's constant. Equation 1.1 shows that the probability, $|\psi^2(x)|$, of finding the particle inside the potential barrier is non-zero and decays exponentially. It is important to note that if the potential energy barrier is smaller than the energy in Equation 1.2, a classical transmission is taking place. In this scenario, k will be imaginary, and the wave function will change to sinusoidal. Figure 1.1a shows a schematic of a rectangular potential energy barrier as a classically forbidden region. The boundary conditions at the edge of the barrier must be applied to the wave function so that the wave function and its derivative are continuous across the entire region. The particle is approaching from the left side of the barrier with a sinusoidal wave function and has a non-zero probability of penetration through the barrier. On the far side of the barrier, the particle continues its travel.

Equation 1.1 is a simplified single-particle view of the tunneling effect. However, in the STM setup, a sharp metallic tip containing many electrons is brought close to a conducting surface and the single particle picture no longer adequately describes the tunneling current of the STM tip. To address this issue, we first consider two metal plates separated by a thin layer of insulator. In this case, the potential energy barrier is determined by the work function difference between the two metal plates. Work function is the energy needed to remove one electron from the metallic surface. However, a voltage bias between two plates (far less than the work functions) is necessary for electron tunneling in a specific direction. In addition, detecting the tunneling current requires a thin insulating layer (<1 nm) between the metal probe and the sample. Figure 1.1b demonstrates

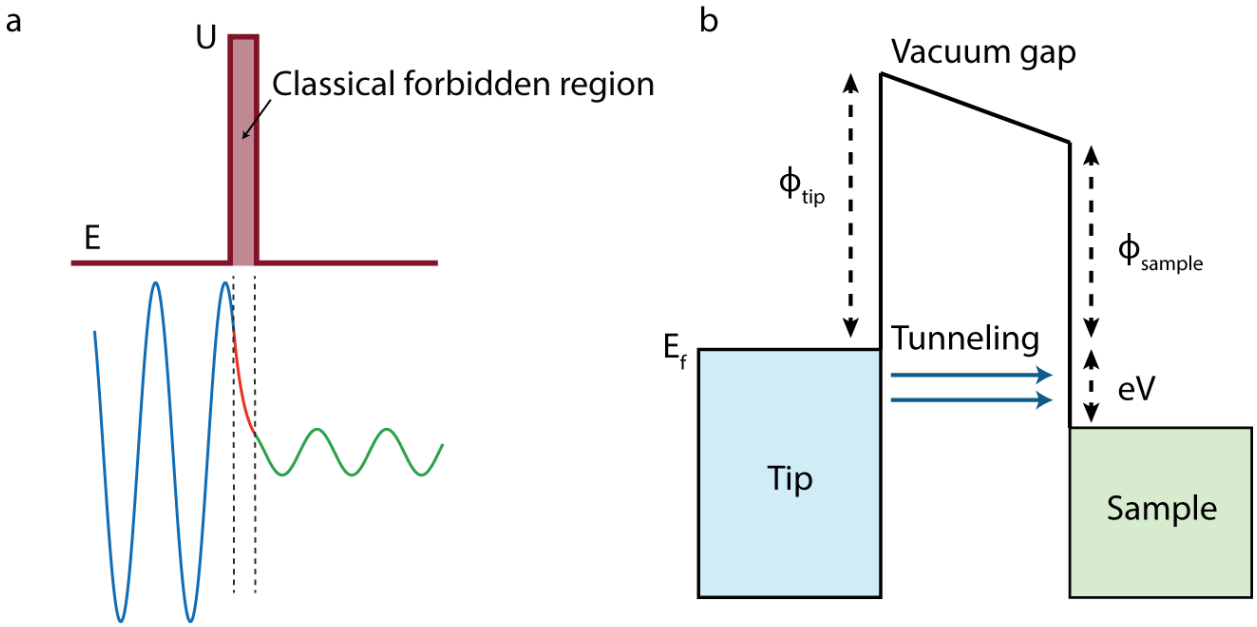

Figure 1.1: **a** The penetration of particle through a potential barrier, classically forbidden region. The probability of finding the particle inside the barrier decays exponentially. **a** The tunneling mechanism between the tip and the sample by applying a voltage bias

the tunneling effect between the tip and the sample in a vacuum. In the absence of a voltage bias, the Fermi level of both tip and sample align and the current becomes zero. This figure provides a simple picture of the tunneling current between two metal plates. In order to make this picture closer to the STM setup, the probe plate needs to be replaced with a sharp metallic tip. Resulting of this modification, a more complete model to describe the tunneling current in STM is given by Bardeen's solution[6, 7, 8]:

$$I = \frac{4\pi e}{\hbar} \int_{-\infty}^{\infty} \rho_s(E_f + \epsilon)\rho_t(E_f - eV + \epsilon)[f(E_f - eV + \epsilon) - f(E_f + \epsilon)]|M_t|\, d\epsilon \tag{1.3}$$

where ρ_s and ρ_t are the density states of the sample and the tip, respectively, M_t is the tunneling matrix element depending on the tip and the sample properties, and f is the Fermi-Dirac distribution. In order to simplify the tunneling current we can make a few assumptions to Equation 1.3. We can approximate the Fermi-Dirac distribution at low temperatures with a step function. This is a reasonable approximation given that most of our experiments are being conducted at 4K

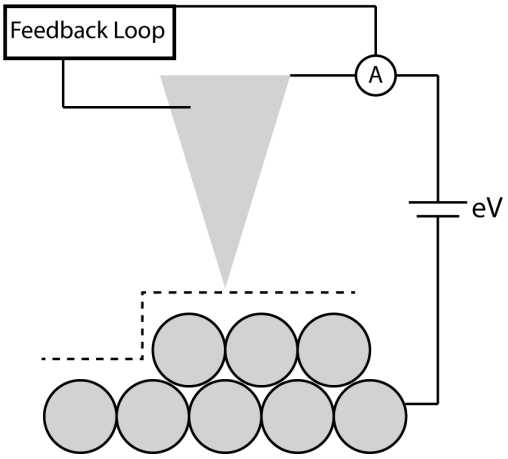

Figure 1.2: Schematic of the constant current mode of STM to acquire topography using a feedback loop and adjusting the tip height from the surface

STM. However, for room temperature measurements, the Fermi-Dirac broadening effect must be considered. Furthermore, the tunneling matrix element can be obtained from the WKB approximation[8]. Lastly, the tip density of states can be approximated as constant and energy-independent. This assumption requires calibrating and preparing the tip on a known surface such as Au(111) as a reference point prior to the measurements. Taking into account these major assumptions, the tunneling current takes the following form:

$$I = \frac{4\pi e}{\hbar}\rho_t e^{\frac{-2d}{\hbar}\sqrt{2m\phi}} \int_{E_f}^{E_f+eV} \rho_s(\epsilon)\, d\epsilon \tag{1.4}$$

where ϕ is the average work function of the tip and the sample and m is the electron mass. Equation 1.4 shows that the tunneling current decays exponentially as a function of the distance between the tip and the sample. Further, it demonstrates the tunneling current is proportional to the summation of the sample energy states between the offset of bias. This formula is the foundation of different functionalities of STM including topography and spectroscopy. In the following, we will delve into these aspects in more depth by utilizing Equation 1.4.

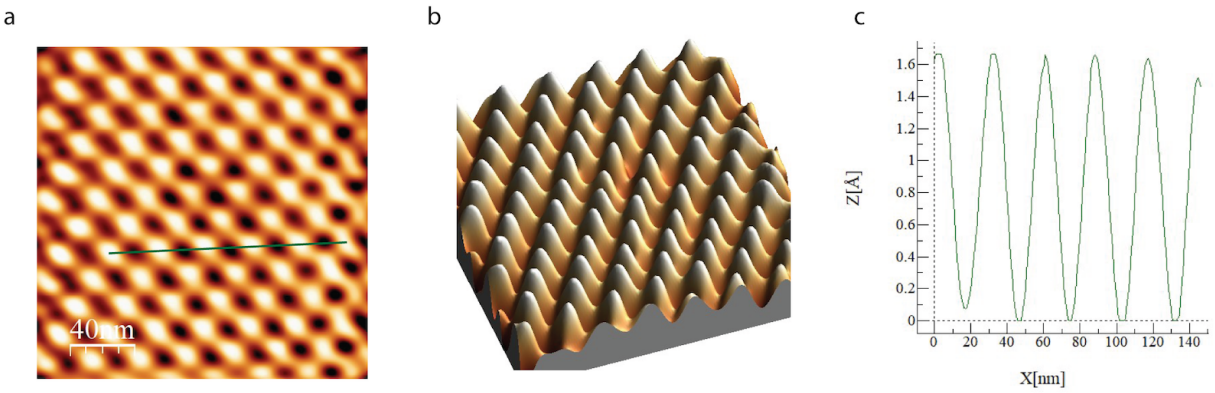

Figure 1.3: **a** The STM topographic image of twisted graphene moire**b** The 3D profile of the surface showing the roughness**c** The 2D height profile along the line shown in a

1.2 Topography

Topography is one of the most powerful STM modes. Utilizing Equation 1.4 which demonstrates the current decreases exponentially as a function of distance, we can determine the surface structure. A feedback loop can be employed to keep a constant tunneling current. The tip adjusts the distance between itself and the sample by retracting or extending the piezoelectric to maintain a constant current. Thus, the height profile of the tip over a scanned area reveals the surface roughness. Figure 1.2 illustrates how topography is generated in a constant current mode via a feedback loop. The dashed line is the height profile of the tip relative to the sample detecting the edge step by retracting to retain the constant current. Figure 1.3a shows a topography image from a moire lattice, described in detail in chapter 2, on a twisted graphene device. The 3D plot of the same topographic image is shown in Figure 1.3b illustrating the structure roughness. The height profile across the line imposed over the topographic image is provided in Figure 1.3c displaying the moire pattern periodic structure.

1.3 Scanning Tunneling Spectroscopy

Scanning Tunneling Spectroscopy (STS) is another powerful mode of STM revealing the electronic properties of the material. Equation 1.4 provides insights into spectroscopic measurements.

Taking the derivative of Equation 1.4, the differential conductance is proportional to the local density of states (LDOS) of the sample as shown below:

$$\frac{dI}{dV} \propto \rho_s(\epsilon) \tag{1.5}$$

This equation is the core of STS measurements and investigations into the band characteristics of materials. It demonstrates that we can extract the sample LDOS by modulating the voltage, collecting the associated current oscillation, and determining the dI/dV. In the following, we will examine in detail three distinct STS measurements that were used in this paper.

1.3.1 Single Point Spectra

There are two methods to obtain the dI/dV spectra. By switching off the feedback loop, we can freeze the tip at a certain distance from the sample. The voltage is then swept between $V_{initial}$ and V_{end}. Meanwhile, the corresponding current is recorded to acquire the I(V) curve. During the acquisition of a spectroscopy curve, the feedback loop is switched off. Motivated by Equation 1.5, one can take the numerical derivative of the I-V curve and derive dI/dV spectrum. However, this method is followed by high-frequency noise. Instead, we can use a lock-in amplifier to modulate the voltage at a specific frequency (chosen in a way to avoid resonating with the electronic frequencies) and collect the oscillation in the tunneling current[9, 10]. This method is a robust way to measure dI/dV with a high signal-to-noise ratio. The result of this measurement is a 1-dimensional dI/dV curve. In order to acquire a more reliable dI/dV curve we can repeat the measurement and take an average over the data set. On a homogeneous sample, single point dI/dV spectrum is spatially independent and is useful for shedding light into the material electronic properties. However, if LDOS varies across the surface of the material, imaging spectroscopy is a more effective way. To get information about the change of LDOS across a line or region, instead of collecting several single-point spectra manually, we can utilize a linecut or map spectroscopy as described below.

1.3.2 Spectroscopic Linecut

Spectroscopic linecut involves dI/dV measurements across a line on the sample surface. To perform a linecut measurement, a certain number of points are included in a line and a single-point spectrum is taken at each point. Through this process, The height of the tip is stabilized at each point, but the feedback loop is turned off during the acquisition of dI/dV data. Once the data is obtained, the feedback loop is turned on again to adjust the height and the process is repeated for the next point. The linecut measurements are useful to gain insights across a junction with different dopings or distinct moire sites possessing different electronic properties. For example, we used this method to observe the evolution of dI/dV across the p-n junction in graphene/α-$RuCl_3$ nanobubbles (chapter 6).

1.3.3 Spectroscopic Map

The spectroscopic map is a powerful method to visualize the electronic features and the change of the density of states over an area to study phenomena such as moire potential (chapter 3), p-n junctions (chapter 6), and quasiparticle interference. In order to obtain a spectroscopic map, the tip takes dI/dV spectrum pixel by pixel from a selected area of the sample. At each pixel, the tip implements a single-point spectrum by adjusting the height, turning off the feedback loop, and collecting dI/dV before moving on to the next pixel with feedback switched on. This leads to a 3-dimensional data set including two spatial dimensions (x,y) and energy. We can plot the LDOS map at specific energy and investigate the spatial dependence of the electronic states. A spectroscopic map allows us to visualize how the electronic properties of a material vary over the surface, revealing important information about the underlying physics.

1.4 Experimental Setup

During the initial stages of my PhD, I designed a cryogenic STM setup from scratch. This great experience proved to be invaluable as it allowed me to develop an in-depth understanding of

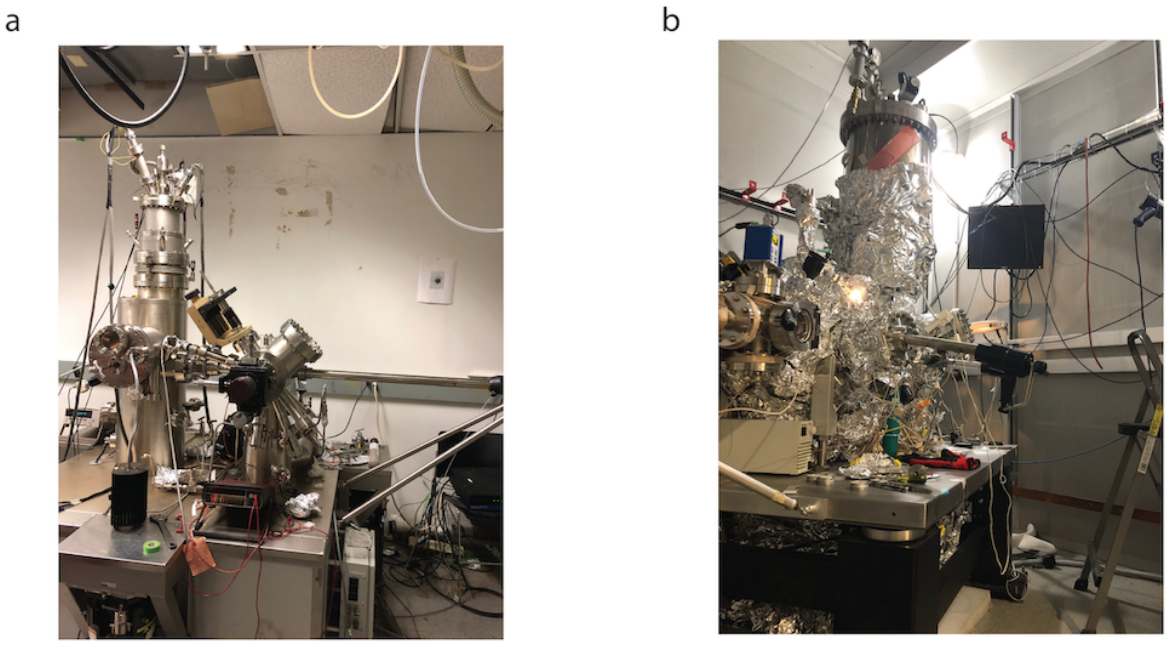

Figure 1.4: **a** The omicron STM operating at room temperature **b** ULL STM operating at 4K

the machine and familiarize myself with the technical details involved in building such a complex apparatus. This knowledge was useful in troubleshooting the issues I faced with the STM systems in the laboratory later on. During my PhD and depending on the projects, I worked with five different STM machines at Columbia, three were home-built, while the other two were Omicron systems. Figure 1.4 a and b shows the Omicron and the home-built 4K systems, respectively. This unique opportunity allowed me to gain extensive experience working with a variety of systems, each with its own unique strengths and weaknesses. I developed a deep understanding of the critical components that are required for the successful operation of an STM setup. These include the scanning mechanism, noise isolation, electronic measurement system, and tip preparation. Each of these components must be carefully optimized and calibrated to ensure that the system is operating at its full potential. In the following, I will share my thoughts on the critical components of an STM setup.

1.4.1 Piezoelectrics

The functionalities of STM strongly depend on the precision of the tip motion. There are two types of motions in the system 1) course motion over a large distance and 2) fine motion on the atomic scale. The building blocks of both are piezoelectric materials. Piezoelectric materials are widely used in scanning tunneling microscopy (STM) due to their ability to convert electrical energy into mechanical motion[11]. The electric field generated by an applied voltage difference between two piezoelectric plates gives rise to the deformation of the polar molecules of the material and thus small motion. Depending on the direction of the electric field, the piezoelectric can expand or contract giving access to moving in both directions. Using this mechanism, the course mover includes stacks of piezo for different directions (x,y,z) connected by the wires from the microscope to an external voltage source. To control the fine motion, the tip is mounted in a piezoelectric scanning tube consisting of four quadrants. If all four voltages are identical the tip moves in the z direction however any asymmetry in the applied voltage leads to the bent tube and the fine motion in x and y with high precision in the order of atomic scale. For tip positioning, the piezoelectric element is typically used in the feedback loop of the STM, which is responsible for controlling the position of the tip above the sample. As the STM tip approaches the sample, the piezoelectric element is used to adjust the position of the tip, bringing it closer or further away from the sample surface to maintain a constant tunneling current. This precise control of the tip position allows for high-resolution imaging and spectroscopic measurements of the sample surface. During my time in the lab, I was responsible for repairing and rewiring the piezo stacks and the tube scanner of one of the home-built STMs after the piezo failed to function properly. It was absolutely fascinating to see how delicately the piezo stacks are wired leading to nanometer-scale movement of the microscope and high-resolution imaging and spectroscopic measurements.

1.4.2 STM Tip

The tip of a scanning tunneling microscope is one of the most critical components of the instrument, as it plays a crucial role in the imaging and spectroscopic measurements of a sample surface.

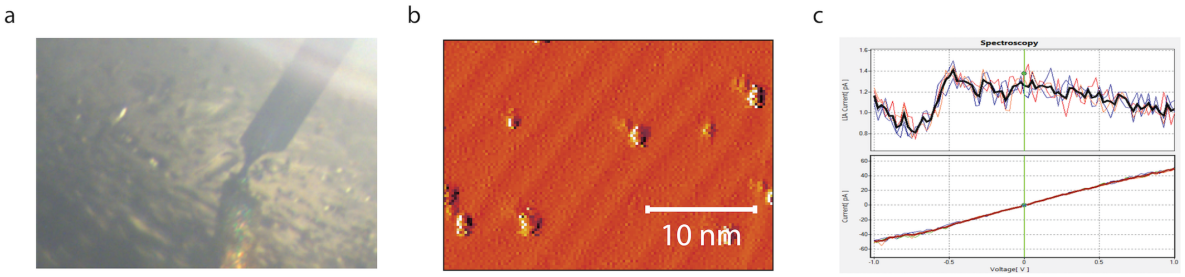

Figure 1.5: **a** Camera image of the tip and its shadow landing on Au(111) surface **b** Topographic image of gold surface showing herringbone patterns as well as poked areas by tip **c** The dI/dV and I/V curves on gold in order to calibrate the tip

Therefore, it is essential to prepare and calibrate the tip carefully to achieve the best performance and obtain reliable data. The preparation of the STM tip typically involves several steps. Firstly, a wire made of a conducting material such as tungsten, platinum, or gold is carefully cut. We use electrochemically etched tungsten tips prepared in NaOH solution. However, tungsten gets oxidized quickly in the air thus in situ preparation on a reference surface such as Au(111) or HOPG is required. If the tip gets broken by a hard crash on a sample, a new tip needs to be mounted. The tip transfer process into the microscope depends on each STM system. For instance, a magnetic sample holder is used to load a tip in Omicron STM. Whereas VT STM requires venting and taking out the entire microscope to load a new tip. In order to prepare the tip in situ after "soft" crashes, we begin with field emission on a clean and flat Au(111). This process involves applying 200 V to the tip and creating a giant electric field to remove any contamination at the end of the tip. Before moving to the next step, we can check the tip quick response to the change of field emission current. We then approach the gold surface with the tunneling mode and scan the surface. Figure 1.5a shows the tip and its shadow on a gold surface in 4K STM. The Au(111) surface is a well-studied material in surface science and exhibits a range of reconstructions[12, 13]. As a result of surface reconstruction, the herringbone pattern is observed on Au(111) in which the gold atoms rearrange themselves into arrays that form a V-shaped pattern. Figure 1.5b shows the herringbone patterns as parallel lines. We then perform I-Z measurements to crash or "poke" the gold by less than a nanometer and create a sharp tip end. The trace of the tip poking on the surface is visible

by circular dots showing the shape of the apex of the tip (shown in Figure 1.5b). Another method to confirm the sharp tip is conducting I-Z measurements. Based on Equation 1.4, the exponential form of I-Z curve also reflects on a sharp tip and indicates if the tip is prepared. Lastly, we conduct dI/dV on Au(111) to verify the tip calibration by detecting the surface states[14]. Figure 1.5c shows a typical dI/dV on the gold surface. Obtaining this spectrum on the Au surface shows the tip is well-calibrated and prepared for the other measurements. In summary, the preparation and calibration of the STM tip are critical to achieve reliable and high-quality imaging and spectroscopic measurements. The tip must be carefully prepared to produce a sharp tip apex and calibrated to maintain a constant tip-sample distance, which is essential for obtaining accurate data.

1.4.3 Noise Reduction

STM is a high-resolution technique that can provide atomic-scale images of surfaces. However, it is susceptible to noise, which can limit the resolution and quality of the images obtained. Noise reduction from mechanical vibration and electronic noise is crucial for STM tunneling process. To prevent mechanical noise, the STMs are located in the basement and inside acoustic rooms. The system is mounted on an optical table and the microscope is hanging from springs as shown in Figure 1.6. Another critical component of STM is the ultra-high vacuum (UHV) environment with 10^{-10} torr pressure inside a stainless steel chamber achieved by an ion pump. This is essential to stabilize the tip-sample junction at a few angstroms above the surface without crashing while measuring. It also prevents sample contamination over time as it is placed on the stage for measurements. To further stabilize the tip junction and improve the signal-to-noise ratio, we can couple the STM to cryogenics and cool down the system to 4K using liquid helium. STM can benefit from operating at low temperatures, where thermal noise and thus the drift are reduced. Cooling the sample and the tip can also reduce the thermal vibrations of the atoms, which can increase the stability of the feedback loop and improve the resolution of the images. In addition to that measuring at low temperatures allows us to gain higher energy resolution in spectroscopic measurements vital for detecting fragile electronic features such as flat bands with small energy

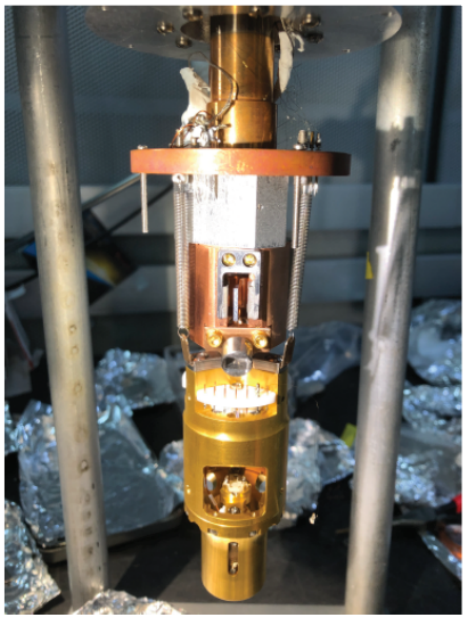

Figure 1.6: **a** The STM microscope hanging from springs for noise reduction.

bandwidths. The energy resolution is limited by kT where k is the Boltzmann constant and by lowering the temperature the energy resolution enhances. At room temperature, this is restricted to ~25 meV however it drops to ~0.3 meV at 4K. Another important factor in noise reduction is electronics. This noise can come from a variety of sources, such as power cables and electronic devices. Shielding the microscope and cables are required to reduce the noise. Coaxial wires with minimum lengths are also used to reduce noise relative to the current signal. Nonetheless, a high-quality current amplifier is necessary to collect and amplify pico-amps tunneling current. Another important element of STM that can be affected by noise is the feedback loop. STM uses a feedback loop to maintain a constant current between the tip and the sample, and this feedback loop can be adjusted to reduce noise. The feedback gain can be optimized to balance the response time and the stability of the system. A low gain can reduce the noise but may also increase the response time and lead to crash, while a high gain can reduce the response time but may introduce instability. By applying these techniques, it is possible to mitigate the noise in STM and obtain high-quality images. However, it is important to balance the different parameters to achieve the best performance for each specific measurement.

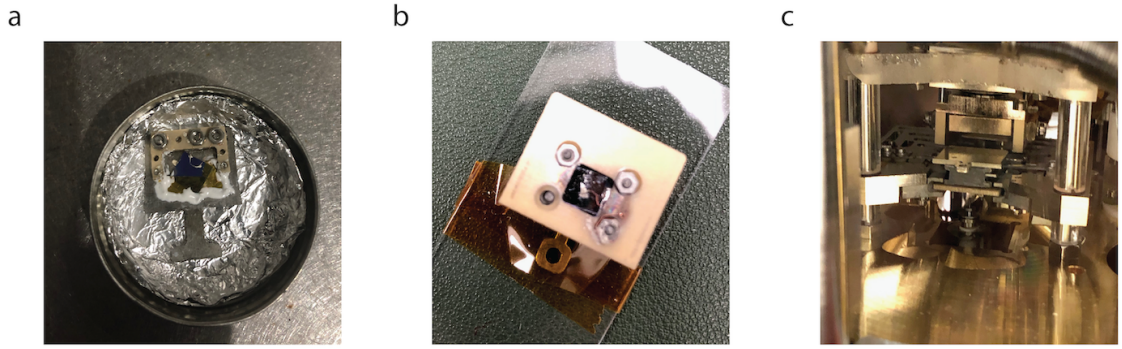

Figure 1.7: Multi contact sample holders of **a** ULL system and **b** single contact Omicron VT sample holder. The thin copper wires from the sample go under the nuts and make electric contacts with the STM. The nuts are separated by an insulating ceramic piece to avoid the short. **c** The omicron sample holder is placed into the stage and creates contact with the stage from the side brushes.

1.4.4 Multi-Contact Sample Holder

The sample holder is another important component of STM measurements. It typically consists of a metallic plate that the sample is mounted on it and a few small screws on top of the plate to make electric contacts. There are different types of sample holders, depending on the experimental setup and the type of sample. Usually, for a bulk sample, a metallic plate is used however in order to gate 2D devices a multi-contact sample holder is required. Figure 1.7a and b show ULL and Omicron sample holders. The screws and nuts are separated by an insulating piece to avoid electrical short and a wire from the sample is wrapped around the screw to make contact to the STM. Figure 1.7c shows a sample holder in Omicron stage where the side brushes make electric contacts to the microscope and the tip approaches from underneath.

Chapter 2: Scanning Tunneling Microscopy on Two-Dimensional Materials

Atomically thin 2D materials are a distinct group of materials that possess unique and fascinating properties. The exploration of 2D materials has attracted tremendous attention due to their vast potentials in both practical applications and fundamental physics studies. Since the discovery of graphene in 2004, other layered materials including 2D semiconductors[15, 16], superconductors[17, 2, 18], and magnets[19, 20] have emerged and are showing promising platforms for exploring many quantum phenomena such as exciton condensate[21, 22], superconductivity[2], quantum spin liquid[23] and other strongly correlated phases of matter. For instance, In the past decade, semiconducting transition metal chalcogenides (TMDs) have attracted significant interest due to their intrinsic properties such as large band gap and large spin-orbit coupling as opposed to graphene. In addition to that TMDs have shown high tunability in carrier density and the capability to integrate into electronic devices. Another promising route to study strongly correlated phases which were previously challenging is using moiré structures. Since the discovery of superconductivity in twisted magic angle bilayer graphene, the moiré pattern has been the focus of numerous theoretical and experimental works. It has been shown that adjusting the twist angle, hence the moiré wavelength leads to the tuning of interlayer hoping which is related to flat bands, moiré potentials, and other emergent phenomena. Therefore, the twist angle is a powerful knob allowing us to access exciting physics. Our approach to studying 2D materials and their unique electronic properties is scanning tunneling microscopy (STM) and spectroscopy (STS). STM is a powerful local probe providing information about the surface structure and the band properties of the materials. Utilizing STM for bulk materials is well established by cleaving the crystal in situ. Nonetheless, the measurements of 2D devices are followed by technical obstacles including sample fabrication and preparation for STM measurements, making proper electrical contacts for low-temperature studies, and landing on nano-scale areas. In this chapter, we delve into the struc-

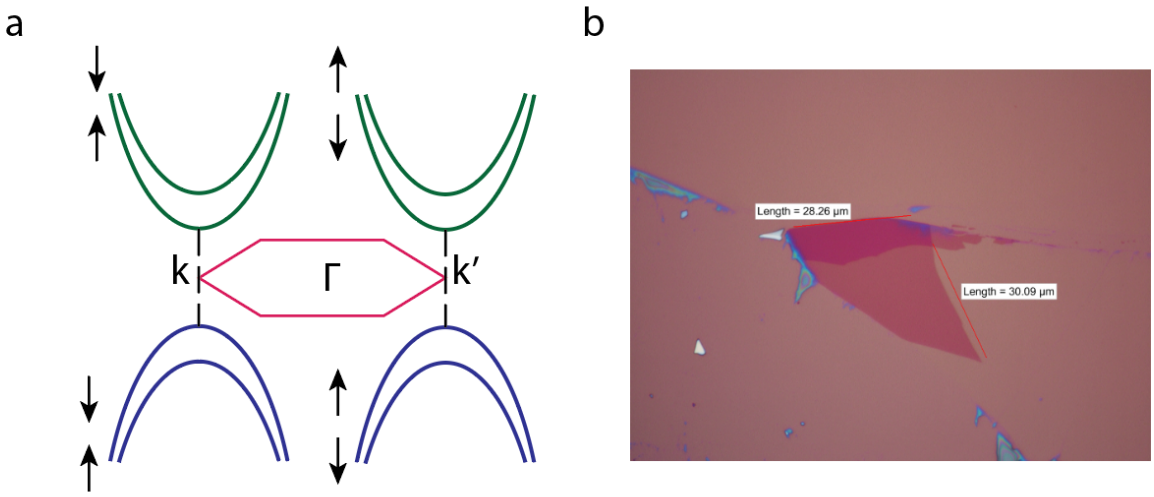

Figure 2.1: **a** The band structure of monolayer WSe_2. The valence band and conduction bands are located at K and K' points, the corners of the hexagonal Brillion zone. **b** The image of exfoliated WSe_2 monolayer and bilayer taken by the optical microscope. The thickness of the exfoliated layers can be determined by the color contrast.

ture of 2D materials and their band characteristics, as well as the obstacles I encountered during STM measurements on 2D samples and the strategies I employed to overcome them.

2.1 Two-Dimensional Materials

2.1.1 TMD Monolayers

Transition metal dichalcogenides (TMDs) are a large family of 2D materials with semiconducting bandgaps and great tunability to investigate correlated regimes in condensed matter. The TMD layers are stacked by van der Waals (vdW) interactions. The weak van der Waals (vdW) interactions between layers permit us to exfoliate bulk crystals and reach to monolayer limit. A category of TMDs has the chemical formula as MX_2 (M (metal) = W, Mo and X (chalcogen) = S, Se, Te)[24]. In this thesis, my focus has been $MoSe_2$/ MoS_2/ WSe_2 and WS_2. We will examine the band properties of different TMD heterostructures in the next chapters. In monolayer limit, TMDs exhibit a direct band gap, with the valence and conduction band edges located at the K point, which is the corner of the first Brillouin zone. In contrast, bulk TMDs possess an indirect

band gap from K to gamma in the reciprocal lattice. This difference in band structure gives rise to distinct optical and electronic properties in the TMD monolayers. The first experimental realization of band properties is by photoluminescence (PL) showing strong luminescence in monolayer TMD compared to bulk crystals[15, 25]. As a result, by increasing the number of layers, the band gap becomes significantly smaller. Another parameter that can be extracted is exciton binding energy which is defined by the difference between optical and electronic band gaps using PL[26, 27] and STM[28, 29]. It has been shown that TMDs possess large exciton binding energy[28] due to strong Coulomb interaction making it a unique material for excitonic devices[28]. Figure 2.1a illustrates a schematic of WSe_2 band structure at the K point with simple parabolic band gap[15]. Figure 2.1b shows the optical image of exfoliated WSe_2 monolayer attached to a bilayer from top using scotch tape exfoliation method.

2.1.2 Twisted Bilayers: Moiré Pattern

Twisted moiré patterns have recently emerged as an important part of the study of two-dimensional materials, particularly transition metal dichalcogenides (TMDs). When two monolayers are stacked on top of each other with a slight twist angle, a periodic moiré pattern is created, which results in a superlattice structure with a unique set of electronic properties. These properties arise from the interaction between the layers, which modify the electronic band structure of the material. Thus, the twist angle between 2D materials is a powerful tuning knob to control the interlayer hybridization leading to emergent phenomena such as superconductivity[2, 4, 30], Mott Insulator[31, 3, 32, 33, 34], and quantum anomalous Hall[35, 36]. As a result of twist angle or lattice mismatch between layers, a moiré pattern, a periodic superlattice, is formed. The moiré wavelength is calculated as the following[37]

$$\lambda = \frac{a_t + a_b}{2\sqrt{2(1+\delta)(1-cos(\phi)) + \delta^2}} \tag{2.1}$$

where ϕ is the rotational twist angle and δ is the lattice mismatch. a_t and a_b are the lattice constants of the top and bottom layers, respectively. This equation shows the moiré wavelength of bilayers can be adjusted by the rotational twist angle. As a result of the formation of the superlattice,

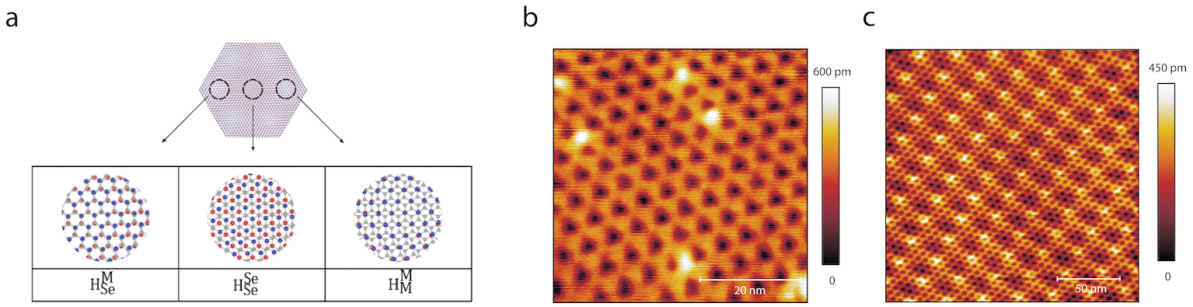

Figure 2.2: **a** A schematic of moiré pattern of $WSe_2/MoSe_2$ bilayer showing three different moiré configurations. **b** STM topographic image on the same heterobilayer showing triangular moiré structure **c** moiré pattern of graphene/graphene and also graphene/h-BN.

a 2D energy potential with the same periodicity is generated, so-called moiré potential, giving rise to the modification of the band structure. The strength of the moiré potential depends on interlayer hybridization and the flatness of the band. For instance in graphene when the layers are aligned at a very specific twist angle of around 1.1 degrees the moiré potential creates a nearly flat energy band which is characterized by strong electron-electron interactions and lead to the formation of correlated electronic states[3, 38]. Therefore, The precision of the twist angle is crucial for studying twisted materials. There are two well-established methods to fabricate twisted bilayers. The tear stack technique is used for twisted homo-bilayers such as twisted graphene and twisted WSe_2. However, in the case that two layers are distinct second harmonic generation (SHG) measurements are required to find the lattice orientation of each layer relative to the other. We discuss the details of the fabrication in the next sections. Figure 2.2a shows a schematic of moiré pattern with three distinctive moiré configurations. A topographic image of moiré pattern in $WSe_2/MoSe_2$ obtained by STM is shown in Figure 2.2b. Two moiré patterns corresponding to twisted bilayer graphene and graphene/h-BN are clearly observed in STM topography in Figure 2.2c. In summary, moiré patterns allow us to access new physics that was difficult to access with conventional materials due to a lack of high-quality and highly tunable devices. It provides a unique platform for exploring and engineering novel electronic phenomena, which could have significant implications for the development of advanced electronic devices.

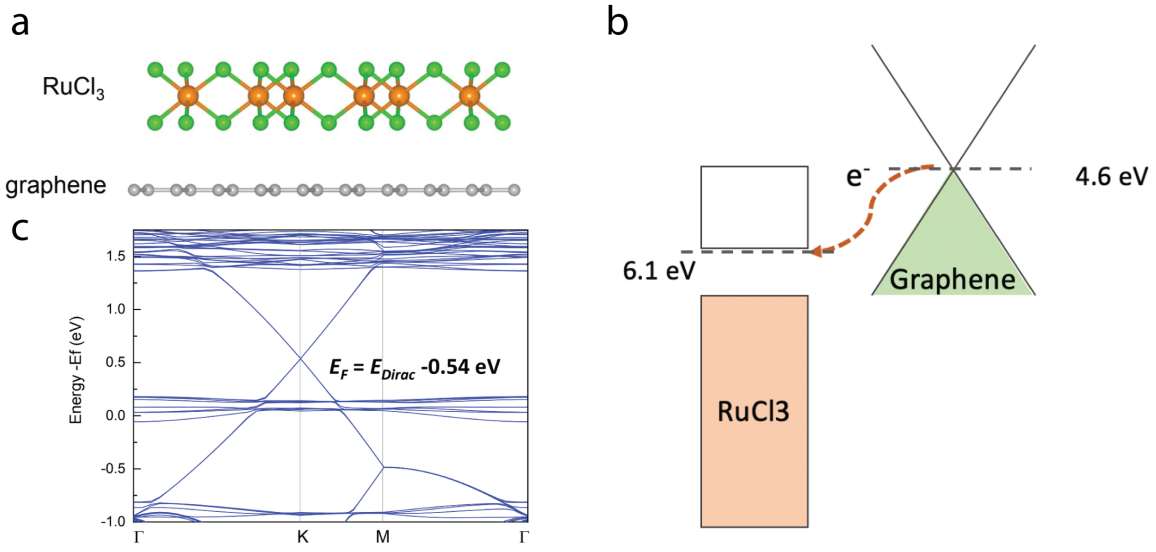

Figure 2.3: **a** Side view of graphene/α-$RuCl_3$ heterobilayer. **b** Schematic of charge transfer between graphene and α-$RuCl_3$ due to the difference in work function. **c** DFT calculation of the heterostructure band structure and showing 0.54 eV shift in Dirac energy position due to charge exchange process.

2.1.3 α-$RuCl_3$ Heterostructures

Beyond moiré heterobilayers, we can vertically stack materials based on the concept of interlayer charge transfer between layers due to work function differences. For instance, the large work function difference between graphene (4.6 eV) and α-$RuCl_3$ (6.1 eV) heterostructure leads to massive interlayer charge transfer. This large carrier exchange results in heavily p-doped ($10^{13} cm^{-2}$) and n-doped graphene and α-$RuCl_3$, respectively. This observation opens routes toward high carrier density physics in both graphene and α-$RuCl_3$ which was previously challenging due to poor dielectrics. Figure 2.3a shows the side view of the heterostructure. The charge transfer mechanism between two layers is illustrated in Figure 2.3b. Our density functional theory (DFT) calculations (Figure 2.3c) demonstrate a 0.54 shift in the Dirac point confirming a massive charge exchange between layers. Another example studied in this thesis is WSe_2/α-$RuCl_3$ heterostructure. As a result of the enormous charge transfer between WSe_2 and α-$RuCl_3$, WSe_2 becomes heavily p doped, and the Fermi level shifts to the valence band edge. The results of this work are important for future

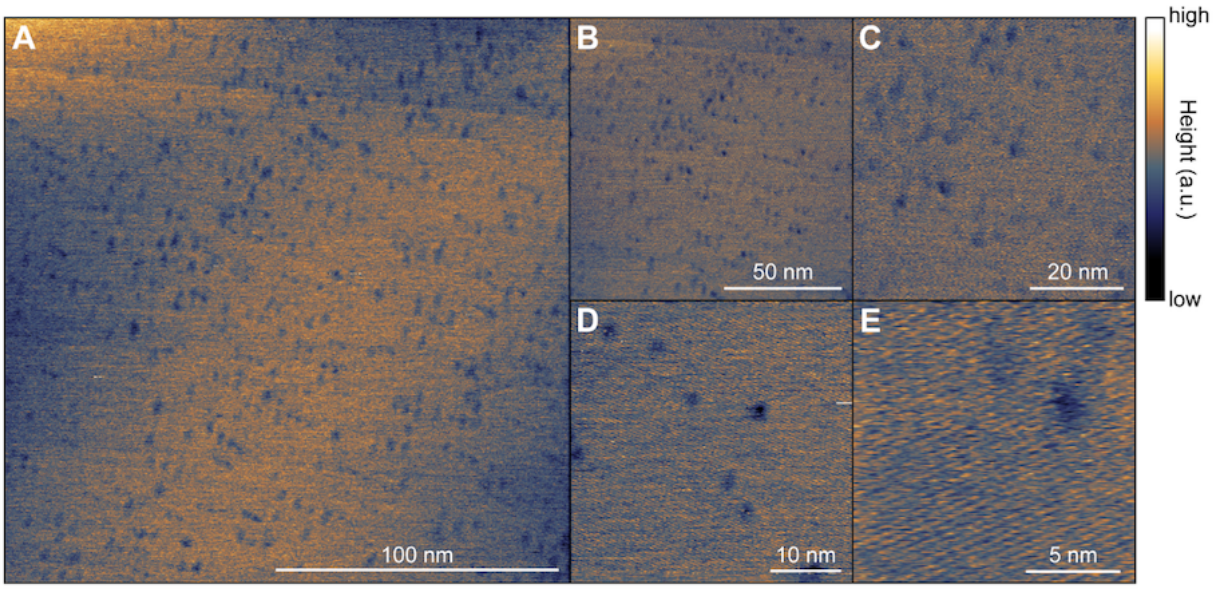

Figure 2.4: STM topographical maps of bulk CrSBr. **a** Scanning tunneling microscopy topography maps of bulk CrSBr along the c-axis with increasing resolution. The scale bar for all color maps is given on the right. The defect density found from manually counting individual defects is $8 \times 10^{11} cm^{-2}$, $6 \times 10^{11} cm^{-2}$, and $4 \times 10^{11} cm^{-2}$ for (C), (D), and (E), respectively. All images were taken at 300 K. The STM bias and current set points were 1 V and 50 pA, respectively.

device engineering to take advantage of α-$RuCl_3$ properties to improve contacts to WSe_2 at low temperatures. So far achieving good contacts to WSe_2 has been challenging and this method paves the way to investigate and access the correlated states in twisted TMDs.

2.1.4 Other Heterostructures

Another 2D device that was investigated by this work is graphene/ CrsBr. CrsBr is an antiferromagnetic 2D semiconductor with a high transition temperature[39, 40]. The proximity with CrSBr can lead to intriguing physics in graphene due to the semiconducting and magnetic characteristics of CrSBr[41]. Characterization of these heterobilayers shapes our understanding of induced properties in heterointerface physics. Here our approach to studying the 2D systems is STM and figure 2.4 shows the STM topographies on a CrSBr bulk to characterize the defect density to evaluate the crystal quality for future 2D device measurement. However conducting STM measurements on 2D devices is extremely challenging. In the next section, the details and the methods to overcome the

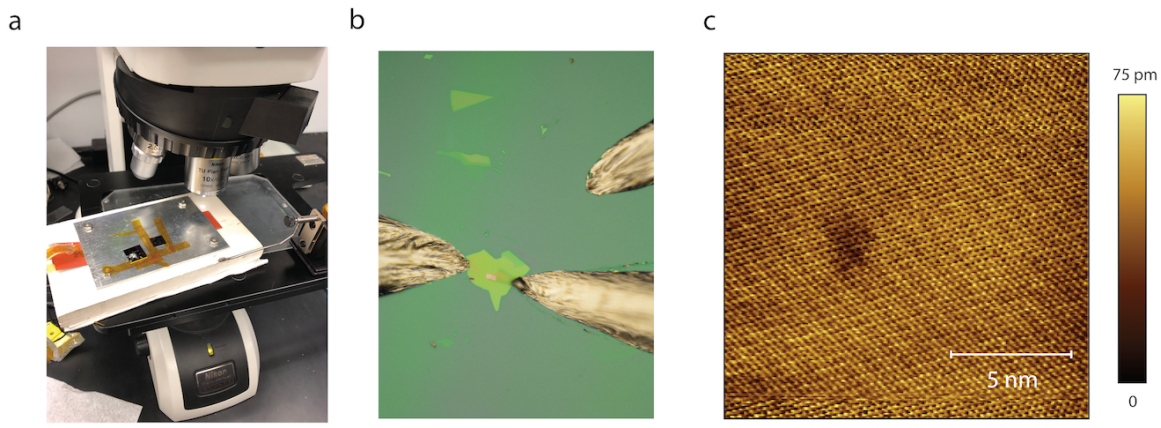

Figure 2.5: **a** The indium setup includes the optical microscope, the hot plate, and the micro solder. The 2D sample chip and indium chip are taped on the sample. **b** The indium contacts were placed on CrSBr/graphene sample. The top indium is used for pointing toward the sample and guiding for landing. **c** The STM topographic image from the CrSBr/graphene sample at 4K showing successful electric contact.

challenges are discussed.

2.2 STM Measurements on 2D Devices

STM is a powerful local probe to investigate 2-dimensional materials and reveal their unique electronic properties. The knowledge provided by STM can influence our perspective on the band structure of materials and can be utilized in future device designs. However, conducting STM/STS on 2D materials can be technically challenging including the device fabrication. The target sample is required to face up in order to make a tunneling current directly from the tip to the surface. This geometry increases the difficulty of making the contacts. Moreover, the old STM machines are usually built in compatibility with millimeter-size bulk crystals as opposed to 2D materials on a micrometer scale. Therefore, landing on a 2D device on the first attempt with a fresh tip is an extremely difficult task. I will cover the details of the challenges in the next sections.

2.2.1 2D Device Fabrication for STM Measurements

High-quality crystals with low defect density are required to host many fragile quantum effects. We use the self-flux growth method[42] to grow single crystals at Columbia. This method depends on many parameters including the growth time and temperature. In order to confirm the quality of the crystals, we scan the bulk crystals by STM and acquire topography images where the number of defects can be determined. The defect density can be obtained by averaging the densities over multiple scanned areas. The defect density reflects the quality of the crystal and enables us to tune the growth parameters more efficiently. High-quality TMD crystals have been measured by room temperature STM to ensure low defect density and they were used for the exfoliation of monolayers. Figure 2.4a-c shows STM topographic images of CrSBr crystal to characterize the defect density[39]. The defect density in this material can play an important role in the magnetic properties of the material[39]. Another obstacle for STM measurements on 2D materials is accessing a clean and atomically flat surface. During my studies, I devoted a considerable amount of time to device fabrication and the development of a robust method for STM 2D devices. Despite all the experimental efforts[43, 44, 45, 46, 47], ohmic contact to TMDs is still lacking. In the next subsection, we will discuss the methods to contact TMDs in detail. Another challenge in the fabrication of STM devices is accessing the uncovered target layer. In contrast to devices used in quantum transport or optical approaches, those used in STM require a unique geometry. Transport devices are usually encapsulated and protected between h-BN layers whereas STM devices can not be covered by h-BN due to tunneling current. Open-face device fabrication includes additional steps compared to conventional encapsulated devices for transport measurement. To fabricate a 2D device, we vertically stack the layers using the dry stamp method. A transparent poly-dimethylsiloxane (PDMS) stamp coated by a thin layer of polypropylene carbonate (PPC) is usually used to pick up a thin layer of exfoliated h-BN. h-BN is a great dielectric and also provides a flat substrate for 2D materials. We use h-BN to pick up the sample of interest such as graphene or TMDs. Next, we peel off the PPC film with the whole stack on top of it from the PDMS stamp. Then, we "flip" the stack and transfer it onto a clean silicon chip on a hot plate at 120°. We anneal the device at 200° for 20

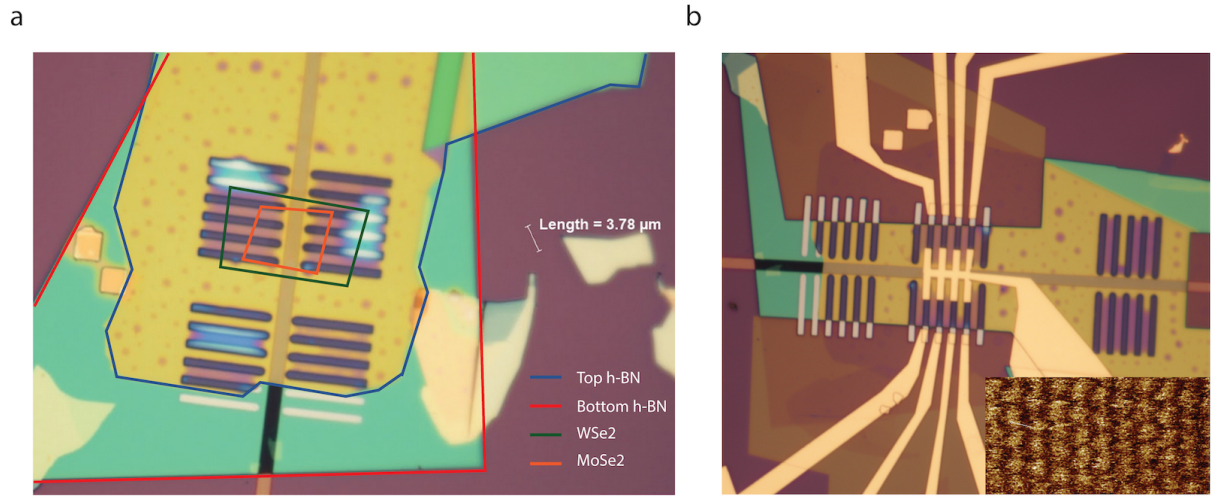

Figure 2.6: Twisted $MoSe_2/WSe_2$ heterobilayer device for quantum transport measurement. **a** The Pt contacts are deposited by pre-pattern method and the TMDs are encapsulated between the top and bottom h-BN. **b** The final device geometry after top gate deposition. the inset shows the pfm on the heterobilayer confirming 4.5 nm moiré wavelength to study by transport.

min to evaporate the PPC underneath and create a flat substrate for the STM measurements. After flipping the stack, from top to bottom, our stack includes TMD/graphene and h-BN. As a result of this method, "flip chip stacking", the TMD layer is the top layer with a clean surface protected from polymer.

2.2.2 Contacts to 2D Materials

Making electrical contact to the 2D device is necessary for applying the bias to the sample relative to the STM tip. The use of silver epoxy on the two-dimensional sample is ineffective since a small droplet spreads and covers the micrometer-sized sample. A method that is commonly used in our group is the micro-soldering of an indium alloy[48]. This is a quite precise and clean technique to contact micrometer-sized samples. One can also remove the indium contact and replace it with a new one without leaving much contamination. We use a heating stage to place the device chip on top as well as a micro-manipulator with a needle attached to it as shown in Figure 2.5a. The process is based on the melting temperature of the "Field metal" around 60°C. Using the micro-manipulator and adjusting the temperature, we can lift a sharp-ended indium

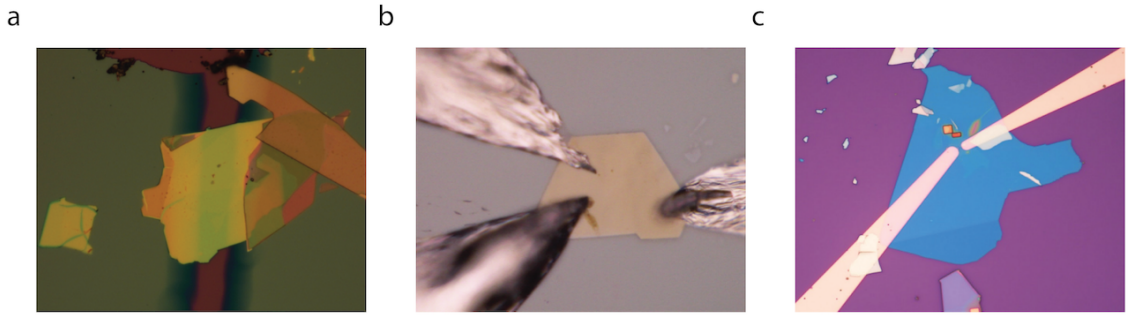

Figure 2.7: Three methods of making contacts to TMD samples for gatable devices. **a** The shadow mask technique. The gap between the two metals is where the twisted TMDs are located. **b** Indium contact to graphene/α-$RuCl_3$ sample **a** Lithography method to deposit Pt on TMDs. This method requires cleaning the surface after removing the lithography mask.

and place it on the device. The other side of indium which is much wider can be used to make contact with silver epoxy and wiring to the STM sample holder. Figure 2.5b shows three indium contacts to graphene/CrSBr heterobilayer. Two of the indiums are used for contacts to graphene and the top one is pointing to the sample to assist with tip landing. The STM topographic image from the CrSBr/graphene sample at 4K is presented in Figure 2.5c reflecting on successful electric contact. It is worth noting that indium alloys make great contacts to graphene due to the work function difference, however, it is ineffective on TMDs. I spent a significant amount of time and still, there is an extensive ongoing effort for making ohmic contacts to TMDs to investigate these materials for low-temperature studies and detect the predicted correlated states by STM and transport techniques. So far based on transport measurements Platinum (Pt) used in the prepattern method is the best way to contact TMDs due to the lower Schottky barrier which originates from the metal-TMD interface[49]. In this method, Pt is deposited on h-BN and cleaned by atomic force microscopy (AFM) in contact mode for a few hours to remove any contamination and achieve a smooth metallic surface. Then the h-BN/ TMD stack is dropped on h-BN/pt electrodes and as a result, Pt creates electrical contact to TMD layers. Figure 2.6 a and b show transport devices I made while collaborating with Dean's lab using prepattern Pt contacts for quantum hall measurements. The inset shows the moiré pattern in this device obtained by the piezoresponse force microscopy(

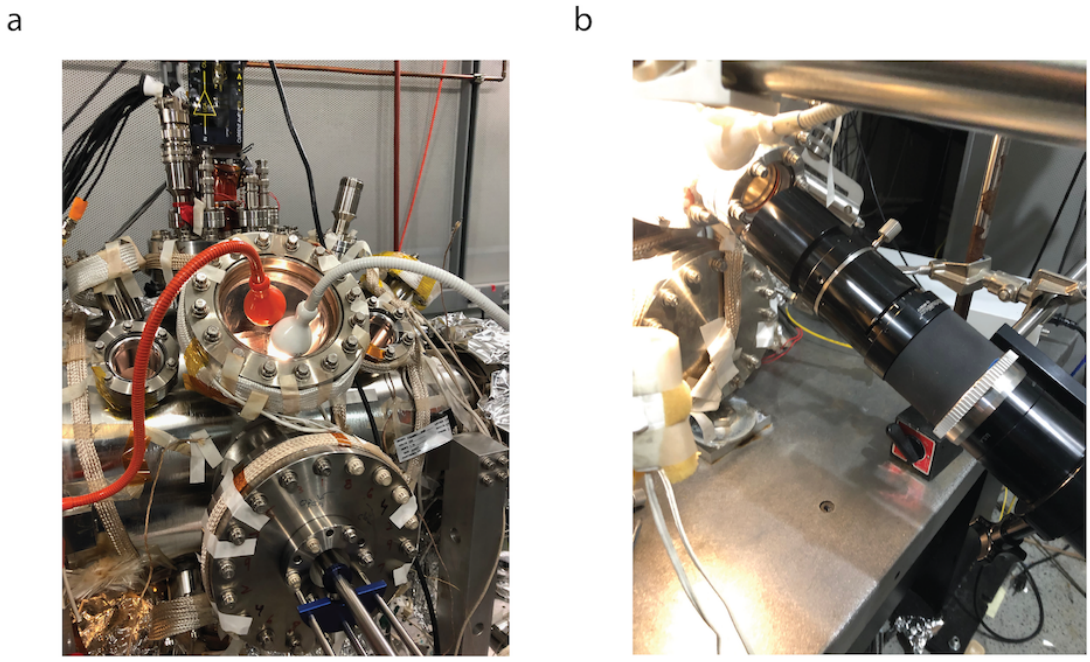

Figure 2.8: **a** The view port of room temperature STM and shining light pointing to the sample stage **b** The view port of ULL STM and camera aligned to the sample for tip landing

pfm)[50]. However, this method does not work for STM measurements due to open-face device geometry. Any direct metal deposition leads to contamination of the TMD layer from lithography masks. One effective approach is using graphite to make contact with the TMD layer. In this case, we can place an indium contact on graphite and wire the indium to the sample holder. Nevertheless, this method restricts the doping level due to graphite screening, and more importantly, the contact resistance of graphite electrodes is quite large at low temperature and no longer effective. Another method that I developed and optimized during my PhD is using the shadow mask. We use the sharp end of a razer blade and adjust it on top of the sample under the optical microscope to cover and protect the area of interest.

The Pt metal is then evaporated on the chip, resulting in metal contact on the exposed surface. This method requires parameter optimization of the deposition tool such as the height and beam energy to prevent cracks in the monolayers. The precision of a sharp contact strongly depends on

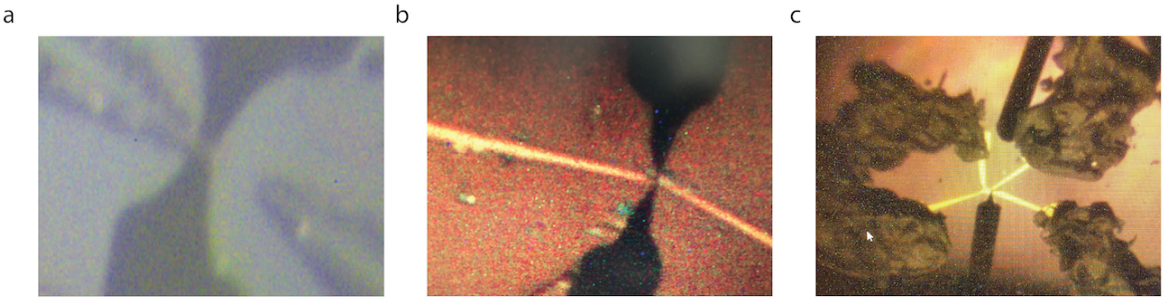

Figure 2.9: **a** The ULL STM tip view through the camera. Due to poor optical view other methods such as capacitive current measurement is used to land on a 2D device. **b-c** The tip view of room temperature STM. The middle point between the tip and its shadow is where the tip lands. The deposited metal electrodes make contact with the sample and point to the position of the sample as well.

the razor blade position which is extremely challenging to secure a millimeter-sized razer blade with tape on top of a micrometer-sized target area. Despite the difficulty, this method preserves the cleanness of the TMD layers as opposed to lithographic methods. Figure 2.7a shows a twisted WSe_2/WS_2 device for STM study using the shadow mask technique. The small distance between the electrodes is where the device is located. In this geometry silicon back gate is connected to the metal plate of the sample holder and is effective for doping. Another method, indium contact to graphene/α-$RuCl_3$ heterostructre is shown in Figure 2.7b. Direct Pt deposition on twisted WSe_2 (Figure 2.7c) is another method to make contact to TMDs however the contamination was removed by AFM to achieve a flat surface.

2.2.3 Tip Landing on 2D Samples

One of the biggest challenges in studying 2D materials by STM is approaching the tip on the target area. The STM systems were built in compatibility with large bulk crystals and usually lack good optical view ports to detect the micro-sized samples. Figure 2.8 shows the view ports of room temperature and low-temperature STMs. Crashing the tip on the non-conducting area such as silicon or h-BN requires preparing the tip on Au(111) and attempting again. My approach was using the features on the chip including the indium contacts as a guide to finding the position of

the sample. Figure 2.9 shows the STM tip and its shadow in two different STMs. Indium or gold electrodes point to the area of interest as guidance. We also use capacitive current to keep track of the height of the tip from the surface. The capacitive current increases exponentially if the tip is approaching a conductive surface otherwise it can be a sign of crashing on an insulating piece. This method is tricky as the tip may be on indium or metal contacts rather than the 2D sample. In that case, topography can provide information about the type of surface. We then move across the sample to get away from the rough indium surface and scan different parts of the device to find the flat area of interest. To confirm if the tip is on the target area, we can obtain the atomic lattice size from the topography and compare it with the 2d material lattice constant. Conducting STS is also useful for validating the material property. Nonetheless, looking for a specific moiré wavelength, for instance, magic-angle graphene, on the sample is a challenging task as the target region is on the order of several hundred nanometers. moiré inhomogeneity across the sample also makes the search procedure more complex. To make this process faster and more efficient, enhanced optical view or dual STM/AFM mode in future STM systems are crucial. In the next chapters we implement these methods to study the 2D materials in particular TMD heterobilayers and α-$RuCl_3$ heterointerfaces using STM/STS.

Chapter 3: Deep Moiré Potentials in Twisted Transition Metal Dichalcogenide Bilayers

Here, we used the methods introduced in previous chapters to report experimental measurements of the structure and spectroscopic properties of twisted bilayers of WSe_2 and $MoSe_2$ in the H-stacking configuration using scanning tunneling microscopy (STM). Twist angle is a powerful knob to create a periodic moiré pattern on the surface and thus tune the interlayer hybridization. Although there has been tremendous efforts in studying twisted graphene bilayers[17, 2, 18], characterizing the moiré effect on semiconducting TMDs has been challenging due to poor electric contact. In this work, to overcome this issue, we utilized a graphite layer beneath the heterobilayer and conducted the measurements at room temperature for lower contact resistance. Various methods for addressing the contact and tip landing issues in TMDs are discussed in chapter 2. The goal of this research was to realize moiré potential in TMD heterobilayers resulting from electronic coupling and structural rippling that can confine charged and neutral excitations[51, 52, 53, 54, 55, 56, 57]. Our experiments reveal that the moiré potential in these bilayers at small angles is unexpectedly large, reaching values of above 300 meV for the valence band and 150 meV for the conduction band, an order of magnitude larger than theoretical estimates based on interlayer coupling alone. We further demonstrate that the moiré potential is a non-monotonic function of moiré wavelength. This non-monotonicity is accompanied by a drastic change in the structure of the moiré pattern from a continuous variation of stacking order at small moiré wavelengths to a one-dimensional soliton dominated structure at large moiré wavelengths. We show that the in-plane structure of the moiré pattern is captured well by a continuous mechanical relaxation model, and find that the moiré structure and internal strain rather than the interlayer coupling is the dominant factor in determining the moiré potential. Our results demonstrate the potential of using preci-

sion moiré structures to create deeply trapped carriers or excitations for quantum electronics and optoelectronics.

3.1 Introduction

Lattice vector mismatches between two layers of a van der Waals bilayer gives rise to a moiré pattern. The moiré pattern affects the electronic structure of the bilayer, and many emergent quantum phenomena have recently been observed in these systems [58, 55, 54, 59]. In a TMD semiconductor heterobilayer, the low-energy electronic structure can be reasonably approximated by the properties of a single layer on which a spatially dependent potential energy landscape is imposed (termed the moiré potential)[60, 61, 52]. This moiré potential when periodic gives rise to subbands within the first valence or conduction bands, which are responsible for the emergent quantum properties observed. Spatially separated interlayer excitons can also be trapped within these subbands[62, 54, 51, 57, 59, 56]. Theoretical estimates based only on interlayer coupling estimate the size of this moiré potential to be of the order of a 10 millielectronvolts (meV) at small moiré wavelengths (< 5 nm)[63, 64], but experimental measurements of the moiré potential remains an important open problem in these materials.

Scanning tunneling microscopy is one of the few experimental techniques that can provide direct measurements of the magnitude of the moiré potential, due to its high energy and spatial resolution. Its use requires clean surfaces and conducting samples, both of which are significant challenges for TMD semiconductor layers. A few pioneering STM experiments have been performed on CVD grown [65, 66], rotationally aligned bilayers and (more recently) exfoliated, twisted TMD bilayers[67, 68, 69, 70]. All of these previous measurements have been performed for moiré wavelengths near 5 nm at rotational angles close to zero degrees between the two layers. In this work, we study the heterobilayer of $MoSe_2$ on WSe_2 at a range of moiré wavelengths from 5-20 nm. We avoid problems associated with sample conduction by performing our STM measurements at room temperature with a few-layer graphite substrate, under which condition the samples are sufficiently conductive.

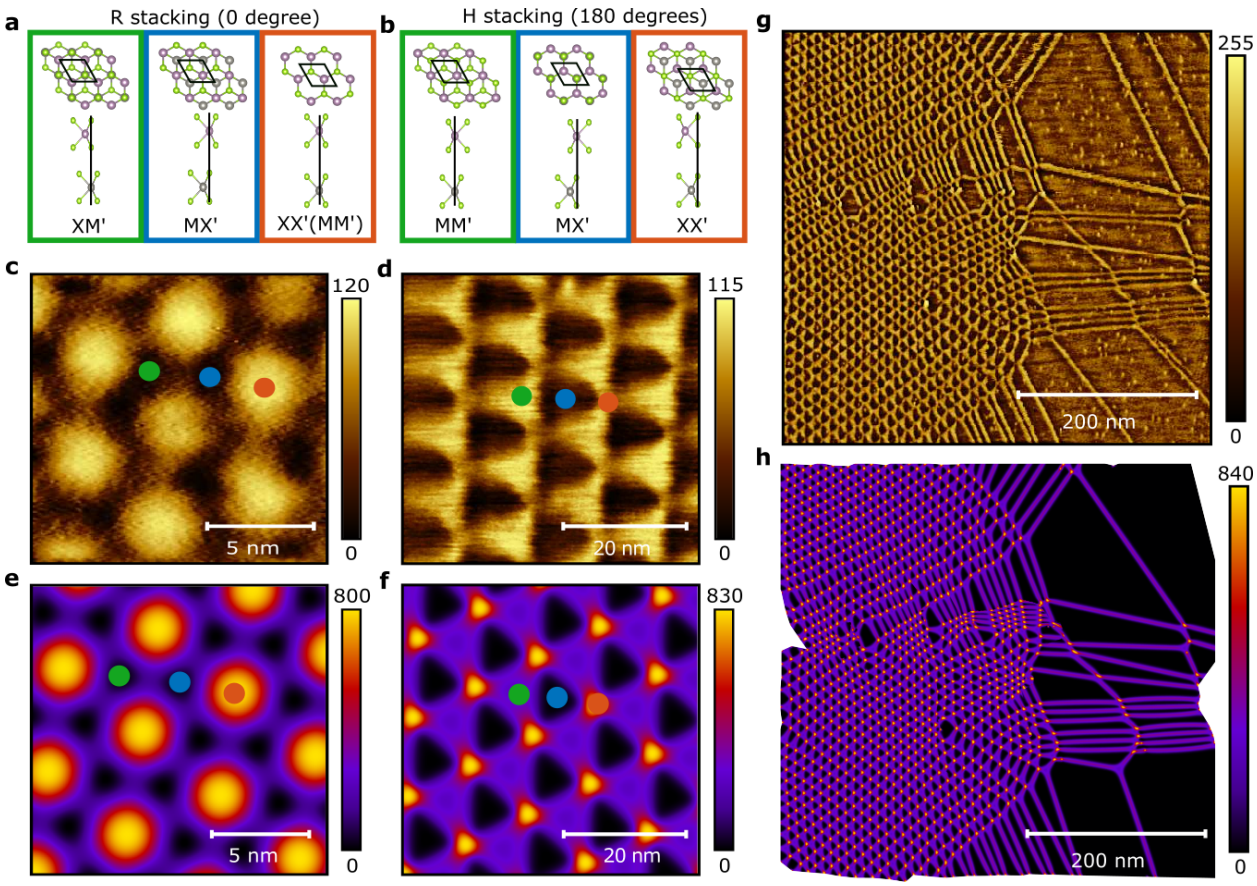

Figure 3.1: Structure of twisted heterobilayer $WSe_2/MoSe_2$. **a,b** Illustration of R- and H- stacked heterobilayers and the high-symmetry stacking configurations present within each configuration. **c,d** STM topographic images (in pm) of R- and H-stacked twisted heterobilayers. (set point of -1.4 V, 100 pA, and -1.7 V, 150 pA, respectively). **e,f** Stacking energy density (in meV/nm^2) from mechanical relaxation calculations corresponding to the STM topographs in **c,d**. The high symmetry stacking configurations illustrated in **a,b** are marked with appropriately colored dots in **c-f**. **g** Large area STM topograph (in pm) of H-stacked $WSe_2/MoSe_2$ at an average twist angle of $\sim 1.7°$. The topograph shows the presence of inhomogeneous heterostrain, one-dimensional solitons, point defects in the individual layers and edge dislocations of the moiré lattice. **h** Calculated stacking energy density (in meV/nm^2) of the relaxed structure. The stacking registry was forced at selected points from the experimental picture. The image is composed of several separate calculations surrounding the observed dislocations from both sides.

Due to the broken inversion symmetry in TMDs, there are two distinct aligned stacking configurations termed R (zero-degree alignment between the two layers, also termed AA stacking in the literature) and H (180-degree alignment between the two layers, also termed AB stacking). When a twist angle is present between the layers, the atomic registry between the two layers varies periodically in space[53]. For nearly R-stacked twisted bilayers, three of the high-symmetry stacking orders that are present in the sample are shown in figure 3.1a, termed MM', MX', and M'X respectively. Here M and X refer to the metal and chalcogen atoms in the top layer, while M' and X' refer to those in the bottom layer; MM' refers to the stacking where the metal atoms of the top layer are in vertical registry with the metal atoms from the bottom layer. For nearly H-stacked bilayers, the corresponding high-symmetry stackings are XX', MX'and MM' as shown in figure 3.1b.

3.2 Structural Properties

Monolayers of WSe_2 and $MoSe_2$ were obtained by mechanical exfoliation from self-flux grown bulk crystals[42]. The relative orientation between two TMD monolayers was determined by second harmonic generation(SHG). We used polypropylene carbonate (PPC) to pick up an h-BN flake, few-layer graphite, and WSe_2 and $MoSe_2$ monolayers, respectively, using a high-precision rotation stage. In the final stage, the sample was flipped on a Si/SiO2 substrate at elevated temperature 120° C. SHG measurements were used to determine the crystal orientations of WSe_2 and $MoSe_2$ monolayers. Linearly polarized femtosecond laser light (Spectrum Physics Tsunami, 80MHz, 800nm, 80 fs) was focused onto a monolayer with a ×100 objective (Olympus LMPLFLN100X). The reflected SHG signal at 400nm was collected using the same objective and detected by a photomultiplier tube (Hamamatsu R4220P) and recorded with a photon counter (BK PRECISION 1823A 2.4GHz Universal Frequency Counter). CVD grown triangular shape monolayer MoS_2 (2D Layer) were used to calibrate the SHG setup. STM and STS data were acquired at room temperature in ultra high vacuum conditions. A lock-in amplifier with modulation of 25 meV and 917 Hz was used for dI/dVspectroscopy measurements. Shown in figure 3.1c and 3.1d are STM topographs

of samples at twist angles of ~3° (near R stacking) and ~61.7° (near H stacking) respectively. We can see that the two stacking orientations present very different structures as visualized in STM. In order to understand this difference, we calculate the relaxed structure of twisted bilayers based upon a continuous mechanical relaxation model (details in methods)[71, 72, 73]. The results of these calculations are shown in figure 3.1e and f for the same angles as shown in figure 3.1c,d. For samples near R stacking, the MM' stacking is an energetic maximum, while both the MX' and M'X stackings are minima that are close to each other in energy (in our case, the chemical identity of M=Mo, M'=W, X=X'=Se). Consequently, the twisted bilayer shows topographic contrast with the MM' region (red dot, figure 3.1c) displaying a larger topographic height while the MX' (green dot) and M'X (blue dot) regions are minima in height. For samples near H stacking, the XX' stacking is most energetically unfavorable, while the MX' is the global minimum and the MM' is a local minimum. As a result, the XX' stacking (red dot, figure 3.1d) region shrinks in size while the MX' (blue dot, figure 3.1d) region expands and the MM' has an intermediate area (green dot, figure 3.1d). We also see quite clearly for this moiré wavelength (~11 nm) that lattice reconstructions result in fairly sharp triangular domain boundaries between the MX' and MM' regions. All of these together allow us to clearly identify the various stacking configurations in our STM topograph in figure 3.1d, as indicated in the figure. We see that samples that are near H stacking present a completely different structure than samples near R stacking, which has not been studied by STM previously. For the rest of this work, we focus exclusively on this case.

At moiré wavelengths of close to 10 nm near H-stacking, the moiré unit cell shows regions of MX and MM' stacking which are approximately equal in area, resulting in a triangular lattice moiré pattern as shown in figure 3.1d of the main text. As the wavelength increases beyond ~ 15 nm, the MM' regions shrink in size to soliton lines, with nearly the entire moiré unit cell occupied by the MX' stacked regions. The moiré pattern then resembles a honeycomb lattice. The transition between the triangular and honeycomb regions is seen in figure .

Having understood the details of the moiré pattern at small length scales, we proceed to perform STM measurements over large areas of nearly H-stacked samples. One such topograph is shown

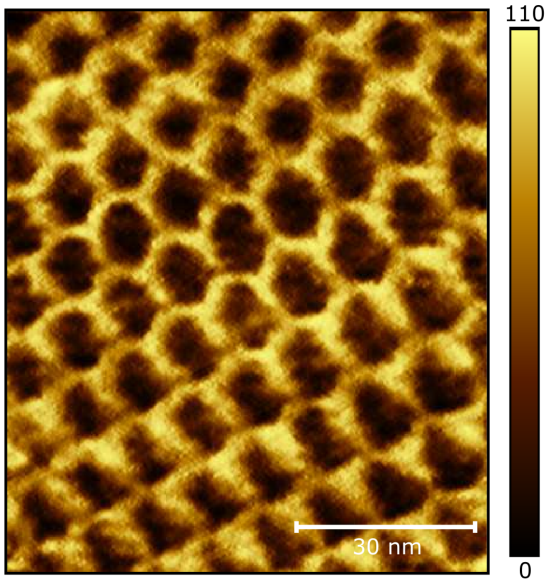

Figure 3.2: Honeycomb lattices formed by the shear strain instead of triangular lattice seen at a small angle (in *pm*).

in figure 3.1g, over an area of 500x500 nm^2. This topograph shows many interesting features, including a spatially varying moiré period, large (> 100 nm) regions of uniform MX' stacking, and one-dimensional solitons. Interesting electronic and optical properties have been reported in these 1D solitons[74, 75, 76]. Point defects in the individual layers are seen as white dots of atomic dimensions, and edge dislocations in the moiré lattice are also observed, presumably due to impurities between the two layers of the bilayer. These features arise from the presence of impurities and non-uniform strain over this area. All of this disparate behavior can be captured with the continuum mechanical relaxation calculation shown in figure 3.1h. The only inputs (beyond those of the periodic case shown in figure 3.1f) that go into this calculation are the locations and stacking registry of selected XX' stacking points. Given this information, a detailed spatial account of the relaxed structure is resolved. Due to the existing dislocations, the process was repeated surrounding dislocations from different sides to generate the integrated map of figure 3.1h . We find that this process captures the entire complex structure of the moiré pattern, and can be used to quantitatively estimate the local strain fields producing inhomogeneities in the large scale structure in figure 3.1g.

Here we provide the details of the calculation of Figure 3.1h. Figure 3.1h presents a mechanical

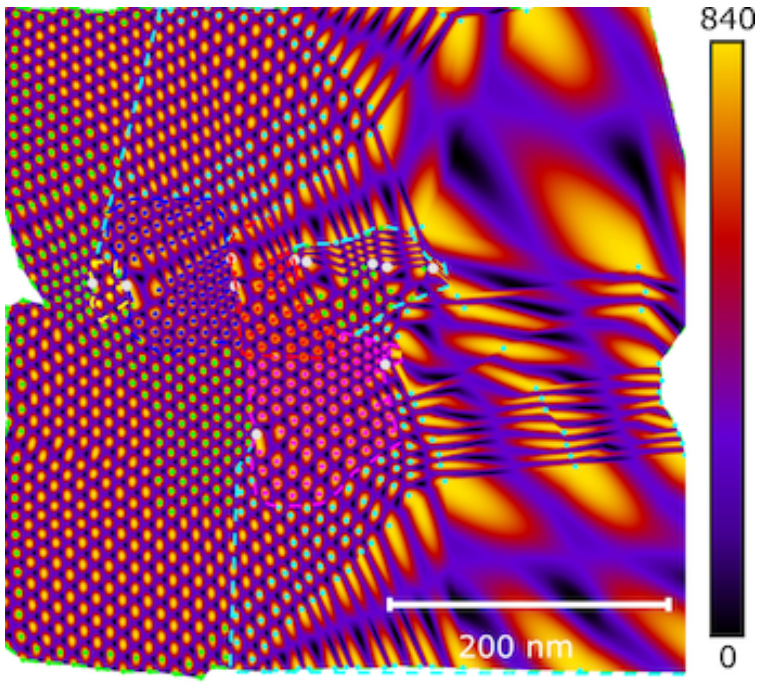

Figure 3.3: Initial and boundary conditions for the simulation presented in figure 3.1h. The white circles mark locations of dislocations appearing in the measurement of figure 3.1g. The simulation area was divided into 5 regions, marked by dashed lines with different colors. In each region, the colored dots mark the positions of points where XX' stacking configurations were forced. The false-color shows the stacking energy density (in meV/nm^2) of the initial configuration, used as a starting point for the simulations. The solution of figure 3.1h is a result of stitching these 5 calculations.

relaxation calculation aiming to reproduce different non-uniform related strain features that were measured in figure 3.1g. Beyond the intrinsic system properties, namely the generalized stacking fault energy function (GSFE) lattice constants and elastic properties for this system (see methods section), the simulation uses as initial and boundary conditions the locations and stacking registry of selected XX' stacking points. Here we provide further details about this process. Figure 3.3 presents the initial and boundary conditions used to construct figure 3.1h. The white circles mark locations of dislocations appearing in the measurement of figure 3.1g. The dislocations are lattice defects and are not directly supported by the model. However, locally the simulation can still account for the strain maps and stacking configurations. Therefore, the calculation was divided into several separate calculations, surrounding the dislocations from different orientations (regions marked by dashed lines with different colors). In each region, the colored dots mark the positions of points where XX' stacking configurations were forced for a given simulation. The false-color shows the stacking energy density of the initial configuration, used as a starting point for the simulations, which was generated as an interpolation between the forced stacking configurations. The solution of figure 3.1h is a result of stitching these 5 calculations.

3.3 Wavelength Dependent Properties

3.3.1 Topography

We now proceed to examine the structure of the moiré pattern at various length scales. Shown in figure 3.4a-e are a sequence of topographs obtained in regions with increasing moiré length scales. At the smallest of these length scales ($\sim$ 6 nm, figure 3.4a), the moiré pattern features nearly equal regions of MX' and MM' stacking. As the size of the moiré wavelength increases (figure 3.4b-d), the area of the MM' stacked region decreases at the expense of the area of the MX' stacking region. For moiré wavelengths that are larger than 20 nm, the MM' region shrinks to a shear soliton of width approximately $\sim$ 4 nm. Above this wavelength, moiré patterns resemble honeycomb lattices formed by the shear solitons rather than the triangular lattices seen at small wavelengths. The large moiré wavelengths are extremely susceptible to small amounts of strain,

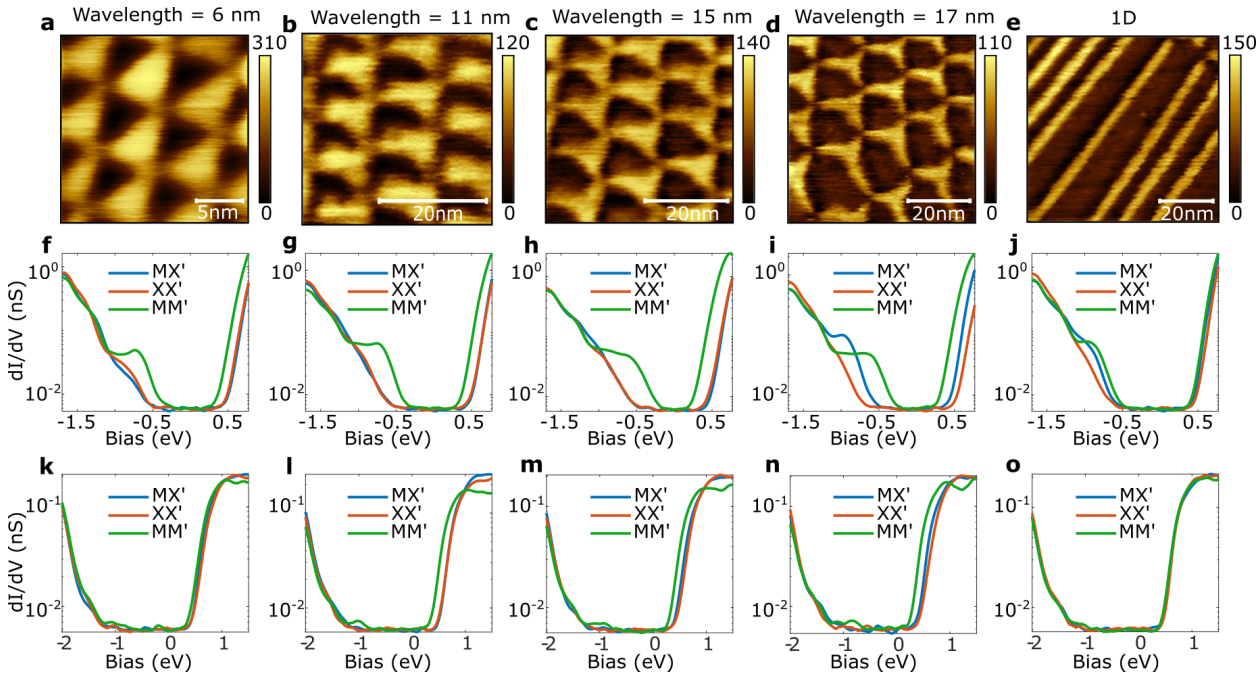

Figure 3.4: Spectroscopic properties of moiré patterns of different wavelengths **a-e** STM topographic images (in *pm*) of moiré patterns of different wavelengths (set points of -1.7 V and 100 pA). As the wavelength is increased, the area occupied by the MM' stacking configuration (brighter area) reduces, leading to a transition from a triangular lattice at a small wavelength to a strain-soliton structure at a large wavelength. **f-j** dI/dV measurements obtained at the high symmetry stacking configurations for each of **a-e**. It is clearly seen that the MM' stacking configuration displays the smallest band gap, with both the conduction and valence edges shifted towards the Fermi level relative to the M-X' stacking configuration. **k-o** dI/dV measurements obtained over a larger energy range. We can see the band edge of the conduction band clearly, and at high negative energies the states from the $MoSe_2$ valence bands that dominate the tunneling. The valence bands nearest the Fermi level that are seen clearly in **f-j** are much smaller in conductance on this scale, and are not seen clearly.

which can distort the honeycomb structure severely. An example is shown in figure 3.4e, where the individual honeycomb cells have been distorted to form quasi-rectangular strips of MX' stacking that are separated by soliton domain walls.

3.3.2 Spectroscopy

We now consider the spectroscopic properties of samples exhibiting different moiré wavelengths. Shown in figure 3.4f-j are measurements of the differential conductance (dI/dV) obtained at the three high symmetry locations of the moiré lattice, viz. XX', MM' and MX' for the moiré patterns shown in figure 3.4a-e respectively. Clear and systematic differences are seen in the spec-

troscopic properties of the different sites within the moiré unit cell. It is seen that the edge of both the valence band and the conduction band are closest to the Fermi level for the MM' site for all of the moiré wavelengths. The difference in valence band edges between the MM' and MX' regions reaches a maximum at a moiré wavelength around 13 nm(figure 3.4c), and decreases for both smaller and larger moiré wavelengths. Similar behavior is observed for the conduction band edges. The wavelength at which the moiré potential is largest corresponds structurally to the length scale where the MM' region transitions from a triangular region to a soliton. The valence band edge observed in figure 3.4f-j is derived from the states with primarily WSe_2 character, while the conduction band edge states are derived from states with primarily $MoSe_2$ character[53]. The states with WSe_2 character have a small tunnel matrix element due to the larger physical distance from the STM tip. The conduction band states, therefore, have a much higher intensity than the valence band states shown in figure 3.4f-j. Spectra taken over a wider bias range, shown in figures 3.4k-o show clearly the conduction band edges as well as deeper valence band states that are derived from the $MoSe_2$ layer. We use these spectra to define the edges of the conduction and valence bands. The spectroscopic differences between the various regions of the moiré unit cell described above are easiest to understand by considering a single moiré unit cell of a single layer. Within this unit cell, a moiré potential energy exists that shifts the location of the band edge. Thus, the moiré unit cell can simply be considered to be a problem of a triangular quantum well with finite depth. Within a single unit cell, this gives rise to a number of confined quantum dot states [66, 72]. At low energy, the states are localized inside the well while at energies above the well depth, the states are found outside the well. At room temperature, we average over closely spaced states and instead see a band edge both inside and outside the quantum well. The difference in the band edge positions inside and outside the well is then simply equal to the well depth, ie, the magnitude of the moiré potential. Our spectroscopic results indicate that the MM' region of the moiré unit cell is the region with a potential minimum for both the valence and conduction band, ie, the low energy physics of this system is dominated by electrons or holes trapped within these regions. A cursory inspection of figure 3.4f-j also reveals that this trapping potential is large - around 300 meV at its

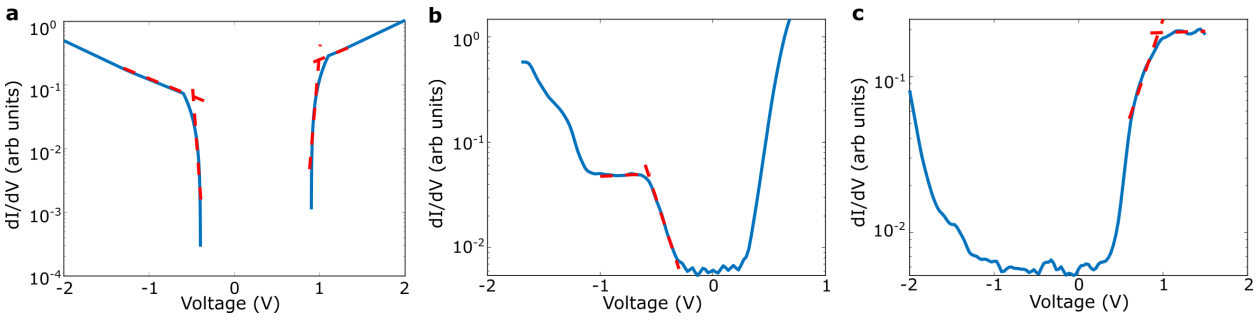

Figure 3.5: **a** Theoretical calculation of the temperature-broadened differential conductance of a semiconductor with valence band edge at -0.5 V and conduction band edge at +1.0 V. The dashed lines are linear fits to the spectrum above and below the band edges, and the crossing points mark the position of the band edges. **b,c** Determination of the valence and conduction band edges from typical experimental spectra following the procedure outlined in a.

largest in the valence band, and 100 meV for the conduction band. This consideration becomes especially interesting for large moiré wavelengths, where the MM' regions shrink to soliton lines. Our results indicate that carriers are confined to these one-dimensional lines at low energies in these structures. This quantum well picture that is based on a single moiré unit cell is only slightly modified by the periodic boundary conditions imposed by the moiré pattern - the coupling between neighboring wells broadens each of the eigenstates within the well to a "flat band" with a width determined by inter-well coupling[60].

3.4 Spectroscopic Imaging

Here we first discuss the band edge extraction and implement this method in the spectroscopic map analysis to gain insight into the moiré potential variation across the sample.

3.4.1 Band edge Extraction

In two dimensions, the density of states $\rho_S(E)$ of an ideal semiconductor with a single valence and conduction band at T=0 features sharp band edges with a constant value of the DOS beyond the band edge. Our experiments are carried out at room temperature, which results in a broadening of the edges due to the Fermi distribution of electrons in the tip and sample at non-zero temperature. The expression for the differential conductance of the tip-sample junction is given by

$$\frac{dI(V)}{dV} = \int_{-\infty}^{+\infty} \rho_S(E + eV) \frac{df(E)}{dE} \, \mathrm{d}E \tag{3.1}$$

where $f(E)$ is the Fermi-Dirac distribution at the temperature of the measurement. The result of this process is shown in figure 3.5a for a hypothetical semiconductor with a valence band edge at -0.5 eV and conduction band edge at 1.0 eV. The sharp band edge develops a finite slope due to temperature broadening at non-zero temperature. A simple practical method that we adopt to define the band edges is also shown on this plot, by drawing intersecting straight lines below and above the gap edge. The use of this method is shown in practice on real data in figures 3.5b and 3.5c for the valence and conduction bands respectively. We note that the accuracy of this process is not limited by the temperature broadening of the spectrum - the determination of the band edge is ultimately set by the signal-to-noise ratio of the measurement.

3.4.2 Spectroscopic Map

In order to understand the systematic evolution of the moiré potential as a function of moiré wavelength, we can utilize strain-induced inhomogeneity in the sample to our advantage. Shown in figure 3.6a is a region of the sample where the moiré wavelength interpolates continuously between a minimum of 5 nm to (> 20 nm). We proceed to take dI/dVspectroscopic measurements at every point on a 256x256 pixel grid in the area bounded by the dashed box in figure 3.6a. For each spectrum, we determine the edge of the valence band and the edge of the conduction band and plot their values in figures 3.6b and c respectively. We use this information, together with the areas of the individual moiré unit cells to plot the conduction and valence band edges as a function of moiré wavelength in figure 3.8d. The scatter in this figure primarily arises from the fact that different moiré triangles in figure 3.6a have differing shapes and thus display slightly different properties when represented by a single length scale. The trends shown in figure 3.6d confirm the selected point spectra shown in figure 3.4 - the non-monotonicity of the band edges as a function of moiré wavelength from figure 3.4 is clearly confirmed in figure 3.6d in a much more extensive data set.

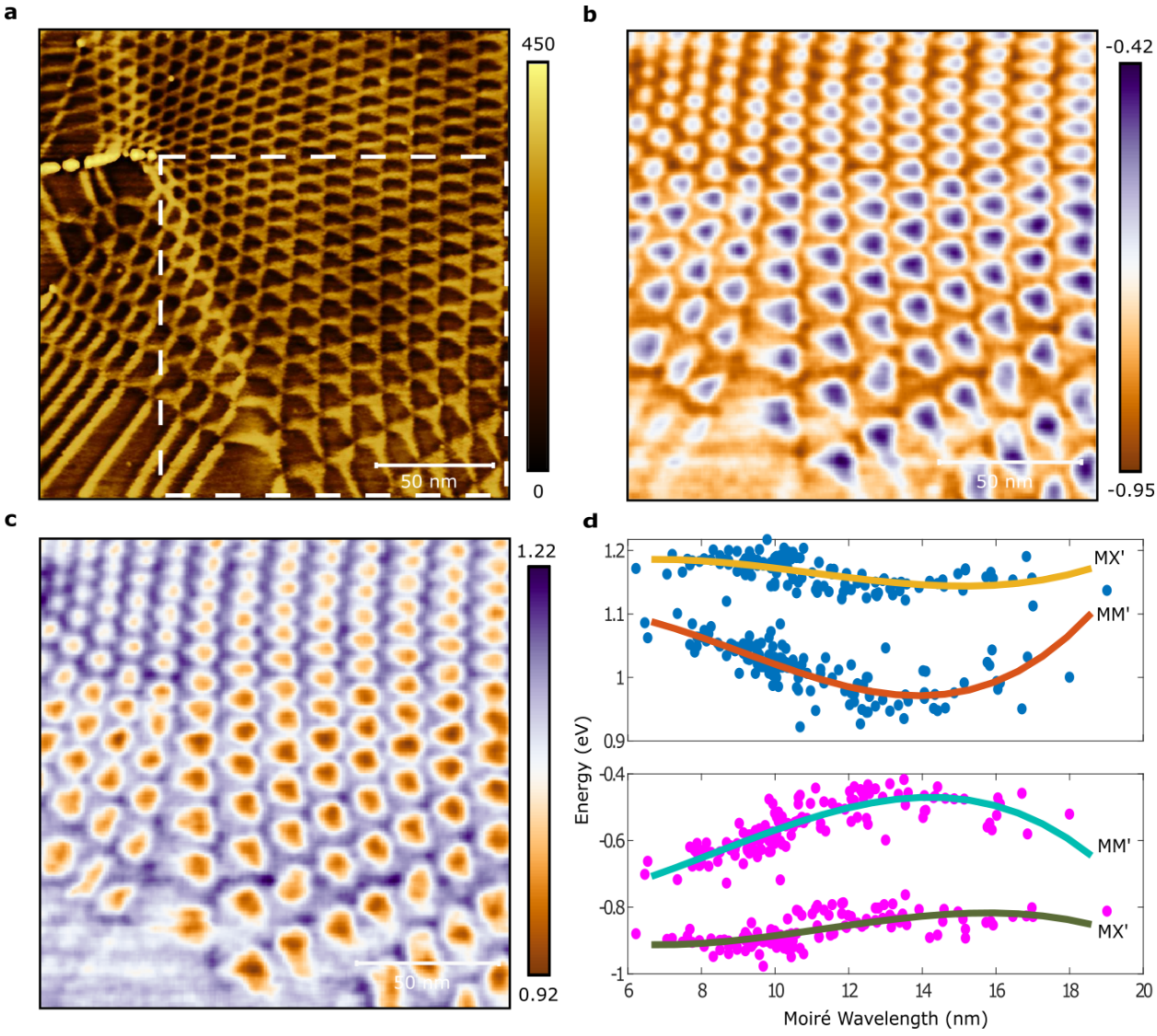

Figure 3.6: Spectroscopic imaging of conduction and valence band edges **a** Topograph (in *pm*) of a non uniform moire region (set points of -1.7V and 100 pA) **b,c** Valence and Conduction band edge maps (in *eV*) obtained in a uniform 256x256 grid within the dashed box shown in a. **d** Extracted positions of the band edges in the MM' and MX' configurations from the maps in **b,c**. These are plotted as a function of moiré wavelength calculated from the area of each moiré unit cell. The solid lines are fifth order fits to the data.

3.5 Strain Analysis

Having obtained separately the conduction and valence band edges for the MM' and MX' sites in figure 3.6, we can utilize this information to extract the moiré potential as a function of wavelength, which is simply the energy difference in band positions between a MM' region and its MX' neighbors. This is plotted in figure 3.8a for both the conduction and valence bands. We can see clearly that the moiré potential is large and non-monotonic for both the conduction and valence band edges. In previous theoretical considerations, the hybridization between the two layers of the heterostructure has been considered to play a dominant role in the moiré potential[77]. For $WSe_2/MoSe_2$, the hybridization differences between bilayers with uniform MM' and MX' stacking order are small (of order 10 meV), and thus there has been a theoretical expectation that the moiré potential is also similarly small in magnitude. Our results indicate that the true moiré potential is far larger than estimations based on uniform stacking order. Some insight into this difference can be gained from previous STM experiments on moiré patterns in TMD bilayers [65, 66, 68, 78]. In all of these works, the observed moiré potential is significantly larger than the expectation based on stacking order alone. This is the case even though these various experiments are on different materials from ours and also are in the R stacking configuration. The common feature of all of the works (including ours) is that real moiré patterns feature structural distortions in both the lateral and vertical dimensions - these distortions must, therefore, be dominating the moiré potential.

3.5.1 Atomic Relaxation Simulation

Modeling of the atomic relaxation of twisted $MoSe_2/WSe_2$ was performed within a continuity model following the method presented in [79], but solved in real space. In this model, the total energy of the system is taken as the sum of elastic energy and a stacking energy term. The total energy was minimized in search of the inter-layer real space displacement field corresponding to the relaxed structure. The stacking configuration at selected XX'-stacking points was imposed as a boundary condition to account for a specific case under study. In the periodic case (Fig.

3.1e-f and Fig. 3.8c-d) four such boundary conditions were used to impose a fixed external strain condition. In the case of a non-uniform strain map as in Fig. 1f, such points were needed wherever the moiré superlattice deviated from a uniformly periodic structure. Special care was needed to describe the 11 dislocations in the image. For each dislocation, the structure was relaxed using two registry maps for the XX'-stacking cites, as to describe both sides of the dislocation. The stacking energy maps were later stitched to for Fig. 3.1h. The mechanical relaxation parameters for the $MoSe_2/WSe_2$ heterostructures were calculated using DFT as implemented in the Vienna *ab initio* simulation package (VASP) version 5.4.4 [80]. All geometries included a vertical (c-axis) of 25 Å to ensure no interaction between periodic images.

The colinear spin-polarized electronic structure was calculated with a plane-wave cutoff of 500 eV, the VASP PAW PBE potentials (v54) [81], a broadening of 50 meV, and a self-consistency convergence criterion of 10^{-6} eV. A periodic dipole correction in the c-axis to the total energy was included, and the van der Waals functional DFT-D3 (V3.0) was used [82]. The bulk modulus (K) and shear modulus (G) for each material were calculated by applying isotropic or uniaxial strain to a monolayer lattice, ranging from -1.5% to 1.5% in units of 0.3%, and then performing a quadratic fit to the strain-dependent energies. The generalized stacking fault energy function (GSFE) coefficients are extracted from a 6×6 sampling of the configuration between layers, with the vertical positions of the atoms relaxed at each configuration until all forces are less than 20 meV. The Fourier components of the resulting energies are then extracted to create a convenient functional form for the GSFE used to describe the stacking energy term in the atomic relaxation calculations. The resulting GSFE coefficients and elastic coefficients used for the mechanical relaxation calculations were (following nomenclature of [79] and units of $\frac{meV}{u.c.}$): $MoSe_2$: K=40521, G=26464 WSe_2: K=43113, G=30770 c_0=42.6, c_1=16.0, c_2=-2.7, c_3=-1.1, c_4=3.7, c_5=0.6 The unit-cell spacing are α=0.3288 nm for $MoSe_2$ and α=0.3282 nm for WSe_2. In all the mechanical relaxation calculations we assumed for simplicity one layer (WSe_2) to be rigid, and allow all the relaxation to happen at the other ($MoSe_2$) layer. Relaxing this condition would not affect the overall picture significantly. The periodic mechanical calculations of Fig. 3.1e, Fig. 3.1f and Fig.

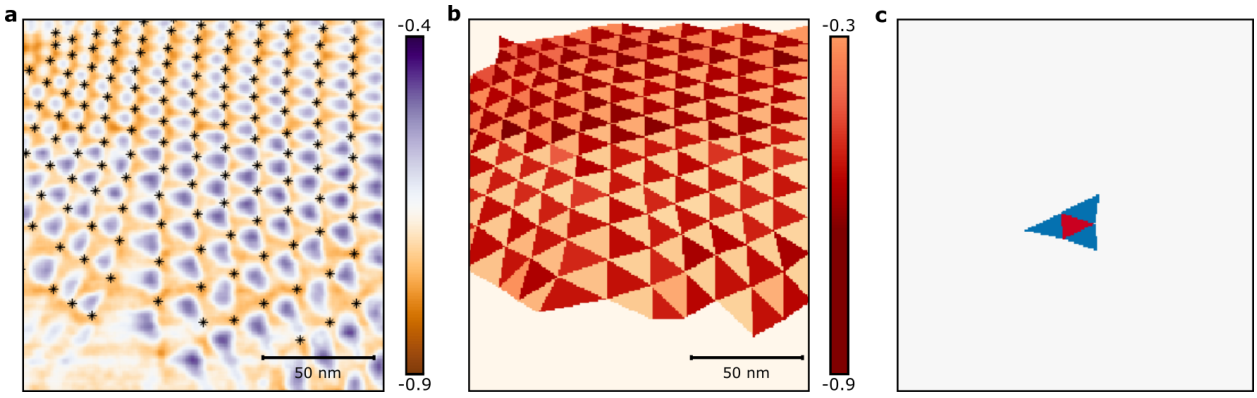

Figure 3.7: **a** XX' points of the moiré lattice shown as black markers, superposed on the spectroscopic map of valence band edges (in eV). **b** Determination of valence band edges of each MX' and MM' region after Delaunay triangulation of the XX' points in a (in eV). **c** Determination of the moiré potential. The moiré potential is defined as the absolute value of the difference between a given triangle in b (shown in red) and the average of its three nearest neighbors shown in blue.

3.8c-d assumed twist angle of 4°, 1.5°, and 1.88° and external strains of 0.13%, 0.3%, and 0% respectively, all with a Poisson ratio of 0.23.

3.5.2 Band Edge Map Analysis

In order to extract band edges as a function of moiré wavelength, we start by defining the moiré unit cells, based upon the positions of the XX' positions from the topograph in figure 3.6a. We avoid moiré unit cells that have aspect ratios larger than 2. We then use Delaunay triangulation to define the moiré unit cells from the XX' positions shown in figure 3.6a. For each Delaunay triangle, we then find the centroid, which defines the position of MM' and MX' stacking respectively. We use the spectroscopic data of figure 3.6b and 3.6c to find the band edges at these points and set this to the valence and conduction band edge values for each given triangle. The result of this procedure for the valence band edge is shown in figure 3.6b. We then take the area of the moiré unit cell and convert it to a moiré wavelength by assuming it to be an equilateral triangle in order to generate the plot in figure 3.6d. This necessarily introduces scatter into the data, since triangles with different aspect ratios have different spectroscopic properties. However, it allows us to represent the entire data set of band edges as a function of moiré wavelength.

In order to then find the moiré potential for each moiré unit cell, we take the difference in band

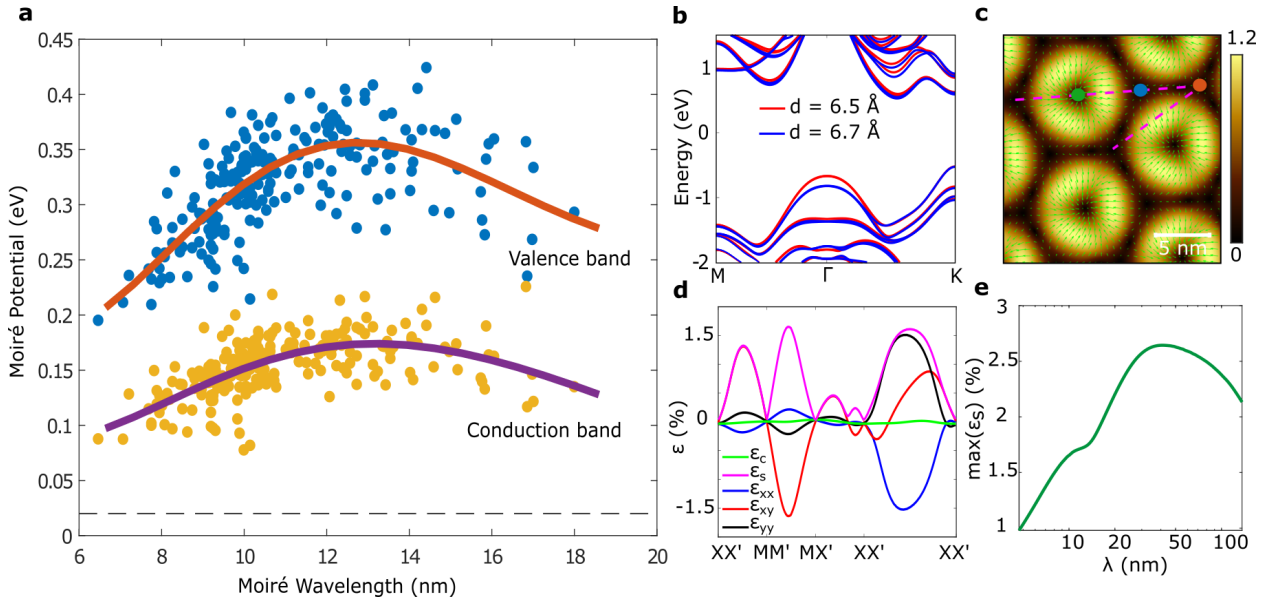

Figure 3.8: Quantifying the moiré potential **a** moiré potential as a function of moiré wavelength extracted from spectroscopic imaging experiments. Solid lines are fifth order fits to the data. The dashed line is the theoretically calculated difference in valence band edges between uniformly stacked MM' and MX' bilayers. It is seen that the experimentally measured moiré potentials are much larger than this theoretical expectation. **b** DFT bandstructure of uniform MM' stacked bilayers with the equilibrium layer separation (blue) and for a bilayer that is compressed by 0.2 . **c** Shear strain map (ϵ_s in %) from mechanical relaxation calculations of H-stacked $MoSe_2/WSe_2$ with a moiré period of 10 nm. The green arrows make a stream plot of the $\epsilon_s \cdot (\cos\phi, \sin\phi)$ field (see text for definitions of ϵ_c, ϵ_s and ϕ), providing additional information about the shear direction. Colored dots in **c** correspond to stacking configuration marked in Fig. 1. **d** Strain tensor components (ϵ_{xx}, ϵ_{xy}=ϵ_{yx}, ϵ_{yy}) and ϵ_c, ϵ_s along the path marked by the dashed lines in **c**. **e** Maximal shear strain as a function of moiré wavelength, showing a non-monotonic behavior.

edges between each MX' region and the three neighboring MM' regions, as shown in figure 3.7c. This data is used to generate the plot in figure 3.8a.

3.5.3 Theoretical Model

Distortions within the moiré unit cell give rise to significant lateral and vertical strain. Due to the large unit cell sizes, we consider in our work, accurate ab-initio calculations of the electronic properties of the moiré are not feasible. We expect significant vertical strain to be present in the structure. For uniformly stacked bilayers, the MM' stacking configuration displays a significantly larger c-axis lattice constant in comparison to MX'(6.7 instead of 6.2). We thus expect that within the moiré structure, the MM' regions are being compressed down by the MX' regions, while the MX' regions are under the tensile strain along the c axis. These strains can give rise to significant

changes in electronic structure. Shown in figure 3.8b is a DFT calculation of the mechanical relaxation model of a uniform MM' stacked region at an interlayer distance of 6.7 A (equilibrium) and 6.5 A (compressed). This compression gives rise to about a 0.2 eV shift in the valence band position at the Γ point in a direction that is consistent with the experimental finding. In order to obtain DFT calculations, we use a slab structure to model the $WSe_2/MoSe_2$ heterostructure. To avoid artificial interactions between the polar slabs, we place two oppositely oriented $WSe_2/MoSe_2$ units with mirror symmetry in the slab. Each slab is separated from its periodic images by 15 Å vacuum regions. Our DFT calculations were performed using the Vienna ab initio Simulation Package[80]. We use the projector augmented wave method to construct pseudopotentials[81]. The plane-wave energy cutoff is 400 eV. The exchange correlation functional is approximated by the generalized gradient approximation as parameterized by Perdew, Burke, and Ernzerhof[83]. The Brillouin zone is sampled by a 30 x 30 x 1 k-mesh. Van der Waals dispersion forces between the two constituents were taken into account using the optB88-vdW functional within the vdW-DF method developed by Klimes et al [84]. We also expect significant lateral strains to be present within the unit cell, which we estimate using our mechanical relaxation model within the moiré unit cell. We write the strain tensor as $\epsilon = \epsilon_C \mathbf{I} + \epsilon_S(\cos(2\phi)\sigma_{\mathbf{Z}} + \sin(2\phi)\sigma_{\mathbf{x}})$ where ϵ_C is an isotropic compression and ϵ_S is a volume-preserving shear, and $\mathbf{I}$ is the identity matrix and $\sigma_{\mathbf{Z}}, \sigma_{\mathbf{x}}$ are the Pauli matrices in standard notation. The magnitude ϵ_S is plotted within the moiré unit cell in figure 3.8c for a moiré wavelength of $\sim$ 10 nm (ϵ_C is small at this wavelength). The total variation in strain across the unit cell is seen to be $> 3\%$ as can be seen in the line cut of strain tensor elements shown in figure 3.8d. For comparison, a uniform tensile strain of a percent changes the band gap of TMDs by $\approx$ 0.2 eV [74]. It is thus no surprise that these large values of strain in the moiré unit cell dominate the electronic properties. Fig. 3.8e shows the maximal value of ϵ_s as a function of the moiré wavelength from mechanical relaxation calculations. It is interesting to note that the shear strain also has a non-monotonic behavior as a function of moiré wavelength. This similarity in behavior to the experimentally observed moiré potential further supports the hypothesis that relaxation-induced strain is the source of the observed enhanced moiré potential. Our results show

that the moiré potential in TMD heterobilayers is substantially larger than previous expectations, and can reach values of several hundred millivolts. Such large trapping potentials can be extremely useful in confining charge carriers as well as excitons and enhancing interactions between them. At the same time, our results show that the largest moiré potentials are realized for a narrow range of angles, and engineering high-quality structures with uniform moiré lattices with these wavelengths remains an open problem.

3.6 Follow-up Works on Strain Extraction

Here, we present two follow-up works using the atomic relaxation model and the strain extraction on the STM topographic images of $WSe_2/MoSe_2$ heterostructures[85, 86]. We introduce moiré metrology as a combined experiment-theory framework to probe the stacking energy landscape of bilayer structures. Through studying the shapes of moiré domains with numerous nano-imaging techniques, and correlating with multi-scale modeling, we assess and refine first-principle models for the interlayer interaction. This method can be applied to a variety of 2D moiré materials. The generalized stacking fault energy function (GSFE), which provides the energetic variations across different stacking configurations, is the fundamental property that describes relaxed vdW interfaces[87, 88]. The GSFE is commonly calculated using density functional theory (DFT). Experimental techniques to probe the GSFE are currently restricted to the stable lowest-energy configuration and are very limited in energy resolution compared to the variability among theoretical descriptions. Here we show that the generalized stacking fault energy function (GSFE) is encoded in fine details of the relaxed moiré super-lattice patterns at the low twist-angle limit. In particular, the shape of domains and domain wall networks, as well as domain wall width, abide by transitionary configurations beyond the lowest-energy stackings of the domains. Figure 3.9 is an example showing the stacking energy density map (figure on bottom) from relaxation calculations performed on a different moiré topography obtained by STM (figure on top).

In the following, we discuss the second work to extract the strain from the STM topographic images on TMD heterobilayer. Various papers have discussed the possibility of strain tensor ex-

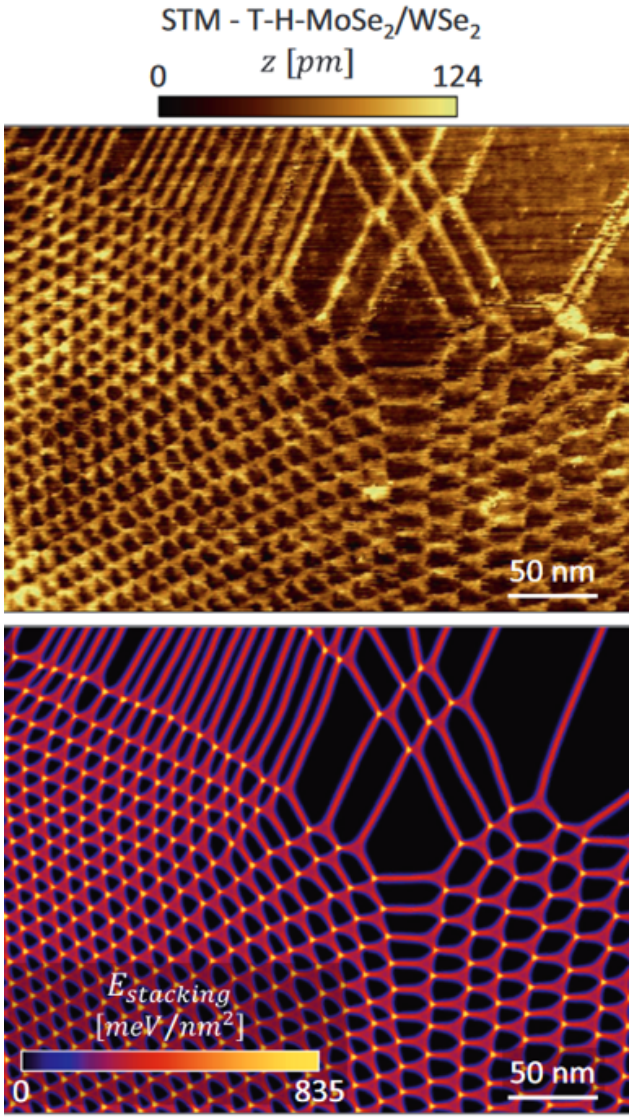

Figure 3.9: STM map of T-H-$MoSe_2$ /WSe_2 resolving MM' (bright) and MX' (dark) stacking configurations in various strain conditions. STM topography (top panel) and stacking energy density (bottom panel) from full relaxation calculations of the experimental data

traction from the observable moiré spatial pattern using different imaging techniques including scanning tunneling microscopy (STM)[89, 90, 91], piezoresponse force microscopy (PFM)[50, 92], conductive atomic force microscopy (CAFM)[93], scattering-type scanning near-field optical microscopy (s-SNOM)[85, 94], and microwave impedance microscopy[95]. Whether the strain is deliberate or spontaneously formed, it may strongly affect the system under study and, in particular, the moiré potential[89]. While the notion of strain extraction has been discussed before, there is a need for a more standardized approach to the problem. Furthermore, the limitations of what can be extracted from the moiré superlattice pattern should be clear when making such an attempt. This work[86] provides a derivation of the problem, offers a practical tool for strain and twist angle extraction from an experimentally observed pattern, as well as lay out the limitation of such an approach. The twist angle and strain map extraction scheme is demonstrated in Figure 3.10: starting from a raw STM topography of a $MoSe_2/WSe_2$ heterostructure (Figure 3.10a), through processing (Figure 3.10b), and finally the extraction of maps of the twist angle (Figure 3.10c) and the strain tensor (Figure 3.10d,e). The details of the procedure are discussed in this paper[86]. This work will be useful for the analysis of experiments in the field of twisted van der Waals heterostructures as well as prevent ambiguity by creating a standard for moiré -based strain extraction.

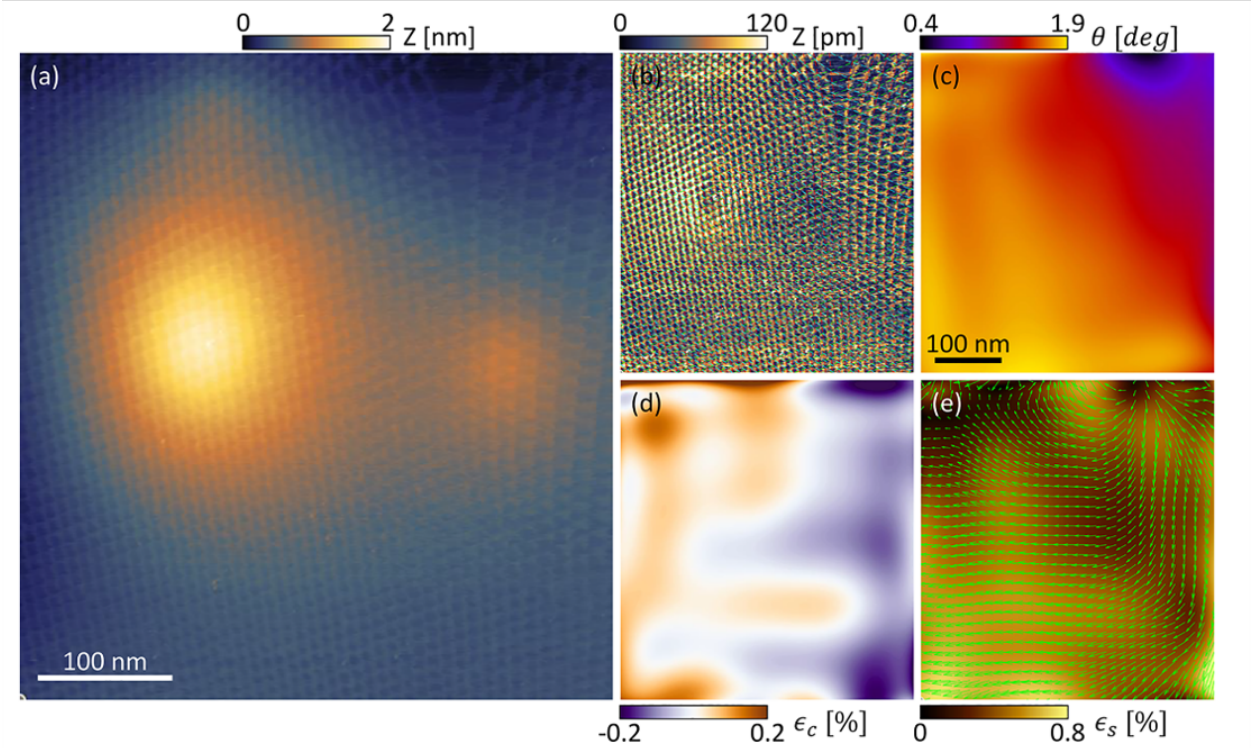

Figure 3.10: Strain and twist angle fields extraction from a spatially varying moireé superlattice map. **a** STM topography map of a twisted $MoSe_2$ /WSe_2 heterostructure. Two bubbles cause large-scale topography features over which the moiré superlattice is apparent. **b** Data of (a) after background, subtraction to highlight moireé. **c-e** Using a common choice of ψ_0, defined by the lattice orientation of layer 1 connecting two A sites, the maps for θ, the twist angle (c), the compression strain ϵ_c **d**, and the shear strain ϵ_s **e** were extracted. The vector field $\epsilon_s(\cos\gamma + \sin\gamma)$, where γ is defined as the strain tensor angle, is overlaid on top of the map of ϵ_s in (e). Panels c-e share a scale bar.

Chapter 4: Ultralocalized Optoelectronic Properties of Nanobubbles in 2D Semiconductors

In the previous chapter, we demonstrated that $WSe_2/MoSe_2$ heterobilayers host a deep periodic potential generated by moiré patterns and offer an excellent platform for carrier confinement. Strain and electric fields are considered as other effective methods to achieve highly confined carriers such as excitons in the TMD bilayers[96, 97, 98, 74, 99, 100, 101]. Previously, researchers have modified the optical properties of transition metal dichalcogenides on a nanoscale by using both mechanical and electrical nanostructuring. However, there has been no clear experimental understanding of the relationship between the local electronic structure and emission properties in these structures. In this chapter, we examine the nano-bubbles present in the same heterobilayer studied in the previous chapter as a test bed to achieve high mechanical and electrical fields, employing scanning tunneling microscopy (STM) and near-field photoluminescence (nano-PL) to investigate their electronic and optical characteristics. We demonstrate through tunneling spectroscopy that there are electronic states deeply localized in the gap at the boundary of these bubbles, which remain unaffected by chemical defects in the layers. Additionally, we illustrate that there is a considerable change in the local bandgap near the bubble's edge, which evolves continuously over approximately 20 nm. Nano-PL measurements also reveal a consistent redshift in the interlayer exciton upon entering the bubble, in agreement with the band-to-band transitions detected by STM. Using self-consistent Schrodinger-Poisson (SP) simulations, we capture the core of the experimental findings and identify that strong doping in the bubble region, in combination with mechanical strain, is necessary to achieve the observed localized states. The ability to engineer the electronic and optical properties of TMDs to achieve quantum emitters offers a promising route for developing advanced optoelectronic devices.

4.1 Introduction

Two-dimensional (2d) transition metal dichalcogenides (TMDs) have been investigated as a possible route toward producing well-controlled optical emitters, critical components in quantum technologies and photonics [102, 103, 104, 105, 106, 56, 107, 99, 108, 109, 100, 110]. The bandgap of monolayer TMDs is uniquely sensitive to doping[96, 97, 111, 112, 113], dielectric environment[114] and mechanical strain[98, 74, 99, 100, 101], thereby providing an ideal platform to create quantum confinement by local mechanical and electrical fields. Indeed, previous research has investigated moiré patterns [115, 116, 89, 75, 117], wrinkles [105, 103, 99], bubbles [102, 118] and lithographically fabricated dielectric arrays as effective methods [119] to create localized optical emitters. In spite of these notable achievements, a basic band diagram picture across such localized structures remains elusive. For example, recent theoretical calculations[120, 119, 121] have predicted large bandgap changes at the edges of wrinkles and nanobubbles. However, such predictions have not been experimentally verified, and it remains unclear what the major contributors are to achieving localized optical emitters in TMD materials.

In order to address these questions, high spatial resolution spectroscopic measurements across local perturbations in TMDs are necessary. Our approach is to use the local imaging and spectroscopic capabilities of scanning tunneling microscopy(STM) to measure the local band diagram across nano-bubbles, and directly correlate these measurements with near-field optical measurements with 10 nm spatial resolution.

4.2 Device Fabrication

Samples were prepared using mechanically exfoliated monolayers of WSe_2 and $MoSe_2$ from high-quality flux synthesized crystals[122]. We first describe the STM device. The heterostructure was stacked by the dry stamp method. A transparent polydimethylsiloxane (PDMS) stamp coated by a thin layer of polypropylene carbonate (PPC) was used to pick up a thin layer of exfoliated h-BN. This h-BN was then used to pick up few-layer graphite, and then the h-BN/graphite stack

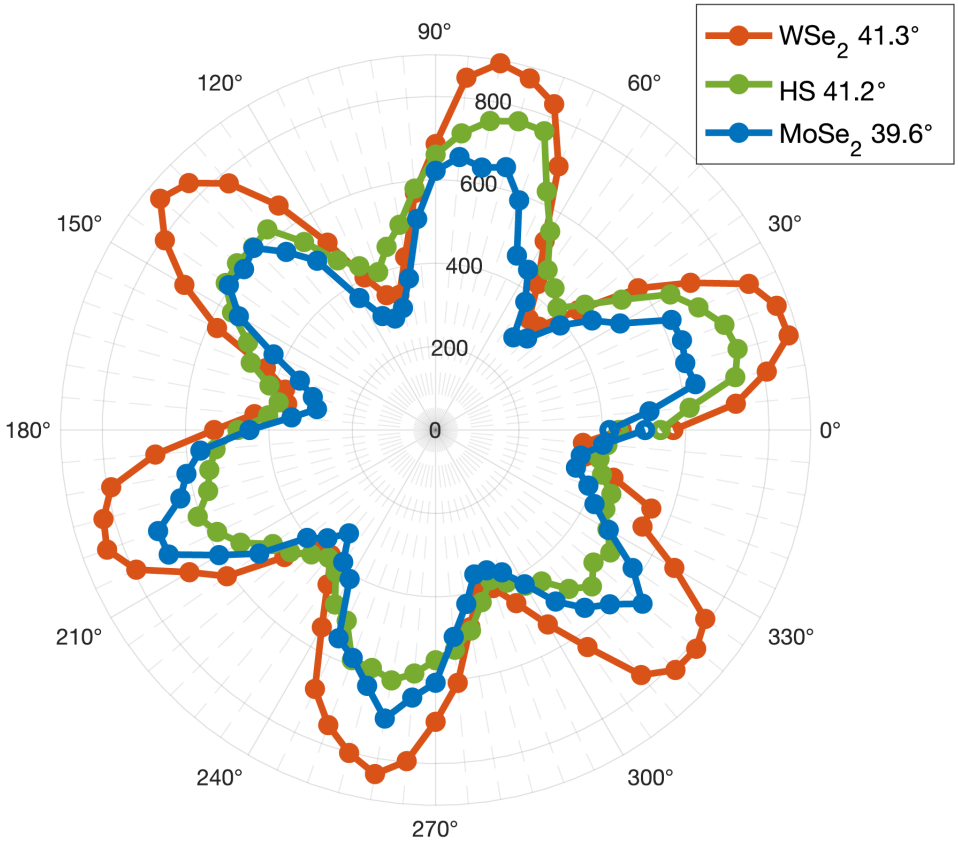

Figure 4.1: Polarization-resolved SHG signal of monolayer WSe_2, $MoSe_2$ and HS regions after stacking. HS region shows a weaker SHG signal, which indicates a near 60 degrees (H stacking) with 1.7 degrees twist angle.

was used to pick up the first TMD monolayer, WSe_2. The second TMD monolayer, $MoSe_2$, was ~ 1.7 degrees twisted and picked up by the first monolayer on a rotation stage. Second harmonic generation (SHG) as described later in this section was used to determine the relative orientation between WSe_2 and $MoSe_2$, prior to the pick up which is described in the next section. We peeled off the PPC film with the whole stack on top of it from the PDMS stamp. Then, the h-BN/graphite/WSe_2/$MoSe_2$ stack was 'flipped' from the original stacking order and transferred onto a clean silicon chip on a hot plate at 120° C. After flipping the stack, from top to bottom our stack includes $MoSe_2$/WSe_2/graphite/h-BN. Finally, we used the fields metal to make electrical contact with graphite. To fabricate Nano-PL device, monolayer WSe_2 and monolayer $MoSe_2$ were stacked using a polycaprolactone (PCL) stamp[123]. The bilayer stacks were then transferred onto template stripped gold substrates and the PCL was dissolved to create the final device.

In the following, we describe the SHG method used in this work. We did SHG to determine the crystal orientation of monolayer WSe_2 and $MoSe_2$ before and after stacking. The azimuthal angular (θ) of SHG intensity was acquired by rotating the laser polarization and the SHG signal by a half waveplate at a fixed sample orientation. Due to the D_3h symmetry, the non-vanishing tensor elements of the second order susceptibility of WSe_2 and $MoSe_2$ monolayers are $\chi^{(2)}_{yyy} = -\chi^{(2)}_{yxx} = -\chi^{(2)}_{xyx} = -\chi^{(2)}_{xxy}$ where the x axis is defined as the zigzag direction. When we simultaneously rotated the fundamental (laser) and SHG signals, the SHG intensity showed six- fold symmetry. CVD-grown monolayer $MoSe_2$ was used for calibration of SHG signal. To confirm the twist angle and stacking configuration (H or R stacking), we did SHG on stacked samples, including not overlapped monolayer regions and overlapped HS regions. The twist angle can be found by the difference of crystal orientation of individual monolayers, and the stacking configuration can be found by comparing the SHG intensity of HS regions with the monolayer regions. In the case of R stacking, the SHG intensity of the HS region is strongly enhanced compared to monolayer signals, while a weaker signal (in comparison to monolayer WSe_2) would be observed in the case of H stacking [124]. In our case, we observed a weakening of the SHG signal in the HS region indicating H stacking. The SHG data is shown in figure 4.1.

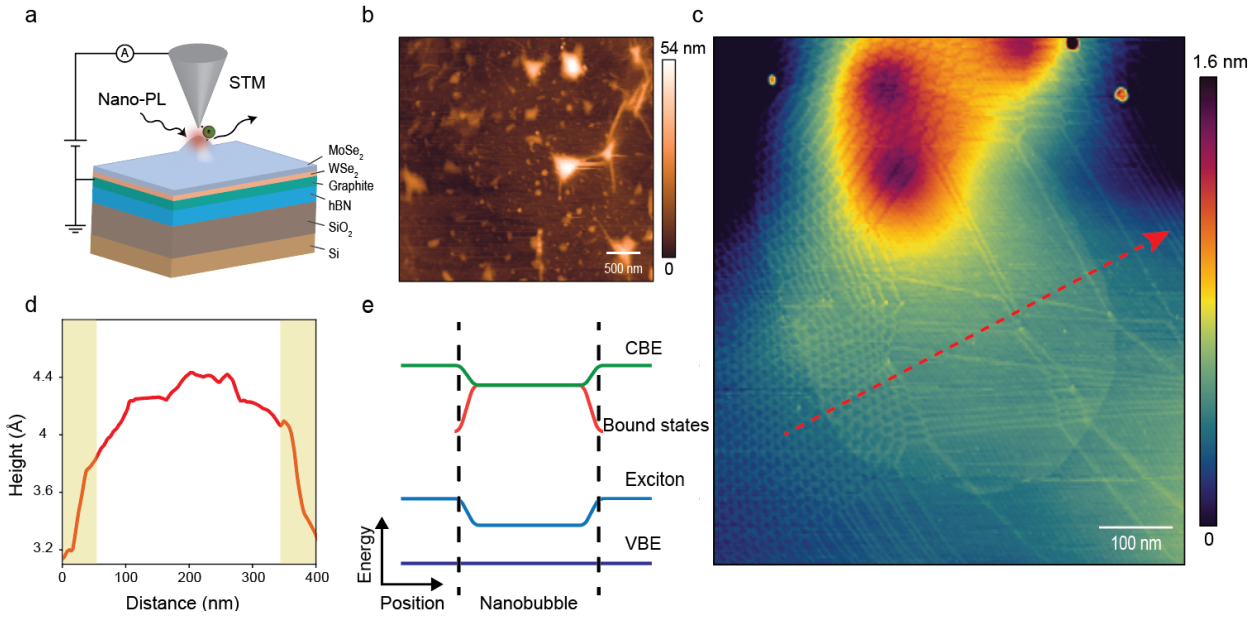

Figure 4.2: Nanobubbles in twisted $WSe_2/MoSe_2$ heterobilayers **a** Schematic of the experimental setup. **b** 3.8 micron AFM image of a $WSe_2/MoSe_2$ heterobilayer on gold substrate used in nano-PL measurements showing several nanobubbles **c** STM topographic image (V_b = -1.8 V, I = -50 pA), of a single nanobubble. The continuous moiré pattern across the nanobubble shows that contact between the two TMD layers is maintained throughout. **d** STM Height profile across the dashed arrow in (c) showing an apparent step size of 1 angstrom at the nanobubble edge highlighted in yellow. **e** Schematic band diagram of the conduction band edge (CB) , the bound states, the valence band edge(VB), and interlayer exciton energy as a function of position deduced from STM and nano-PL measurements.

4.3 Nanobubble Topography

Our STM measurements are conducted on nearly aligned (61.7 °) $WSe_2/MoSe_2$ heterobilayers that were stacked on Graphite/hBN as a conducting electrode for STM measurements (see Fig. 4.2a for a schematic). The relative orientation between two TMD monolayers was determined by second harmonic generation (SHG) (see supporting information figure S1 and accompanying discussion). During the stacking process, nanobubbles are commonly formed between layers. Figure 4.2b shows a large-scale atomic force microscopic (AFM) image of such nanobubbles. The nanobubbles range in size from 20 nm to 400 nm and in height from 2 nm to 50 nm. STM topographic measurements on one such nanobubble are shown in Fig. 4.2c.

Figure 4.2d shows the height profile of the nanobubble boundary corresponding to the dashed arrow in Fig. 4.2c. In order to obtain the STM topography, the tunneling current remains constant

at a particular voltage bias, through a feedback loop; however, the tunneling current depends on the integrated local density of states between the sample Fermi level and the bias voltage. This dependency of current on electronic structure affects the topographic data. Thus, both electronic structure and actual topographic height influence the apparent topographic height in STM and the apparent heights are not directly translatable into real vertical displacements. This consideration is not relevant to AFM measurements; however, AFM measurements are dictated by tip-sample force interactions which can strongly influence the apparent height in AFM topographic scans. However, it is clearly evident from the line profile across the boundary shown in Fig. 4.2d that the edge of the bubble features a sharp step. Such a sharp step indicates that there is the localized strain at the edge of the bubble. Finally, a moiré pattern is clearly visible both on and off the bubble. Its presence in all regions shows that the WSe_2 and $MoSe_2$ layers are in good contact throughout, and the bubble is under the heterobilayer. As a result of the device fabrication process under ambient conditions, compounds in the air such as water molecules often are trapped between layers. While the chemical identity of the material in the bubble is unknown, our data below, which shows a highly doped region on the nanobubble, indicate the presence of polarized (or ionized) molecules trapped in the nanobubble during the fabrication. Such polarized molecules induce doping and electric field to the layers above and modify the electronic structure.

STM and STS measurements were carried out at room temperature to avoid sample charging. STM tips were prepared on Au(111). For dI/dVmeasurements a lock-in amplifier was used with modulation of 25 meV and a frequency of 917 Hz.

Nano-photoluminescence measurements were performed in ambient conditions. The scanning platform was the Omegascope-R near-field optical microscope from Horiba Scientific, which was used for feedback control for the nano-PL scans, and for atomic force topographical imaging. The excitation and detection were provided by the LabRAM HR Evolution Spectrometer and Synapse II EMCCD. Nano-optical probes were the SNC-OMNI-TERS-Au probes from Applied Nanostructures. We have shown previously [118] that excitation with red-tuned lasers can preferentially excite localized excitons in nanobubbles in TMD monolayers. For this reason, excitation was per-

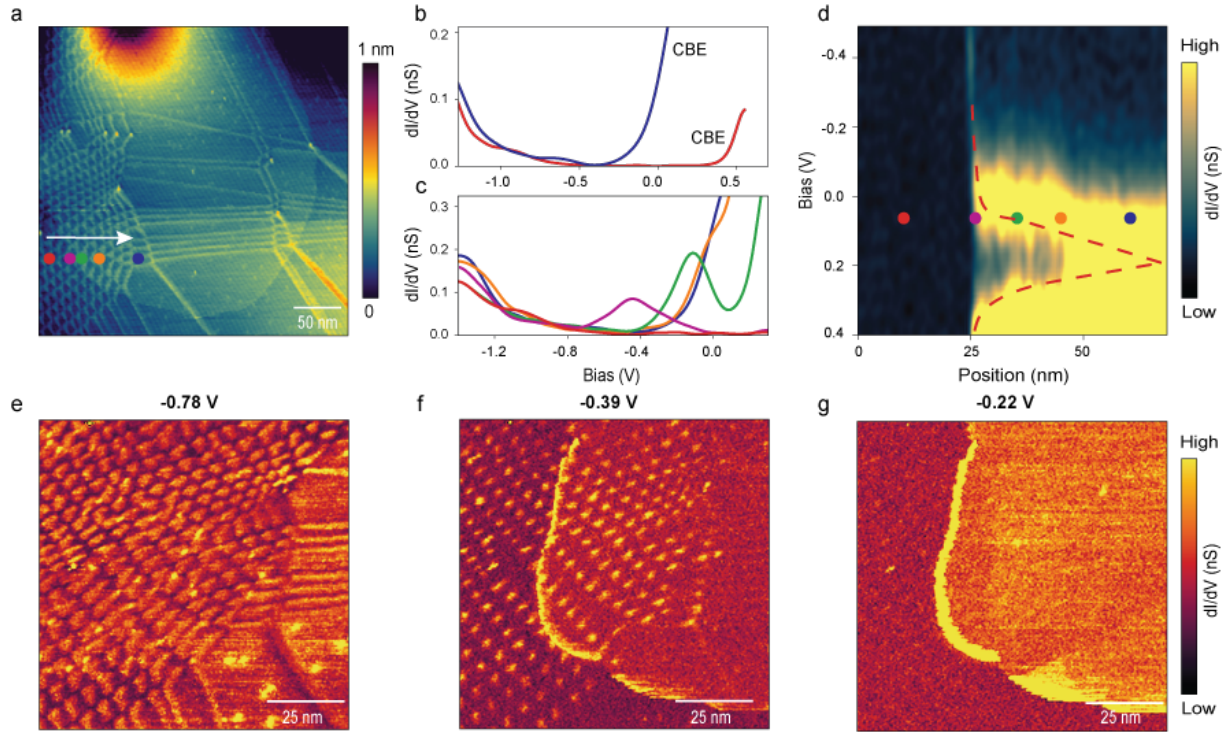

Figure 4.3: STM spectroscopic properties of nanobubbles **a** STM topography indicating locations where the point spectra shown in **b,c** were taken. **b** Point spectra taken inside (blue) and outside (Red) of the bubble show a pronounced shift of the conduction band edge (CBE) inside the bubble while the valence band is unaffected. **c** Evolution of dI/dV point spectra from the outside to the inside of the nanobubble corresponding to the markers in **a**. At the edge of the bubble, deeply localized states are seen within the semiconductor gap. **d** Heat map of position-dependent dI/dV spectra at the conduction band edge across the bubble. The dashed lines are guides to the eye that show the evolution of the bound states and the conduction band edge. **e-g** Spectroscopic maps across the nanobubble edge at energies of -0.78 V (valence band edge), -0.39 V, and -0.22 V (within the bandgap) The set points are V_b = -1.8 V, I = -200 pA. Bound states are clearly observed at the nanobubble edge at -0.39 V and -0.22 V.

formed with a 785 nm continuous wave laser from Horiba Scientific with a total power for ~50 uW delivered into the back aperture of 100x, 0.7 NA Mitutoyo long working distance objective. Scanning over the nano-bubble sample was in the 'Spec-Top' mode: integration of the optical spectrum is done while the nano-optical probe is in contact with the sample. The sample is then pulled away several nanometers before moving to the next pixel, where the process is repeated until completion.

4.4 Scanning Tunneling Spectroscopy

To characterize the electronic properties in the vicinity of the nanobubble, we perform STM dI/dV spectroscopy measurements at various points on and off the bubble (see Fig. 4.3a). Shown in Fig. 4.3b and c are a sequence of such measurements taken across the edge of the bubble, color-coded according to the markers on Fig. 4.3a. Figure 4.3b shows the typical spectra well inside (blue) and outside (red) the nanobubble area. It is seen that the conduction band (CB) edge shows a substantial shift from the outer edge of the bubble into the interior while VB is nearly unchanged. This indicates a substantial reduction in the bandgap on the bubble as well as a large electron doping.

Shown in Fig. 4.3c is a sequence of spectra taken in the transition region across the bubble edge, with a focus on the CB edge where the most dramatic changes are observed. It is seen that at the edge of the bubble (red curve), electronic states exist that are deeply bound in the semiconductor gap. As we transition from outside to inside the bubble (green curve), these states move towards the CB edge, while at the same time, the CB edge moves towards the Fermi level. The entire evolution is shown as a heat map of dI/dV in Fig. 4.3d as a function of position along the arrow overlaid on Fig. 4.3a. The dashed lines overlaid on Fig. 4.3d indicate the evolution of the localized states and the conduction band edge upon moving from the outside to the inside of the bubble.

In order to confirm that the observations above are representative of the entire bubble and not specific to a particular region, we performed spectroscopic imaging experiments across the bubble interface at various energies, a subset of which are shown in Fig. 4.3e-g. At the valence band edge (Fig. 4.3e), the map does not distinguish between the interior and exterior of the bubble, showing the uniformity of the valence band edge across the bubble. Figure 4.3f and 4.3g, taken within the semiconducting gap, show the presence of the localized states clearly, and their evolution towards the interior of the bubble. At large positive energies (not shown), these localized states merge into the conduction band, and a clear contrast is seen between the interior and exterior of the bubble. These maps confirm the basic picture provided by point spectra – the bubble region is character-

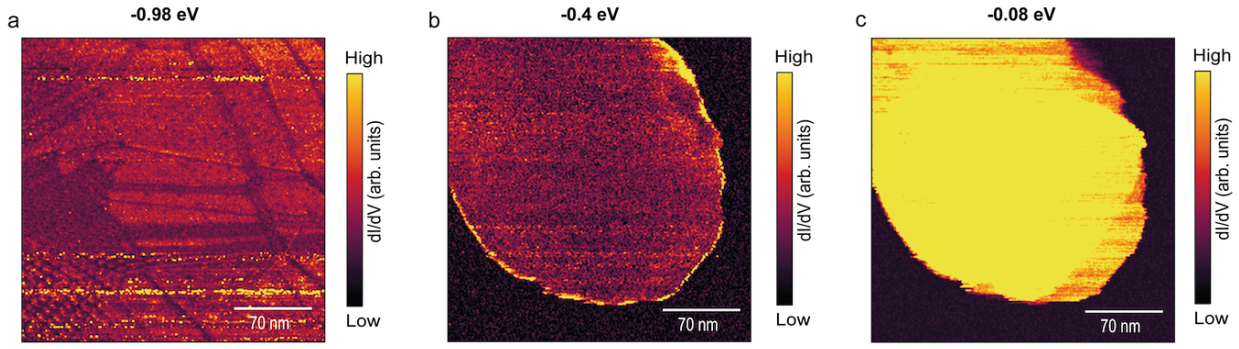

Figure 4.4: **a-c** Large scale (300 nm) spectroscopic maps from the nanobubble at various biases showing the localized states at the boundary.

ized by localized states at its edge and a shifted conduction band edge throughout. We present larger maps across the entire bubble in the supporting information, to rule out moiré effects on the observed phenomena. Finally, to rule out possible damage to the bubble during spectroscopic maps, we measure the topographic heights before and after spectroscopy is performed.

Figure 4.4a-c shows a large-scale spectroscopic map (300 nm) on the same nanobubble presented in the main manuscript at three different biases. At -0.98 V, the valence band inside and outside of the nanobubble remains almost the same. However, the localized states at the edge of the nanobubble are clear at -0.4 V, within the semiconductor gap, Fig. S2b. It is clear that the localized state exists at the nanobubble boundary, independent of the nature of the moiré pattern in specific regions. The conduction band edge shift is visible across the entire nanobubble in Fig. 4.4c. Here, we present the dI/dV maps taken from a different nanobubble on $MoSe_2/WSe_2$ heterobilayer by STM. The moiré wavelength is larger than the scan size; however, the emergence of bound states is similar to the small moire wavelength region shown in Fig. 4.3e-g. At energy close to the valence band edge, the interior and exterior of the nanobubble show almost the same density of states, Fig. 4.5a. However, inside the semiconducting band gap the localized states become apparent at the edge of the nanobubble shown in Fig. 4.5b. The conduction band shift at the interior of the nanobubble is also clear in Fig. 4.5c near the Fermi energy.

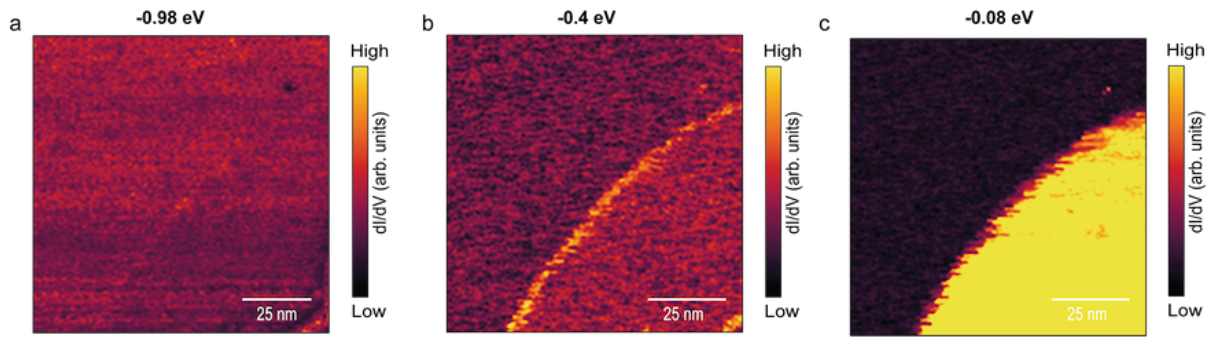

Figure 4.5: **a-c** dI/dV maps at various energies on a different nanobubble showing similar bound states and conduction band offset.

4.5 Nano-PL Spectroscopy

We next proceed to compare our measurements of the single particle spectroscopic properties of individual bubbles with their optical emission. To do this, we employed hyperspectral nanoscale photoluminescence measurements to map the changes in exciton energy across the bubble. We have previously applied this technique to the imaging of localized exciton states in transition metal dichalcogenide monolayers [118], however, the spatial resolution was limited due to the finite radius of curvature of the probe. To push the nano-optical resolution to scales on order of the localized state, we prepared hetero-nanobubbles on template stripped gold (TS-Au), which allows for optical resolutions on the order of the gap formed between the nano-optic probe and the substrate [125]. In addition, the quenching of photoluminescence of the monolayer and heterobilayer regions in contact with the substrate greatly reduces background, improving nanobubble's PL contrast [126]. Figure 4.6a shows an AFM image of a nanobubble $WSe_2/MoSe_2$ on TS-Au, that shows localized interlayer exciton emission (Fig. 4.6b) when compared with the flat heterostructure. The greater strength of the interlayer exciton emission on the nanobubble edge can be attributed to two factors. First, there is an enhancement from the strain of the nano-bubble itself, which shifts the absorption of both constituent layers to the red, allowing for greater absorption of the excitation photons. Second, recent work has shown that like their intra-layer cousins, the interlayer excitons transition dipole is primarily in the plane of the 2D layers[127]. As the nano-optical probe moves

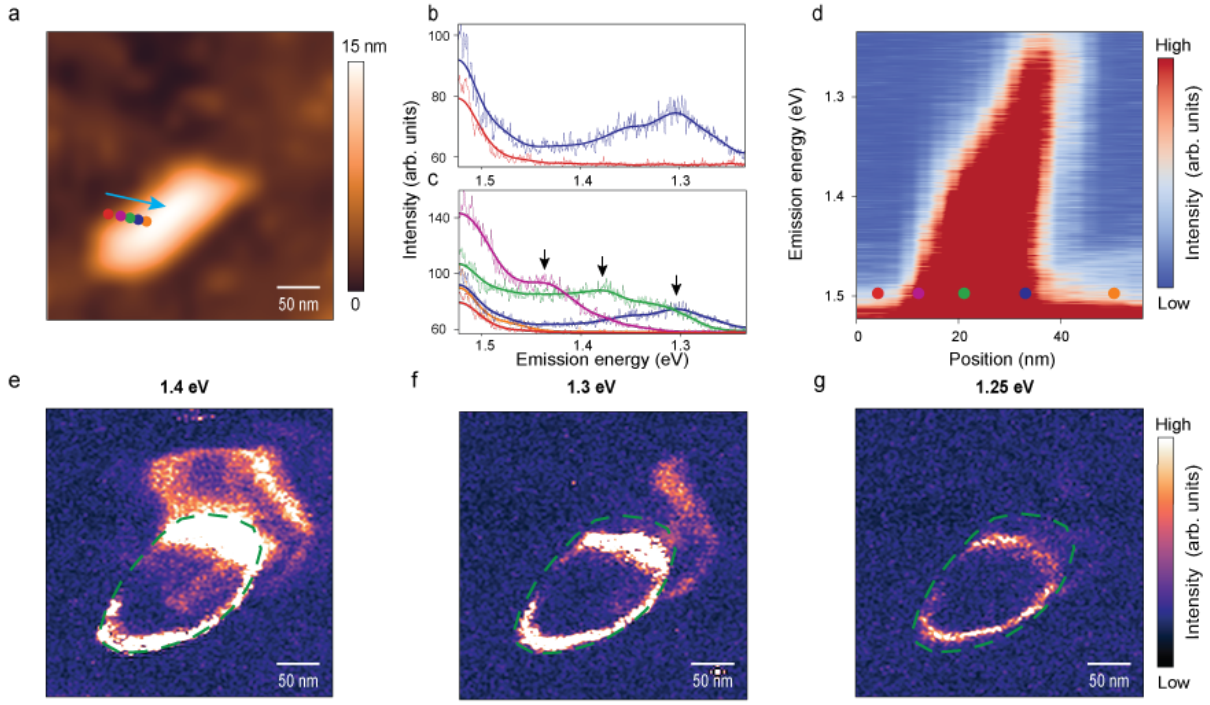

Figure 4.6: Hyperspectral nano-PL maps of localized interlayer exciton spectra **a** Atomic force micrograph of $MoSe_2$-WSe_2 nanobubbles on a template-stripped Au substrate. **b** Average nano-PL spectra on (blue) and off (red) the nanobubble region. **c** Nano-PL point spectra across the bubble edge corresponding the colored points in **a**. For points farther into the interior of the nanobubble, the emissions energy redshifts. **d** Hyperspectral heat map along the vector defined by points in (a). The redshifting of the emission is clearly seen, with the spectral weight shifting from above 1.5 eV at the very edge of the bubble (red point) to below 1.3 eV at 35 nm inside the bubble (blue point). Past the position past 40 nm (orange point) the intensity shift below the low energy detection cutoff of the EMCCD of ~1.2 eV. **e-g** nano-PL maps (average with a window sized 2.5 nm) binned different energy intervals, ordered by decreasing emission energy. The approximate physical nanobubble edge is shown with the green dashed line. The data clearly shows the redshifting of the emission on going into the bubble.

across the edge of the nanobubble, more of the transition dipole is aligned with the polarization of the nano-optical field, allowing for significantly greater in- and out-coupling for optical fields. This alignment we believe is critical for near-field observation of inter-layer exciton luminescence, which has substantially weaker oscillator strength. We also expect that strain-localized PL signal is enhanced by funneling effects, where excitons are preferentially shuttled towards the lower energy states[128, 129, 130]

Figure 4.6c shows point spectra at various locations across the nanobubble edges, identified by the colored markers in Fig. 4.6a and 4.6d. Black arrows show visual identification of the localized interlayer exciton peak. Clear red shifting of the emission is observed as one moves from the outer edge of the bubble into the interior. To visualize this more clearly, in Fig. 4.6c we plot a hyperspectral line-scan along the vector defined by colored points in Fig. 4.6a. The general trend is towards redder emission, shifting $\sim$ 200 meV over 15 nm into the bubble, after which the emission quickly falls to zero in the nanobubble interior. In Figs. 4.6e - 4.6g we show this same trend with spatial maps with energy bins of 1.40, 1.30, and 1.25 eV, respectively. The size of the localized interlayer exciton emission "ring" clearly shrinks for the redder energy bins.

The shifting of the localized interlayer exciton emission energy reflects the energic shift of the $MoSe_2$ conduction band observed in the STS. Indeed, comparing the STS and nano-PL hyperspectral line scans, the roll-off of the interlayer emission energy and the conduction band shows remarkable similarities at the nanobubble, but the nano-PL shows a sudden drop-off in emission intensity soon after the edge, which is not seen in STS. This drop-off however is expected due to the silicon detector used for the nano-PL spectroscopy (see methods for details), which rapidly loses quantum efficiency at energies lower than $\sim$1.3 eV. Similarly, we do not observe emission from the deeply localized defect states seen in Fig. 4.3 given that this would correspond to emission energies $\sim$0.7 eV, which is far below the cutoff our detector. While the quantitative comparison between the STM and nano-PL data is not possible due to the sample differences, evaluation of the STS-derived band gap and exciton PL energy provides information on the binding energy for excitons associated with the conduction band near the bubble edge. Our results are consistent with

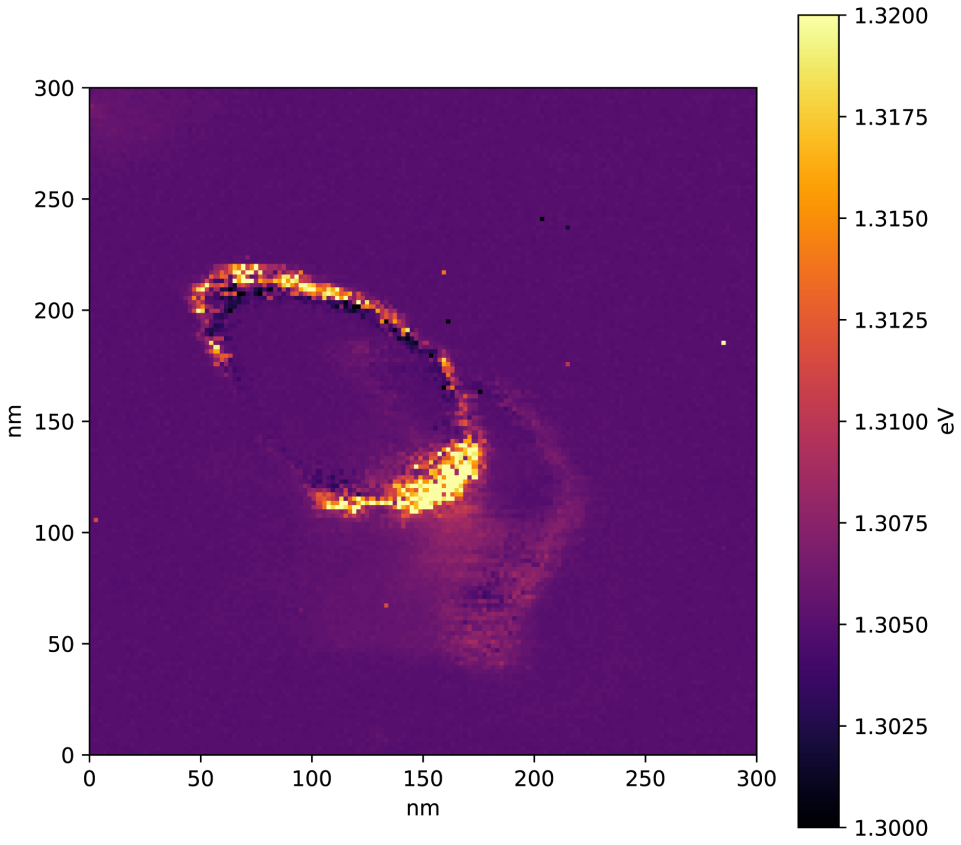

Figure 4.7: Spectral median of the interlayer exciton emission energy (825 nm to 1000 nm).

a conduction band interlayer exciton binding energy with the magnitude of a couple of hundred meV within the bubble[131].

Figure 4.7 shows the spectral median of the interlayer exciton (ILE) emission energy (825 nm to 1000 nm). This reflects the general trend of the emission spectrum, however, the shifts of the spectral median are smaller because of the contributions from higher energy emission which lowers the contrast between the different ILE energies. Around the ring of the nanobubble, there is a clear bright to dark (higher to lower energy) shift of the median, which follows the shifts imaged in STM of the $MoSe_2$ conduction band. The color bar unit is electron volts (eV). Figure 4.8 shows the spectroscopic maps of the interlayer exciton emission at 1.4, 1.3 and 1.25 eV on a different nanobubble. The localized states are clear at the border of the nanobubble. The ring size of localized interlayer exciton shifts by decreasing the energy, consistent with the observations shown in Fig. 4.5d-f. The redshifting of interlayer exciton emission indicates the conduction band edge shift in the heterobilayer.

4.6 Schrodinger-Poisson Simulations

To understand the contributions of doping and strain to the observed spectroscopic features in the experiment, we performed Schrodinger-Poisson (SP) simulations using the approach and code of Ref. [132]. The lengthscale associated with the entire bubble region is too large to model directly, but we will show that the pertinent experimental features can be captured with a significantly simplified model. Our focus on the conduction band of the heterostructure, which is derived from the $MoSe_2$ layer. Thus, we take the band parameters for $MoSe_2$ from Ref. [133] and electromechanical parameters from Ref. [134]. Since the important physics is localized to the bubble edge, we approximate the bubble region by a 2D inclusion in monolayer $MoSe_2$ (large enough to isolate the two interfaces required by periodic boundary conditions), with a the downward shift of the conduction band in the bubble the region, as well as a background doping, that both increase with strain [135]. The strain is assumed to be slightly larger at the edge of the bubble region. The DOS is calculated assuming a 2D parabolic dispersion in the direction parallel to the inclusion above the conduction-band minimum and below the valence band maximum.

Figure 4.9a shows the band diagram obtained by self-consistent solution of the SP equations,

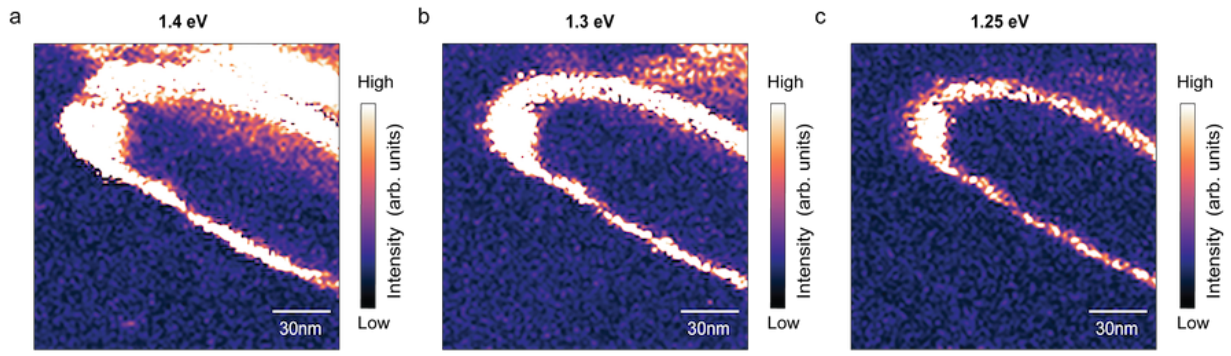

Figure 4.8: Spectroscopic map of the interlayer exciton emission at **a** 1.4,**b** 1.3 and **c** 1.25 eV showing redshifting due to the conduction band edge shift.

focusing on the CB. By construction, the Fermi level is at the conduction band within the bubble region due to the background doping. The dips in the electrostatic potential of the conduction band at the edges of the "bubble" have two origins. The first is the band bending induced by the interface between the doped and undoped regions. The second is that we assume a higher strain at the interface, which increases the effect of this band bending. We found that adding a piezoelectric polarization charge at the interface (not shown) did not change the qualitative features, other than introducing an asymmetry in the band-bending on the opposite sides of the bubble region.

The red dot-dashed lines in Fig. 4.9a are the energies of the bound states in the bubble region, and the green dotted lines are their squared wavefunctions (shifted so that the zero-density level is at the energy for clarity). We can see that the band bending at the interface region results in a bound state, which can also be clearly seen in Fig. 4.9b as spikes in the electron density at the edge of the bubble regions. In Fig. 4.9c we plot the DOS of the total system, including the sum of 1D states in the bubble region, and the 2D DOS in the bulk, at different x points near the interface of the bubble (see the inset, denoted by curve color). Superimposed on the step-like increase from the 2D DOS at the conduction and valence band edges in the bubble, we can see a small enhancement in the DOS near the interface, where the localized state resides. As we move toward the center of the bubble region, this enhancement weakens, and ultimately disappears. We focused our model on the $MoSe_2$ layer of the bilayer structure since the $MoSe_2$ is the main contributor to the conduction band. The size of the bubble is much larger than the crystal cell. If you were to zoom in at the

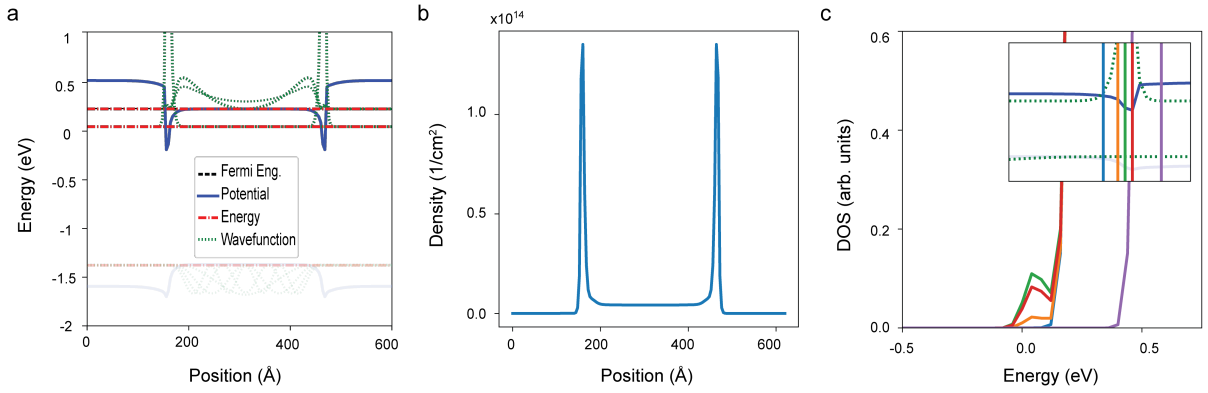

Figure 4.9: Schrodinger-Poisson (SP) simulations **a** Band diagram for two-dimensional Schrodinger-Poisson (SP) model of the bubble. Blue solid lines are the self-consistent band potentials, red dot-dashed lines are the energies of some of the confined states, black dashed line is the Fermi level, and green dotted lines are the confined wavefunctions. **b** Self-consistent electron density versus x position in (a). **c** Density of states versus energy including the 1D states confined to the well, with 2D DOS outside of the bubble, and in the bubble interior, superimposed.

atomic level the edge of the bubble can be approximated by its tangent on the surface of the $MoSe_2$ layer. Hence using the deformation gradients as a baseline for the energy of the different strained portions we can accurately model the band edge with the one- dimensional model. Our theoretical results, though the result of a simplified model, accurately captures the essential features of the experimental observations. They indicate that sharp lateral junctions in doping are an excellent way to engineer localized states in 2D TMD semiconductors. Such localized states do not depend on the presence of specific chemical defects or specialized strain fields. Recently, several 2D materials interfaces have shown the ability to realize large charge transfer at the interface [136, 137]. Our results indicate that such interfacial engineering together with nanostructuring can be employed to create optical emitters with arbitrarily desired shapes at the nanoscale. Our work provides a clear route to achieving this in the future.

references.bib

4.7 Theoretical Methods

The induced strain in the bubble causes the conduction band energy to drop allowing it to cross the Fermi level of the material in that local region for a small number of energy levels. We have

concluded this by running Density Functional Perturbation simulations of $MoSe_2$ in a bulk set by calculating the first order response to strain [138]. The crossing of the fermi level only allows a small region near the Q point (halfway between Gamma and K symmetric points) in the Brillouin zone to have electrons in the conduction band leading to a one-dimensional density of states in the bubble region. This region is then flooded with electrons. Since the bubble region is rather big, we utilize the 1-dimensional simulation of the Schrodinger-Poisson method [132] on the valence and conduction bands to simulate the combined effect of the strain and the induced doping.

As discussed in the main text, Schrodinger-Poisson (SP) simulations were performed using the approach and code of Ref. [138]. Our simple model of the bubble region involved five regions in the direction perpendicular to the bubble interface [see Fig. 4.9(a)]. Region 1 was 150 nm wide and intended to be bulk-like, with parameters from unstrained $MoSe_2$; region 2 was a narrow, high-strain region at the interface 5 nm wide with the largest conduction band deformation and doping; region 3 was a wider region with slightly less doping and slightly less strained/doped and was intended to model the internal region of the bubble; region 4 was the same as region 2; region 5 was the same as region 1. The parameters for the regions are given in the tables below.

Table 4.1: Slab Table

Parameters	**Slab 1**	**Slab 2**	**Slab 3**	**Slab 4**	**Slab 5**
Strain %	0	0	1	0.9	1
Width (nm)	150	150	5	300	5

Table 4.2: Input parameters for strains

	Region 1,5	Region 2,4	Region 3
Relative permittivity	15.71	15.71	15.71
Polarization charge (e/u.c.^{2})	0.0	0.0	0.0
Electron doping (e/u.c.^{2})	0.0	0.45	0.5
Vacuum level (eV)	3.5	3.5	3.5
Valence band energy (eV)	-1.5	-1.5	-1.5
Conduction band energy (eV)	0.0	0.6	0.54
VB m^* (perp. to interface)	0.59	0.59	0.59
CB m^* (perp. to interface)	0.54	0.54	0.54
VB m^* (parallel to interface)	0.59	0.59	0.59
CB m^* (parallel to interface)	1.08	1.08	1.08

Chapter 5: Large Electrically tunable Band Gap in Semiconducting Heterobilayers

In previous chapters, we showed moiré potential as well as doping and strain as effective methods to achieve localized states to confine carriers. Here, we utilize electric fields for continuous band gap change in twisted WSe_2/WS_2 heterobilayer. Band gap tunability in TMD semiconductors is crucial for many optoelectronic applications including quantum emitters. Here we report a comprehensive study of monotonic band gap reduction of twisted WSe_2/WS_2 heterobilayer using an electrostatic gate. Our approach is utilizing scanning tunneling microscopy and spectroscopy to probe the band properties of the TMD heterobilayer with high energy resolution. We achieve continuous band gap tuning up to $\sim$ 400 meV by applying a perpendicular electric field. Our results can be captured well using tip-enhanced electric field model in 2D semiconducting physics. Furthermore, our DFT calculations show highly populated densities in each layer, evidence for Coulomb-driven bandgap change. Our work opens a new route toward highly tunable semiconductors for quantum technologies and future optical studies in quantum emitters.

5.1 Introduction

Transition metal dichalcogenide semiconductors possess an intrinsic band gap, a fundamental property crucial for carrier confinement used in numerous photonic and electronic devices[139, 102, 104, 106, 140]. The bandgap in 3D bulk semiconductors remains untunable and can be determined using various techniques such as optics and scanning tunneling microscopy (STM)[141, 142, 143, 74]. However, the band gap in 2D semiconductors is tunable and susceptible to the number of layers[144, 141, 142, 15, 28, 143], doping[113, 112, 96, 111, 145], environmental screening[114], and strain fields[146, 74, 105]. Among these methods, electrostatic gating is an

experimentally advantageous method due to its ability to provide continuous tunability, higher doping level, and great integration capability to nanoelectronic devices[147, 148]. The doping applied by the electrostatic gate significantly influences the bandgap in the 2D limit due to reduced screening. Furthermore, the induced electric field is expected to have a stronger effect on the band gap of type II heterobilayers, where the valence band and conduction bands originate from different layers. So far the studies on gate tunable TMD heterobilayers has relied primarily on optical techniques to investigate excitonic properties. However, these methods are inadequate for determining the electronic band gap. It is also challenging to detect the band gap change in optical absorption due to the 2D limit and the background dominance. In addition, the optical techniques are diffraction limited to observe the electric effect in nano scale, however, sub-wavelength patterns can be used to strongly confine the field and tune the bandgap[149]. Other methods such as angle-resolved photoemission spectroscopy (ARPES) have been utilized, but challenges remain in detecting both valence and conduction bands to determine the electronic band gap. To address these limitations, we employ scanning tunneling microscopy (STM) and spectroscopy (STS) to investigate the properties of twisted WSe_2/WS_2 heterobilayers in the presence of a back gate. STM/STS offer high energy and spatial resolution, necessary components to extract the band gap from both valence and conduction band edges across the TMD surface. This technique allows us to gain insight on the individual contribution of electric field and doping effect in band tuning. However, STM measurements are usually performed on chemical vapor deposition (CVD) materials and metal substrates and gating these devices is not feasible. Here we use a silicon back gate to create electric field on a twisted WSe_2/WSe_2 heterobilayer. To overcome the contact issue with TMDs, the twisted heterobilayer is lying on graphene and the measurements were conducted at room temperature.

5.2 Twisted WSe2/WS2 Heterobilayer

We study a device consisting of WS_2, WSe_2, graphene, and h-BN lying on a Si/SiO2 substrate as a back gate. The stack was made using a dry transfer technique from mechanically exfoliated crystals. We first picked up the h-BN flake with ~40nm thickness using poly-dimethylsiloxane

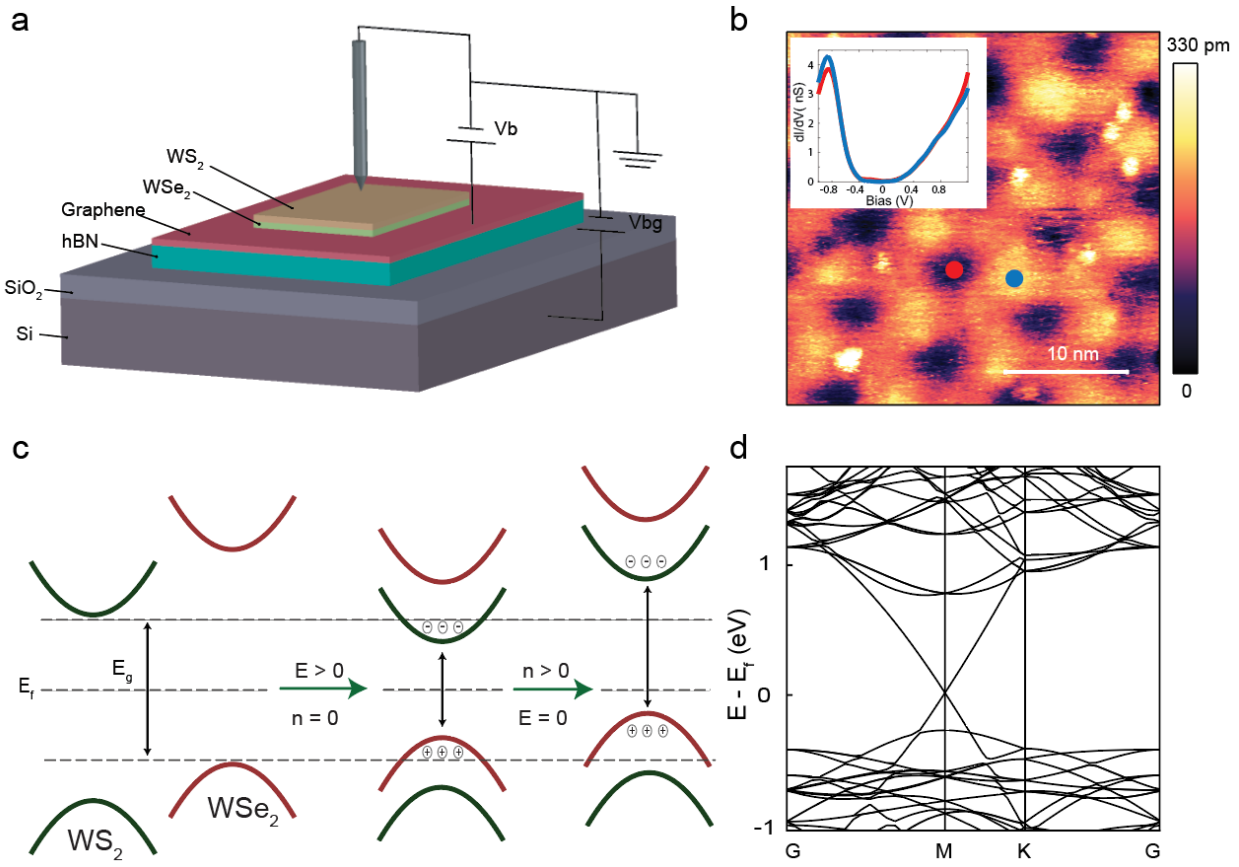

Figure 5.1: Twisted WSe_2/WS_2 heterobilayer **a** Schematic of twisted WSe_2 and WS_2 device geometry measured by scanning tunneling microscopy(STM). The heterobilayer is placed on graphene and a few layers of h-BN and the back gate is applied through Si/SiO2. **b** STM topographic image of nearly aligned WSe_2/WS_2 showing ~8 nm moiré pattern. The inset represents the spectra on different moiré configurations corresponding to blue and red dots on the topography. The spectra show no major difference at the band edges for different moiré sites. **c** Schematic illustration of band structure in WSe_2/WS_2 heterobilayer in the presence of electrid field(E) and doping(n). The electric field reduces the band gap whereas doping shifts the Fermi level relative to the band edges. **d** Electronic band structure of WSe_2/WS_2/graphene in the absence of electric field by DFT.

(PDMS) stamp coated by a thin layer of polypropylene carbonate (PPC). Then the graphene layer was lifted by the h-BN layer. On a rotation stage, monolayer WSe_2 and WS_2 were picked up subsequently using h-BN graphene stack on PPC. The twist angle between TMD monolayers was aimed at zero. We deployed second harmonic generation measurements to extract the rotational alignment between two TMD monolayers prior to stacking. The stack on PPC was "flipped" on (285 nm) Si/SiO2 substrate. We annealed the device at 200 degrees for 30 minutes to remove the ppc layer underneath the stack. Lastly, an indium alloy was made to the graphene layer for STM electrical contact. By aligning the WSe_2 and WS_2 monolayers rotationally using the SHG results, a moiré pattern with a periodicity of approximately 8nm was produced. We employed scanning tunneling microscopy (STM) and spectroscopy (STS) as ideal probes to investigate TMD surface structure and band properties. Figure 5.1a depicts a schematic of the device geometry and the experimental setup. The STM bias and back gate were applied to the graphene and SiO2 substrate, respectively, while the STM tip was grounded. This device geometry enabled us to access the valence band of WSe_2 and the conduction band of WS_2 which are expected to be significantly influenced by the electric field due to the type II band alignment of the heterobilayer. A typical STM topography of the heterobilayer surface is presented in Figure 5.1b. The $\sim$ 8nm periodic moiré superlattice is visible in the topographic image. The large lattice mismatch between WSe_2 and WS_2 (about 3 percent) leads to the formation of a highly uniform moiré superlattice. Three moiré stacking configurations are present in this system, namely, AA (where the metal atoms of both layers are vertically aligned), AB (where the metal of one layer is positioned on top of the chalcogenide of the other layer), and BA (where the chalcogenide of one layer is positioned on top of the metal of the other layer). The STM tip was calibrated on Au(111) single crystal. The lock-in used for dI/dV measurements was set at 25 meV modulations with a frequency of 721 Hz. All the STM and STS measurements presented in this work were conducted at room temperature. To characterize the electronic properties of the heterobilayer, we performed dI/dV measurements on AA and AB sites corresponding to the blue and red dots on the topographic image in the absence of back gate voltage (Fig. 5.1b inset). The spectra on different moiré sites indicate the band edges

of the heterobilayer remain the same and independent of the moiré configurations. This reflects the weak periodic potential created by the moiré pattern, as opposed to the other TMD heterobilayers such as $WSe_2/MoSe_2$[89]. To differentiate the distinctive effect of electric field and doping on the band structure, a schematic of the band alignment in WSe_2 and WS_2 heterostructure is illustrated in Figure 5.1c. The valence band and conduction band of the heterobilayer originate from WSe_2 and WS_2 respectively. In the absence of both the electric field and doping, the Fermi level lies in the middle of the gap. Once an electric field is applied, both valence and conduction bands are displaced towards the Fermi level leading to a bandgap change. Depending on the direction of the electric field, the band gap can increase or reduce in size, nonetheless, the Fermi level position remains unchanged. As opposed to the electric field effect, doping causes a shift in the Fermi level position relative to the band edges, while the bandgap remains unchanged.

To gain a more accurate insight into the band properties of WSe_2/WS_2/graphene, we calculated the band structure in the reciprocal space using density functional theory (DFT) as shown in Figure 5.1d. At zero electric field and doping, the charge neutrality point of graphene is located at Fermi energy and the WSe_2/WS_2 bilayer exhibits a band gap of 1.01 eV.

5.3 Gate-Dependent Spectroscopic Measurements

To elucidate the dependence of band properties in the presence of back gate, we conducted a series of dI/dV measurements on the heterobilayer. Fig. 5.2a shows the local density of states (LDOS) of WSe_2/WS_2 bilayer as a function of back gate voltage and tip bias. The overlaid dashed red lines over the map indicate the valence and conduction band edges of the bilayer and the dark region corresponding to low LDOS defines the semiconducting gap. The map clearly demonstrates that that the band gap decreases monotonically from negative to positive back gate voltage. To provide further insights into the evolution of the band gap, a few dI/dV spectra at various back gate voltages are plotted in Figure 5.2b. By sweeping the back gate voltage from -70 V to +70 V, both the valence and conduction band edges are shifted towards the Fermi energy, resulting in a significant reduction in the band gap. In order to quantify the doping level and band gap

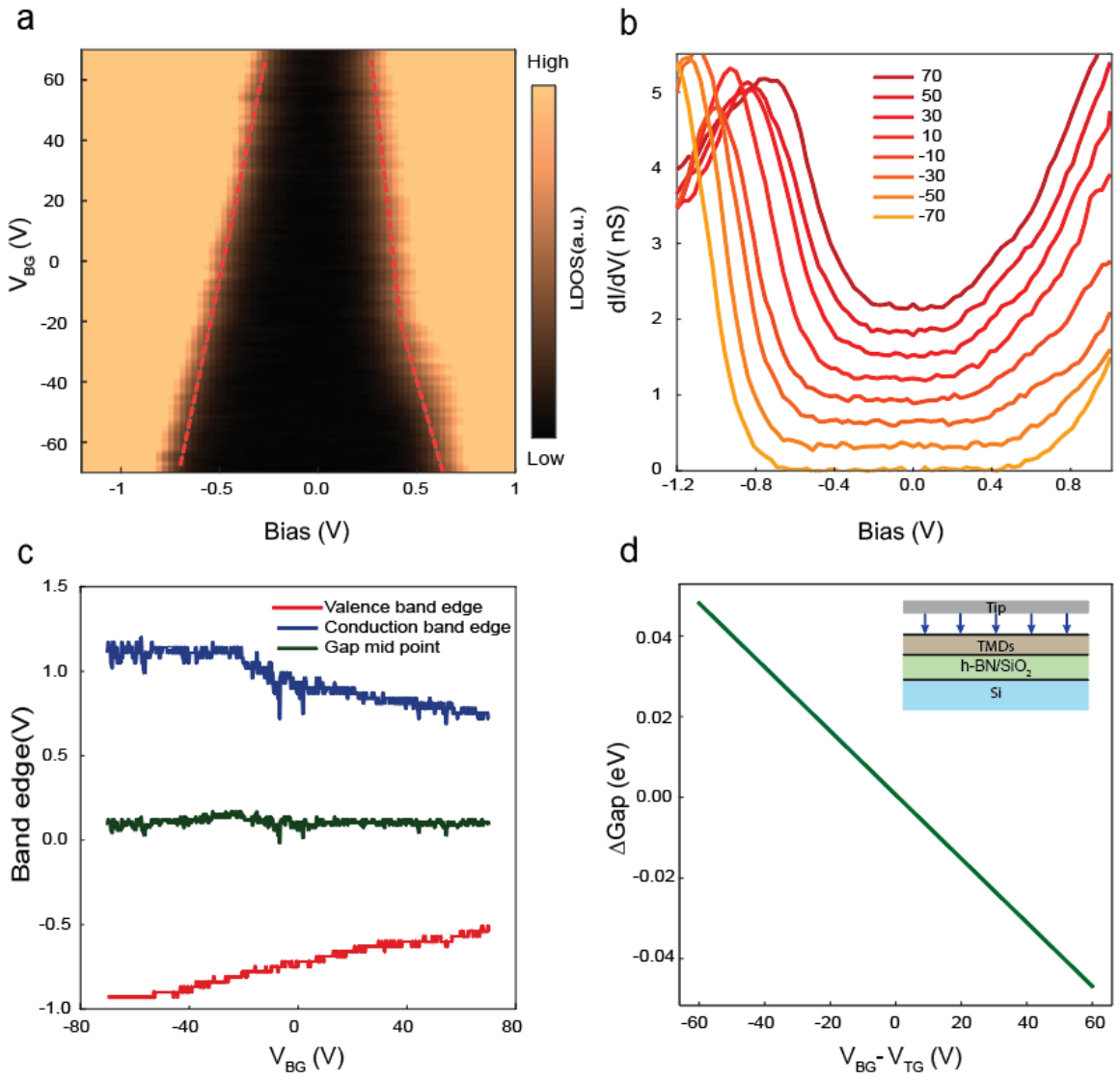

Figure 5.2: Gate-dependent spectroscopic measurements of WSe_2/WS_2 heterobilayer **a** Gate-dependent dI/dV point spectroscopy. The red dashed line is superimposed on the map to indicate the valence and conduction band edges change as a function of the back gate. **b** The dI/dV point spectra at various back gate voltages with a vertical offset. It shows a dramatic band gap decrease from V_{BG} = -70V to +70V. **c** Valence, conduction band edges, and Fermi level positions corresponding to fig 2a are plotted as a function of Gate Voltage. Both valence and conduction band edges shift significantly, in contrast to the Fermi level remaining almost unchanged. **d** Band gap change of WSe_2 and WS_2 extracted by a simple 2D semiconductor model, parallel plate capacitance model, is plotted as a function of back gate voltage. The change is limited to ~ 40 meV using this simplified model.

energy, we plot the valence band, conduction band, and gap mid point positions in Fig. 5.2c. The valence and conduction edges are defined by setting a threshold on the dI/dV spectra at the positive and negative energies. Figure 5.2c clearly exhibits a non-linear substantial change in both valence and conduction band edge positions by applying the back gate. Whereas the gap mid point remains nearly the same showing the overall doping of the heterobilayer is negligible. This result shows the presence of a large electric field in space created by the back gate. To understand the experimental observations, we first calculate the extrinsic and intrinsic doping using conventional 2D semiconducting physics. In this model, we consider the device as three layers of simple parallel plate capacitor (inset of Fig. 5.2d) including the STM tip, a chunk of WSe_2/WS_2 heterobilayer, and a chunk of h-BN/Si/SiO2 to extract the extrinsic carrier density and the corresponding band gap. To achieve this, we compute the chemical potential of each layer numerically, which allows us to calculate the carrier densities of the TMD layers. Subsequently, we extracted the heterobilayer band gap from the carrier densities. Further information on the model is available in the following section.

The calculated intrinsic carriers at room temperature are 0.95 and 2.4×10^{-5} $/cm^{-2}$ corresponding to WS_2 (top layer) and WSe_2 (bottom layer). This result indicates that the small intrinsic densities have a negligible impact on the band gap. To investigate the effect of extrinsic charge on the band gap, we calculated the extrinsic carrier density caused by the tip and back gate voltages. The band gap change is then extracted from the extrinsic carrier density and is plotted as a function of $V_{BG} - V_{TG}$ in Figure 5.2d. This plot shows that increasing the back gate voltage results in a reduction of band gap consistent with the experimental observation. Nonetheless, the calculated band gap varies up to $\sim$ 45 meV at $V_{BG} - V_{TG} = +60V$, one order of magnitude smaller than the STM results. It is important to note that the model we have presented here is a simplified representation of the actual experimental setup, however, we can make further modifications to the model to closely emulate the STM setup.

5.4 2D Semiconducting Model

5.4.1 Parallel Plate Model

In this section we shall treat our device as a simple parallel-plate capacitor formed between the STM-tip (V_{TG}) and the back-gate (V_{BG}). In between the parallel plates there are three slabs of dielectrics with thickness d_1, d_2, d_3 and dielectric constants ϵ_1, ϵ_2, ϵ_3, corresponding to air (between the tip and the sample), the $MoSe_2/WSe_2$ heterobilayer, and BN/SiO_2 (above the Si back-gate). For clarity in the following discussion, we label the three dielectric regions with I, II, III from top to bottom.

Our goal is to solve for the electric potentials at the two boundaries. The electrostatic boundary conditions give:

$$\epsilon_1 E_1 - \epsilon_2 E_2 = \sigma_t \tag{5.1}$$

$$\epsilon_2 E_2 - \epsilon_3 E_3 = \sigma_b \tag{5.2}$$

where E_1, E_2, E_3 are the vertical components of the electric field in the three slabs, and σ_t, σ_b are the free charge densities on the boundaries. Writing the electric potentials at the I-II and II-III boundary as V_t and V_b, one can easily express the fields in terms of the potentials:

$$E_1 d_1 = V_{\mathrm{TG}} - V_t \tag{5.3}$$

$$E_2 d_2 = V_t - V_b \tag{5.4}$$

$$E_3 d_3 = V_b - V_{\mathrm{BG}} \tag{5.5}$$

Assuming the free charges entirely come from the shift of the electrostatic potentials in the two TMD semiconductor layers and the chemical potentials are away from the band edges (compared to $k_B T$), the free charge density can be written as

$$\sigma = 2en^{\mathrm{in}} \sinh(eV/k_B T) \tag{5.6}$$

where n^{in} is the intrinsic carrier density of a TMD monolayer. The intrinsic density can be estimated from the semiconductor law of action:

$$n^{\text{in}} = \frac{\sqrt{m_c^* m_v^*}}{\pi\hbar^2} k_B T \exp(-\Delta/2k_B T) \tag{5.7}$$

with m_c^*, m_v^* being the effective masses of the conduction and valence bands, and Δ the monolayer band gap. The above set of equations can be simplifed down to two:

$$\frac{\epsilon_1}{d_1}(V_{\text{TG}} - V_t) - \frac{\epsilon_2}{d_2}(V_t - V_b) = 2en_t^{\text{in}} \sinh(eV_t/k_B T) \tag{5.8}$$

$$\frac{\epsilon_2}{d_2}(V_t - V_b) - \frac{\epsilon_3}{d_3}(V_b - V_{\text{BG}}) = 2en_b^{\text{in}} \sinh(eV_b/k_B T) \tag{5.9}$$

Here V_t and V_b can be solved numerically and their difference gives an semiconductor estimation on the band gap change, which is roughly 10 times smaller than our experimental observation.

5.4.2 Tip Enhancement Model

Since a sharp tip can potentially lead to a local field enhancement and thus have an impact on the electrochemical potentials, in this section we shall discuss how the potentials react to the tip size using a simple spherical conductor model.

We treat our STM tip as a spherical conductor of radius R, which is held at potential $V_{\text{TG}} - V_{\text{BG}}$. We further assume the charges on the sphere are uniformly distributed and will not be affected by its surroundings. The problem can then be transformed into finding the electric potential distribution of a point charge ($q = R(V_{\text{TG}} - V_{\text{BG}})$, $z_0 = a + d + R$) in three slabs of dielectrics, with the middle slab (which corresponds to the TMD heterobilayer) having a finite thickness of $2a$ while the top and bottom slabs extending to infinity.

This boundary-value problem has been solved analytically using image charge techniques with Fourier transforms. The potentials at the boundaries (i.e., $z = \pm a$) right below the point charge are

(in Gaussian units):

$$V_t = \frac{2q}{\epsilon_1 + \epsilon_2} \int_0^\infty dk \, \frac{e^{k(a-z_0)} - L_{32} e^{-k(3a+z_0)}}{1 - L_{12} L_{32} e^{-4ka}} \tag{5.10}$$

$$V_b = \frac{4\epsilon_2 q}{(\epsilon_1 + \epsilon_2)(\epsilon_3 + \epsilon_2)} \int_0^\infty dk \, \frac{e^{-k(a+z_0)}}{1 - L_{12} L_{32} e^{-4ka}} \tag{5.11}$$

where $L_{ij} \equiv (\epsilon_i - \epsilon_j)/(\epsilon_i + \epsilon_j)$. Enhancements indeed show up for small tip radius, and with larger radius the result is leaning toward the parallel capacitor model as expected.

5.5 Results of Tip-Enhanced Electric Field Model

To address this issue, we modify the model by taking into account a finite tip geometry instead of simple two-infinite parallel capacitor geometry. This consideration leads to a significant enhancement of the electric field induced by the STM tip and results in significant effects on the band properties. It is worth noting that experimentally the STM tip can have a rounded shape due to its preparation on an Au(111) substrate, which contains grids of a few nanometer sizes, making it reasonable to consider the tip as being shaped similar to the grids when performing IZ measurements and crashing on the surface. The model under consideration assumes a spherical tip with a radius R situated in a vacuum at the top of the TMD layers (shown in fig. 5.3a).

We further assume TMDs and h-BN/Si are two insulating layers with dielectric constants of $7.5\epsilon_0$ and $4\epsilon_0$, respectively. This assumption is supported by STM data as the Fermi level remains within the TMD gap under the electric field implying the insulating-like behavior of TMDs. The electric potential distribution in space is analytically derived using image charge techniques with Fourier transform. Our calculations reveal that the electric field magnitude significantly enhances by reducing the tip radius, as shown in Figure 5.3b. We can obtain one order of magnitude larger fields from a 10 nm tip size relative to parallel plate geometry. Achieving high electric fields is crucial to investigate high carrier density-driven phenomena in TMDs such as exciton condensation by optical studies. However, it is technically challenging to obtain enhanced fields due to poor back gate dielectrics leading to dielectric breakdown and current leakage. This plot highlights the possi-

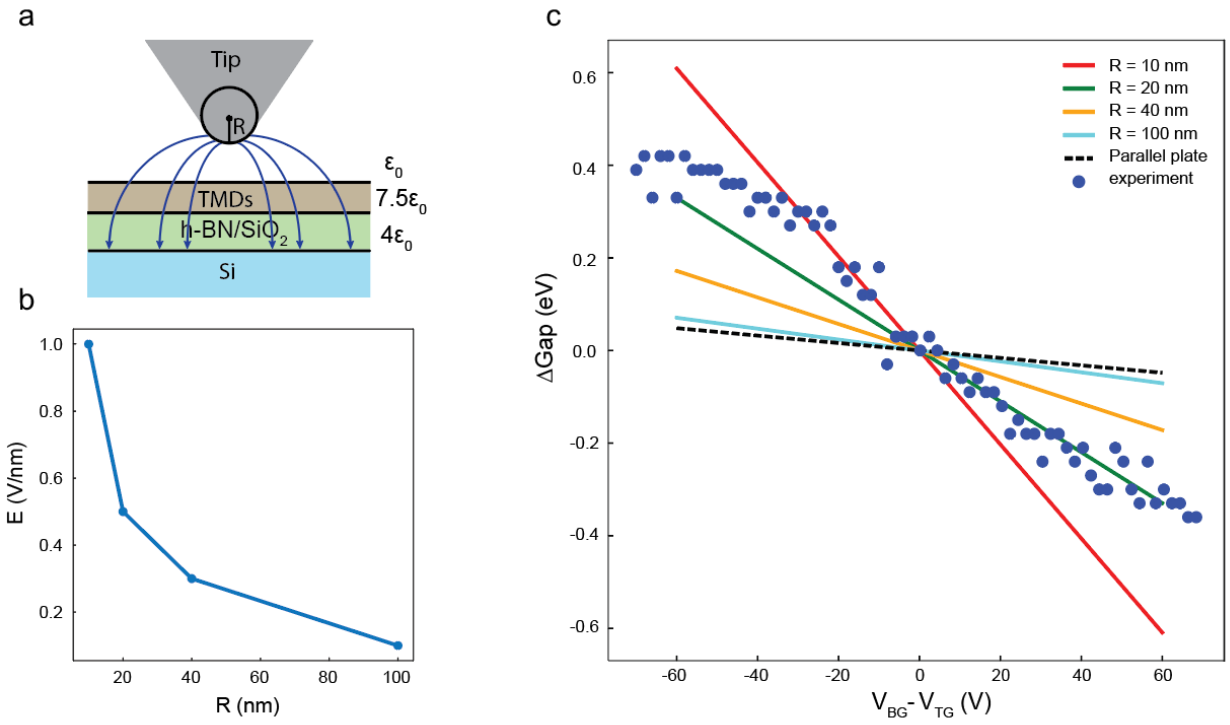

Figure 5.3: Tip-enhanced electric field on WSe_2/WS_2 heterobilayer **a** Schematic of the modified model; the STM tip geometry is approximated as a sphere with a radius R. In this model, TMD layers and h-BN/ Si/SiO2 are considered as two insulating layers with $7.5\epsilon_0$ and $4\epsilon_0$ dielectric constants, respectively. **b** The electric field enhancement as a function of tip radius calculated by the semiconducting model shows the exponential growth of the electric field by tip radius reduction. **c** The band gap change is plotted for various radii as a function of the Back gate calculated by the semiconducting model described in the text. The experimental data are plotted with blue dots and lie within red and green curves corresponding to R = 10nm and 20nm at high back gate voltage.

bility of achieving high electric fields in the experimental setups, in specific optical spectroscopy, by selecting the proper tip radius and unlocking new properties of the materials. Using the electric field distribution in space, we can calculate the band gap as a function of a perpendicular electric field. Figure 5.3(c) shows the band gap change from the parallel-plate capacitor model (dashed line), the spherical tip model at various radii (solid lines), and the experimental data points (blue circles). In this model, the band gap increases at the negative back gate and shrinks at the positive back gate in agreement with the experimental results. Furthermore, the band gap change at a fixed $V_{BG} - V_{TG}$ is substantially increased as the tip radius decreases due to the enhanced electric field shown in Fig. 5.3b. The STM data set (blue dots) lies between R = 20 nm (green line) and R = 10 nm (red line). As discussed, $\sim$ 10 nm tip radius is experimentally reasonable due to the method used to prepare the tip on gold and the size of the grain boundaries. Both experimental data and our tip-enhanced capacitor model provide evidence of significant band gap change in the presence of a perpendicular electric field.

5.6 DFT Calculations

Despite the fact that the tip-enhanced electric field model presented here captures the large band gap tuning compatible with experimental observations, it is still an incomplete picture of the actual experiment as graphene layer is not taken into account throughout the calculations. Also, the assumption of insulating layers of TMDs used in the model is not fully accurate due to the relatively small band gap. In order to address this issue and understand the band structure, we performed density functional theory (DFT) calculations on the WS_2/WSe_2/graphene system. Figures 4 a and b display the band structure evolution of the heterostructure, under perpendicular electric fields. At zero field, the bilayer exhibits a band gap of 1.01 eV (fig. 5.1b). At an electric field of E = -0.2 V/Å, the band gap of the WS_2/WSe_2 bilayer increases to 1.12 eV (Figure 5.4b) while E = 0.2 V/Å introduces the reduction of bands gap (0.90 eV) as shown in fig. 5.4d. According to the projected density of states shown in figures 5.3c and 5.3e, the valence band maximum at K is derived from the WSe_2 layer, while the conduction band minimum is assigned to the WS_2 layer,

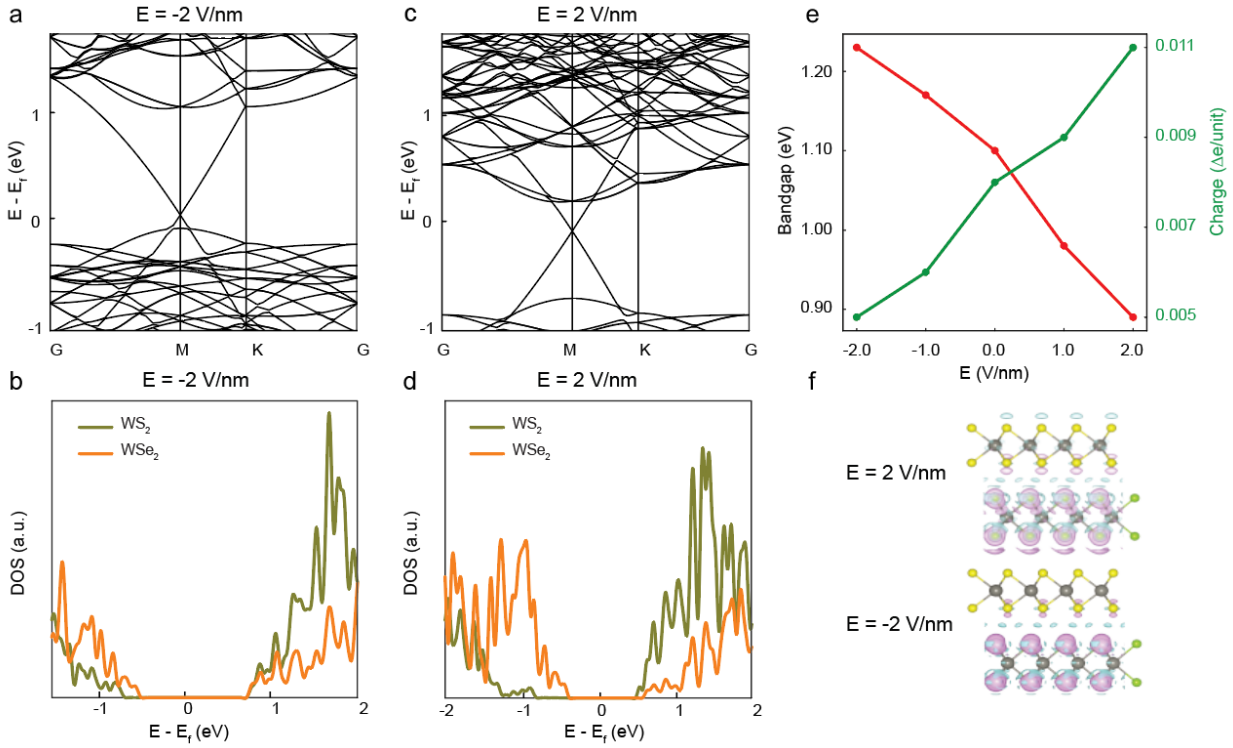

Figure 5.4: DFT calculations on WS_2/WSe_2/graphene **a-b** Band structures in the reciprocal space for different vertical electric fields, -2V/nm and +2 V/nm showing a substantial shift in band edges in the presence of electric field. **c-d** Corresponding projected density of states on WS_2 (green) and WSe_2 (orange). Fermi levels are set to zero in all panels. **e** Calculated band gap and charge per unit cell on WSe_2 by DFT as a function of Electric field induced by the back gate. The band gap decreases by 300 meV from -1V/nm to +1V/nm. The charge (green curve) is calculated by Bader analysis and shows an increase of carrier density as a function of electric field. **f** Electric field dependence of charge distributions of the WS_2/WSe_2 heterostructure. Spatial difference of electronic states in WS_2/WSe_2 heterostructure for -0.2 V/Å and 0.2 V/Å. The pink and cyan surfaces indicate charge accumulation and depletion after the formation of the heterostructure, respectively. The grey, yellow and green balls represent W, S and Se atoms, respectively.

resulting in a type II band alignment. The field-induced changes lead to apparent band offset variations in both layers. Owing to type II band alignment, each layer band offset gives rise to band gap change rather than overall doping. Figure 5.4c and 5.4d clearly show a shift in both WSe_2 and WS_2 bands from E = -2 V/Å to E = 2 V/Å resulting in band gap increase and reduction, respectively. The field dependence of band gaps is in agreement with the experimental observations. To quantify this change by DFT, the band gap energy is plotted as a function of the electric field in fig. 5.4e showing up to 200 meV gap change relative to zero electric field at 2 V/Å. This is almost half the change observed by the STM measurements. To identify the root cause of this mismatch, we calculate charge per unit cell on WSe_2 (green curve) based on Bader analysis as a function of electric field (shown in fig. 5.4e). The lattice constant in the simulation is 3.19 Angstrom. Using this analysis, we estimate achieving the carrier density as high as $\sim 10^{13}/cm^2$ at a large enough electric field (2 V/nm). This is one order of magnitude larger than accessible doping on TMDs used by conventional methods such as lithographic back gate limited to $10^{12}/cm^2$. In such a high carrier density the electrostatic interactions are expected to be significant enough to trigger collective interactions and influence the quasiparticle bandgap. 2D semiconducting TMDs are excellent candidates to study collective behaviors due to strong Coulomb interactions caused by low dimensional effects and weaker dielectric screening.[150, 151]. As a consequence of this many-body interaction, the bandgap energy can be renormalized dramatically[152, 28, 148]. This behavior depends strongly on the high density of carriers and the screening strength in the graphene layer. Our DFT calculation of $\sim 10^{13}/cm^2$ as the carrier density raise the possibility of such interactions and the associated effect on the band gap renormalization. To visualize the charge difference in the heterostructure, the isosurfaces at different electric fields are shown in Fig. 5.4f. The charge difference is defined as $\rho = +(-)$, the total charge densities of WS_2, WSe_2, respectively. It is obvious that the perpendicular electric fields induce significant modulations in the real-space charge distribution. At zero electric field, the charge distribution shows a sizable charge modulation within the two layers and clear hybridization at the interface of the two TMD layers. As E = 0.2 V/Å, the charge difference increases to a larger portion which mainly resides at the interfaces (Figure 5.4f) while the modi-

fication from the opposite electric field is relatively smaller. Our results of charge distribution as well as high carrier density provide evidence of large Coulomb interactions between two layers and the possibility of band renormalization. In the following we present the details of DFT method implemented in this work. All calculations were performed within the Vienna ab-initio Simulation Package (VASP)[153] using a projector-augmented wave (PAW) pseudopotential [154] in conjunction with the Perdew–Burke–Ernzerhof (PBE) [155] functional and plane-wave basis set with an energy cutoff of 400 eV. For WSe_2/WS_2 heterostructures, the unit cell with a lattice constant of 3.19 Å is used and the Brillouin zone is sampled by a 15×15×1 Monkhorst–Pack k-mesh. For graphene/WSe_2/WS_2 heterostructures, the model is chosen to consist a 4×4 WSe_2/WS_2 supercell and a 5×5 graphene supercell resulting in a small interlayer mismatch of lt;sampled by a 3×3×1 Monkhorst–Pack k-mesh. In all cases, a vacuum region of ∼15 Å was applied to avoid artificial interaction between the periodic images along the z direction. Because of the absence of strong chemical bonding between layers, van der Waals density functional in the opt88 form [156] was employed for structural optimization. All structures were fully relaxed until the force on each atom was less than 0.01 eV/Å. In conclusion, our findings show highly tunable band gap in WSe_2/WS_2 heterostructures using an electrostatic gate. As a result of high electric field applied by the back gate and STM tip, the band gap changes up to ∼ 400 meV. We introduced a tip enhanced electric field model to capture the experimental data and understand the underlying mechanism. Our results provide new opportunities in quantum emitters host by TMD heterobilayers.

Chapter 6: Nanometer-Scale Lateral p–n Junctions in Graphene/α-$RuCl_3$

In addition to investigating carrier confinement in TMD heterobilayers, this thesis also delves into the study of charge transfer-induced phenomena in α-$RuCl_3$ heterointerfaces. α-$RuCl_3$ relatively high work function (6.1 eV) compared to other 2D materials makes it a great candidate for studying interface physics. Specifically, the focus of this chapter is on the graphene/α-$RuCl_3$ heterostructure. The work function difference between the two layers results in a significant exchange of charges, leading to heavily p-doped graphene and n-doped α-$RuCl_3$. The nanobubbles present in the heterostructure provide an ideal testing ground to study lateral p-n junctions. To gain a comprehensive understanding of the electronic and optical responses of nanobubble p-n junctions, we employed a multi-pronged experimental approach that combined scanning tunneling microscopy (STM) and spectroscopy (STS) with scattering-type scanning near-field optical microscopy (s-SNOM). Our STM/STS results reveal that p-n junctions with a band offset of ~0.6 eV can be achieved with widths of ~3 nm, giving rise to electric fields of order 10^8 V/m. Concurrent s-SNOM measurements validate a point-scatterer formalism for modeling the interaction of surface plasmon polaritons (SPPs) with nanobubbles. Ab initio density functional theory (DFT) calculations corroborate our experimental data and reveal the dependence of charge transfer on layer separation. Altogether, our study provides a solid experimental foundation for generating p-n nano-junctions in 2D materials, which could have important implications for the development of novel electronic and optoelectronic devices.

6.1 Introduction

Nanoscale lateral p-n junctions in graphene present promising routes for investigating fundamental quantum phenomena such as Andreev reflection[157, 158], whispering gallery mode

resonators[159, 160], quantum dots[161, 162, 163, 164, 165], Veselago lensing[166, 167] and photonic crystals[168]. The ability to realize nano architectures capable of hosting these properties relies on precise control over the lateral p-n junction size–ideally down to atomic length scales. Despite the potential advantages of tailored nanometer junctions, attempts to realize sharp and clean interfacial junctions in graphene-based devices have been limited by the precision of nanolithographic techniques (i.e.,> 20 nm)[167, 169]and lack the nominal potential profile for yielding high-quality devices. Conventional techniques such as local back gating[170], ion implantation[171, 172], and adatoms[173]are practically challenging to implement and can be accompanied by an increase in disorder, reduction in mobility, and surface contamination. Moreover, the maximum charge carrier density achievable with these approaches is typically limited to less than $5\text{x}10^{12} cm^{-2}$,[174, 175]restricting the potential gradients accessible with these techniques. Recent theoretical[176, 177]and experimental[178, 179, 180, 181]work on graphene/α-$RuCl_3$ heterostructures demonstrate that the Dirac-point energy (E_{Dirac}) in graphene will experience a massive shift ($\sim$0.6 eV) due to work function-mediated interlayer charge transfer with the underlying α-$RuCl_3$. While transport measurements suggest a high degree of interlayer charge transfer23in graphene/α-$RuCl_3$ heterostructures($>10^{13} cm^{-2}$), they have not revealed the lateral dimensions of this charging process. On the other hand, analysis of the plasmonic behavior of graphene/α-$RuCl_3$ in the vicinity of nanobubbles suggests that boundaries between highly doped and pristine graphene are no wider than 50 nm[178]. Raman maps conducted on these heterostructures produce similar constraints on the maximum size of lateral charge modulation boundaries[180].

However, a detailed understanding of the nanoscale spatial dependence of interlayer charge transfer between graphene and α-$RuCl_3$ necessitates the use of a high-resolution local probe. In order to elucidate the intrinsic lateral and vertical length scales associated with interlayer charge transfer in graphene/α-$RuCl_3$ heterostructures, we employ two complementary imaging and spectroscopic techniques: scanning tunneling microscopy and spectroscopy (STM/STS) and scattering-type scanning near-field optical microscopy (s-SNOM). STM and STS are ideal probes for studying lateral junction interfaces (e.g.,p-n, p-p', p-i-p, etc.)with atomic resolution and provide infor-

mation about the local electronic structure(in particular, E_{Dirac} in graphene).On the other hand, s-SNOMuses hybrid light-matter modes known as surface plasmon polaritons (SPPs) to probe the local conductivity in graphene. This multi-messenger experimental approach provides a multi-faceted view of the fundamental length scales associated with interlayer charge transfer as encoded in both the electronic and plasmonic responses of graphene/α-$RuCl_3$.

We use nanobubbles that arise spontaneously at the graphene/α-$RuCl_3$ heterostructure interface during fabrication as a test bed for probing the in-plane and out-of-plane behavior of interlayer charge transfer. Differential conductivity (dI/dV) maps and point spectroscopy performed at the boundary of nanobubbles reveal that highly-doped and intrinsically n-doped graphene are separated by a lateral distance of ∼3 nm and vertically by ∼0.5 nm, generating internal fields on the order of 10^8V/m. In addition, the rapid change in the graphene conductivity in the vicinity of nanobubbles acts as a hard plasmonic barrier that reflects SPPs generated during s-SNOM measurements, as observed previously[178]. The results of STS measurements inform our interpretation of the s-SNOM data and permit us to further develop our model for the complex-valued near-field signal associated with nanobubble-scattered SPPs using a perturbative point-scatterer approach. Our results are well supported by first-principles density-functional theory (DFT) calculations, which reveal the origin of the sharp spatial profile of interlayer charge transfer at the boundary of nanobubbles.

6.2 Device Fabrication

α-$RuCl_3$ crystals were grown by the sublimation of α-$RuCl_3$ powder sealed in a quartz tube under vacuum. About 1g of powder was loaded in a quartz tube of 19 mm in outer diameter, 1.5 mm thick, and 10 cm long. The growth was performed in a box furnace. After dwelling at 1060°C for 6 h, the furnace was cooled to 800°C at a rate of 4°C/h. Magnetic and specific heat measurements confirmed that the as-grown pristine crystal orders antiferromagnetically around 7 K. For more information, see ref [182]. α-$RuCl_3$ is notoriously difficult to pick up using standard dry stacking techniques. To overcome this limitation, we modify the usual dry stacking procedure

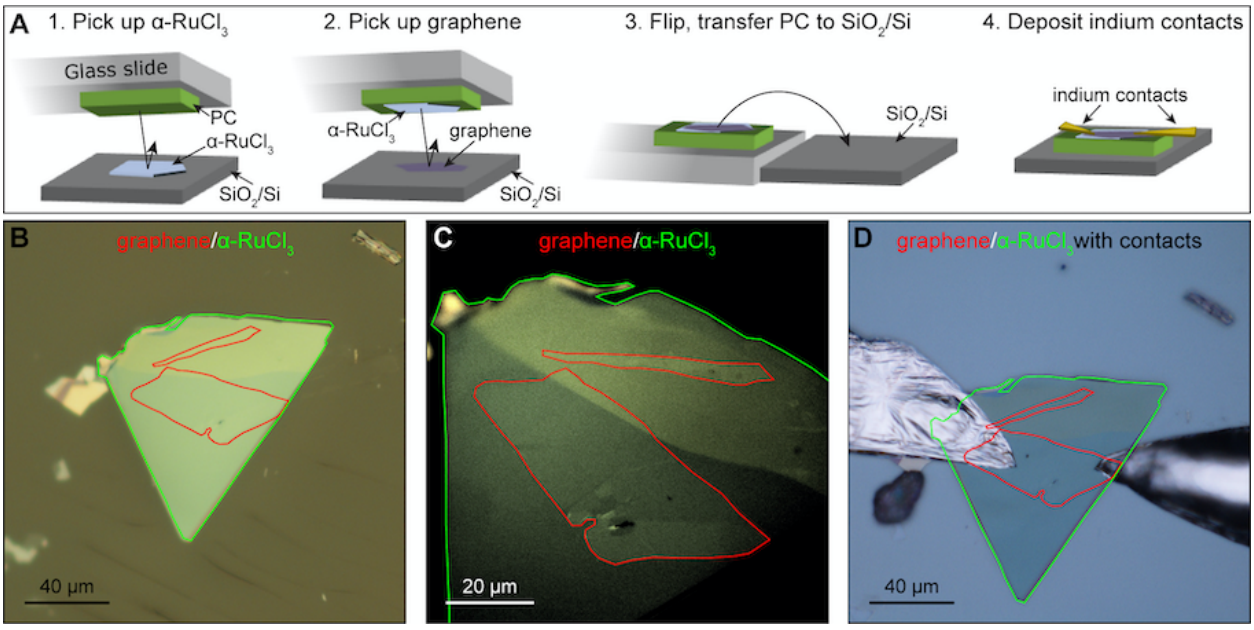

Figure 6.1: Graphene/α-$RuCl_3$ device fabrication. **a** Diagram of four steps for graphene/α-$RuCl_3$ device assembly. In the first step, a PC-coated glass slide is used to pick up exfoliated α-$RuCl_3$ on a SiO2/Si substrate. In the second step, the α-$RuCl_3$/PC transfer slide is used to pick up exfoliated graphene. In the third step, the transfer slide is flipped over and the PC is delaminated from the glass slide and placed on a SiO2/Si chip. In the final step, indium contacts are deposited on the device using a micro-soldering approach.1 **b** Optical image of graphene/α-$RuCl_3$ device with the graphene outlined in red and the α-$RuCl_3$ outlined in green. **c** High contrast magnified image of the stack shown in (b). **d** Optical image of the graphene/α-$RuCl_3$ device after the deposition of indium contacts.

in the following ways: When exfoliating α-$RuCl_3$ onto SiO2, we avoid any plasma treatment of the SiO2 prior to exfoliation. This reduces the adhesion of the α-$RuCl_3$ to the SiO2 (albeit at the expense of the yield of large-area crystals, which were not needed in this experiment). To pick up the α-$RuCl_3$, we employ PDMS stamps coated with poly(bisphenol a carbonate) (PC). The PC is heated above the glass-transition temperature (Tg = 150°C) to 170°C, leaving the film in a low viscosity state. We then slowly cover the targetα-$RuCl_3$ flake and leave the PC in contact with the α-$RuCl_3$ for at least 10 minutes to ensure high coverage. Next, we lower the temperature to below Tg, solidifying the PC film around the α-$RuCl_3$ crystal and significantly increasing the chance of a successful pick-up. We note that the temperature should not be raised higher than the values provided here, as the α-$RuCl_3$ will readily decompose in ambient at temperatures above 200°C. After the α-$RuCl_3$ is successfully picked up, we can use more standard parameters to subsequently pick up other 2D materials (e.g., graphene). Using this approach, α-$RuCl_3$ flakes and single-layer graphene were sequentially lifted from SiO2/Si substrates using a PC-coated glass transfer slide. The PC together with the stack was flipped onto a Si/SiO2 (285 nm Si) substrate held at 150 Celsius. Indium alloy contacts were placed on the graphene using a micro soldering technique1 to provide electrical contacts for STM measurements. This technique preserves sample quality compared to lithography methods. See Figure 6.1 for a diagrammatic procedure.

6.3 Graphene/α-$RuCl_3$ Topography

The graphene/α-$RuCl_3$ heterostructures studied herein were fabricated using dry transfer techniques from components isolated using exfoliation from single-crystal sources as described in the previous section. The resulting heterostructure consists of large regions of graphene forming a flat interface with the underlying α-$RuCl_3$, which are occasionally interrupted by graphene nanobubbles (Fig. 6.2a)(see Fig. 6.3 for STM topographic overview). A high-magnification topographic STM image of a characteristic graphene nanobubble is shown in Fig. 6.2b. As observed with STM topography, the typical heights of nanobubbles studied in this work were between 1 to 3 nm, while the radius ranged from 20 to 80 nm. Topographic images collected with an atomic force

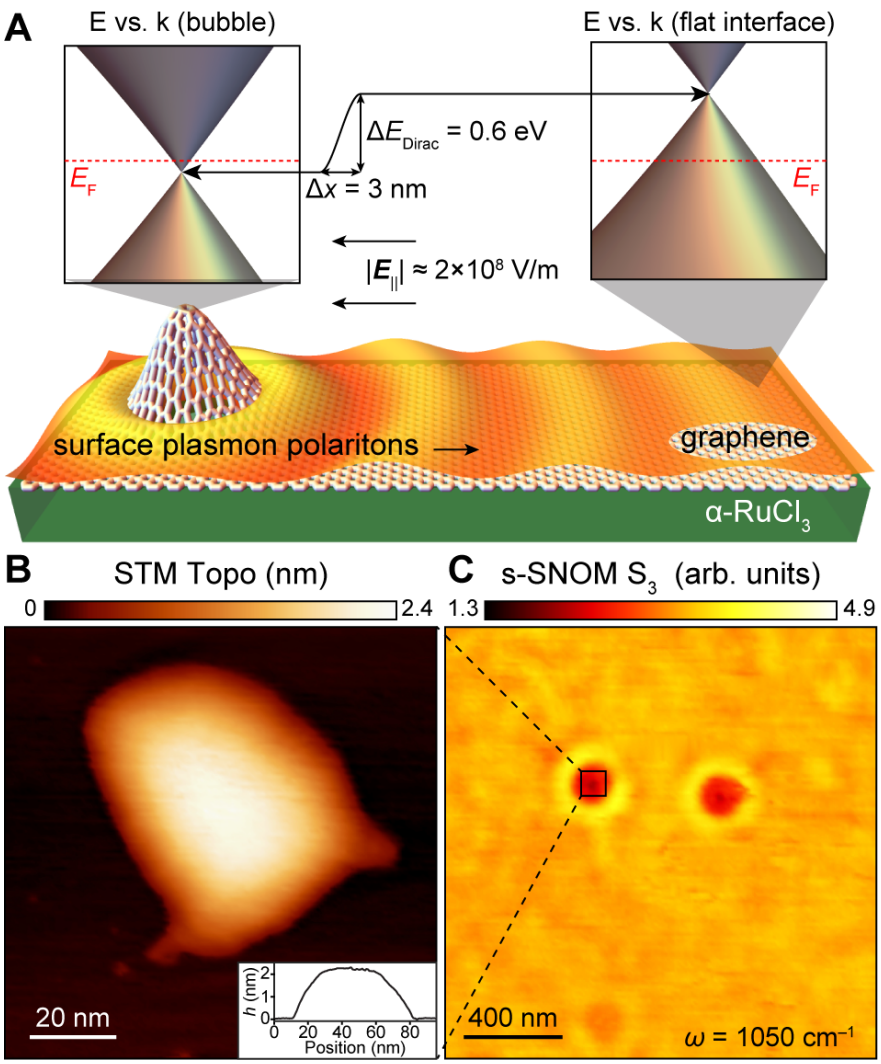

Figure 6.2: Overview of joint STM/s-SNOM investigation of nanobubbles in graphene/α-$RuCl_3$ heterostructures. **a** Schematic of Dirac-point energy shift between nanobubbles and clean flat interfaces in graphene/α-$RuCl_3$ heterostructures. The ~0.6 eV energy shift takes place over a lateral length scale of < 3 nm at the boundary of nanobubbles, generating effective lateral fields of E $\approx 2\times10^8$ V/m (0.2 V/nm). Since the pristine graphene suspended in the nanobubble is intrinsically n-doped, a p-n junction is created at the nanobubble boundary. The associated jump in the graphene conductivity at the perimeter of the nanobubble acts as a hard boundary for the reflection of surface plasmon polaritons. **b** Characteristic STM topographic image of a nanobubble (V_S = 0.7 V, I_t = 50 pA). The inset shows the one-dimensional cross-section of the nanobubble topography. **c** Characteristic s-SNOM image of two nanobubbles shows circular fringe patterns corresponding to radially-propagating surface plasmon polaritons ($\omega = 990\ cm^{-1}$).

microscope (AFM)used during s-SNOM measurements yield similar nanobubble dimensions (Fig. 6.3).

On the other hand, near-field images of these same nanobubbles collected using s-SNOM reveal larger circular features that extend over lateral distances of several hundred nanometers (Fig. 6.2c). The oscillatory nature of the near-field signal moving radially from nanobubbles is consistent with the presence of SPPs that are either being launched or reflected from these locations, giving rise to modulations in the near-field signal that extend far beyond the nanobubble area. It has been suggested that these plasmonic features arise due to discontinuities in the graphene conductivity associated with local modulation of charge carrier density[178], though the precise nature of this profile demands further scrutiny with STM and STS.

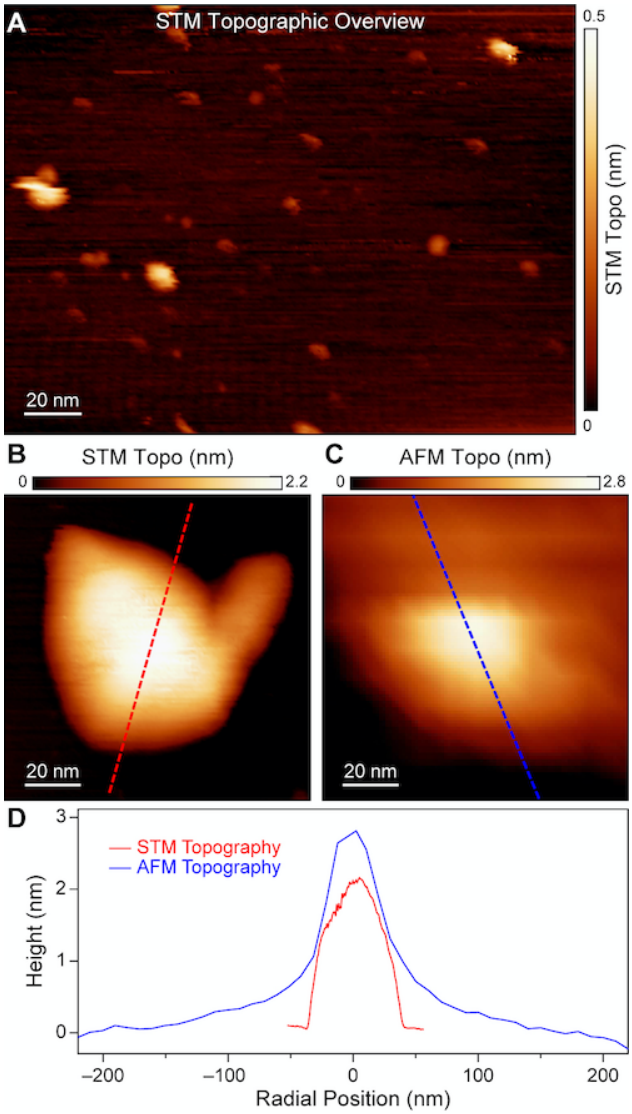

Figure 6.3: STM and AFM topographic data. **a** STM topographic overview of graphene/α-$RuCl_3$ (V_S = 0.7 V, I_t = 50 pA) showing that both flat regions and nanobubbles are present. **b** High magnification STM topographic image of a typical graphene nanobubble (V_S = 0.7 V, I_t = 50 pA). **c** High magnification AFM topographic image of a typical graphene nanobubble. **d** Topographic line profiles based on the images in (b) and (c) showing that typical nanobubbles measured in STM (red curve) have a similar topography to those viewed with AFM and s-SNOM (blue curve).

6.4 Scanning Tunneling Spectroscopy

In order to gain insight into the spatial dependence of interlayer charge transfer, we performed a series of STM and STS measurements in the vicinity of graphene nanobubbles(Figs. 6.4, 6.5).

Figure 6.4a shows two representative point spectra collected on a flat interface of graphene/α-$RuCl_3$ (red curve) and on a nanobubble (blue curve). The spectrum taken on the nanobubble(blue curve)is characteristic of slightly intrinsically n-doped graphene since the Dirac point is located at –0.1 eV relative to the Fermi energy E_F. This spectrum acts as a reference for the pristine graphene density of states. On the other hand, the dI/dV spectrum on the flat graphene/α-$RuCl_3$ region(red curve)away from the nanobubble junction shows a shift in the Dirac point energy of E_{Dirac}= +0.625 eV relative to pristine graphene suspended in the nanobubble. This massive shift in E_{Dirac}corresponds to a hole density in graphene greater than1013cm-2resulting from interlayer charge transfer with α-$RuCl_3$. We attribute the local minimum close to $E_F$observed for both spectra to the ubiquitous inelastic tunneling gap that arises due to phonon-mediated processes independent of the graphene doping level[175]. This direct observation of heavily p-doped graphene on α-$RuCl_3$ by STM is consistent with the previous optical and transport studies[178, 179, 180, 181] and demonstrates that p-n junctions are formed at the nanobubble boundaries. To visualize nanobubble p-n junctions, dI/dV maps were conducted at biases corresponding to $E_{Dirac}$for both the nanobubble and flat interface regions (Fig. 6.4b). The spectroscopic map conducted at-100 mV associated with $E_{Dirac}$of the nanobubble shows high LDOS on the surrounding graphene/α-$RuCl_3$ compared to the nanobubble area with a jump in the LDOS at the boundary between these two regions that occurs over a lateral length scale of approximately 3 nm (green curve, Fig. 6.4c). This is consistent with the expectation that the nanobubble should have a suppressed LDOS at its E_{Dirac}compared to the surrounding highly doped regions. By the same reasoning, at +525 meV (i.e.,$E_{Dirac}$of the flat graphene/α-$RuCl_3$ interface)the LDOS is enhanced on the nanobubble compared to the surrounding flat graphene/α-$RuCl_3$ region.A similarly abrupt shift in the LDOS at the nanobubble edge is observed at this energy (purple curve, Fig. 6.4c). This behavior is character-

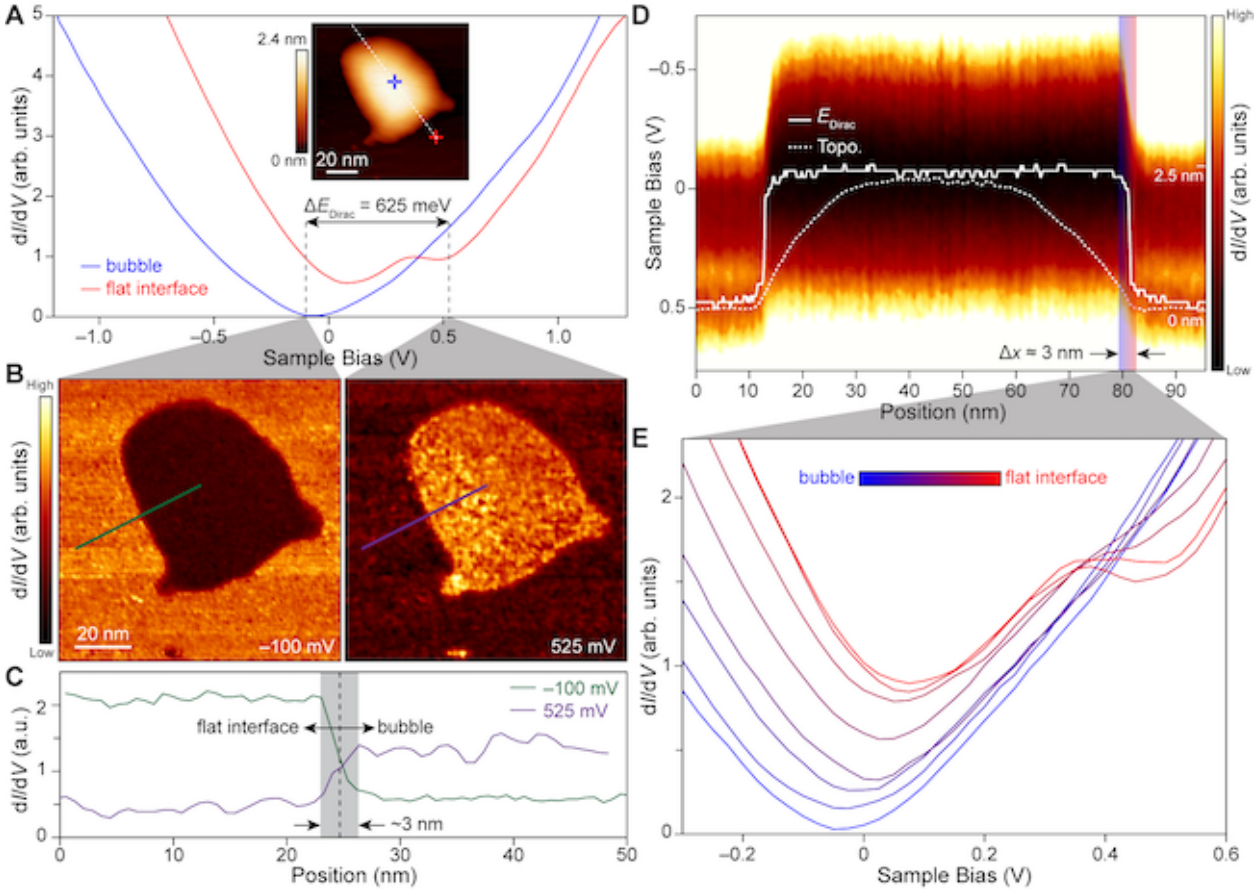

Figure 6.4: Electronic structure characterization of nanobubbles in graphene/α-$RuCl_3$ using STM and STS. **a** Inset: STM topographic image of a graphene nanobubble (V_S = 0.7 V, I_t = 50 pA). Representative dI/dV point spectroscopy collected over nanobubbles (blue) and flat graphene/α-$RuCl_3$ interfaces (red) as indicated by the crosshairs in the inset. Between these two spectra, the graphene Dirac point shifts by 625 meV. **b** dI/dV maps of a graphene nanobubble conducted at the indicated biases corresponding to the Dirac point energies on the nanobubble (left panel) and the flat interface (right panel) (V_{AC} = 25 mV, I_t = 50 pA). A suppressed LDOS is observed at those biases associated with the local Dirac point energy. **c** Linecuts of the dI/dV maps shown in (b) following the green and purple lines indicated on the –100 mV and 525 mV maps, respectively. In both instances, the change in the LDOS at the bubble boundary (indicated by the black dashed line) takes place over a lateral length of approximately 3 nm. **d** Position-dependent dI/dV point spectroscopy collected along the dotted white trajectory shown in the inset in (a). The shift in the Dirac point energy occurs over a lateral length scale of ~3 nm as indicated by the region highlighted in partially transparent red and blue. The position-dependence of the Dirac point energy (solid white line) is superimposed on the topographic line cut (dotted white line) showing that the prior has a much more abrupt spatial dependence. **e** Sample dI/dV point spectra collected at the threshold of a graphene nanobubble corresponding to the red and blue highlighted region in (c).

istic of a nanometer-scale p-n interface in graphene located at the nanobubble boundary. We note that these nanobubble p-n junctions resemble quantum dots previously shown to host quasi-bound states, but would require a spectral resolution beyond what is achievable in the present room temperature study to be visualized. We then extracted the potential profile across the p-n junction and evaluated its sharpness. A representative dI/dV linecut is shown in Fig. 6.4d and follows the white trajectory highlighted in the inset of Fig. 6.4a. Fig. 6.4d clearly shows that the local minimum of the Dirac point shifts abruptly at the boundary of the nanobubble from +0.525 eV to –0.1 eV over a length scale of only a few nanometers. To provide information about the correspondence between STM topography and the shift in E_{Dirac}, we compare the nanobubble topographic cross-section (denoted with a white dotted line in Fig. 6.4d)with the Dirac energy position(solid white line). It is evident that the change in the graphene doping level occurs much more abruptly than the height profile of the nanobubble, implying that interlayer charge transfer is rapidly suppressed with interlayer separation. The lateral junction width is measured to be ∼3 nm as indicated in Fig. 6.4d. The lateral width of this depletion region is roughly one order of magnitude smaller than previously reported results on state-of-the-art split back gate devices[169]. To provide a step-by-step view of the evolution of E_{Dirac}across the junction, a few spectra from the junction region are shown in Fig. 6.4e. Once the interface of the nanobubble is reached and the graphene is separated from the underlyingα-$RuCl_3$ layer by less than 1 angstrom, the minimum corresponding to the Dirac point at +0.525 eV rapidly shifts to lower biases. Beyond this point, E_{Dirac}shifts more gradually until it reaches its minimum value of –100 mV(The dependence of the shift in E_{Dirac}on the nanobubble height is shown explicitly in Fig. 6.4d). All STM/STS measurements were carried out on a commercial RHK system under ultra-high vacuum conditions. An etched Tungsten tip was prepared and calibrated on an Au(111) single crystal. The topographic images were collected in constant current and bias mode using a feedback loop. The STS point spectra were obtained at constant height under open feedback loop conditions with a modulating bias of 25 mV using a lock-in amplifier. dI/dV maps were extracted from a grid of individual point spectra collected in the vicinity of nanobubbles. All measurements were performed at room temperature to permit direct tunneling

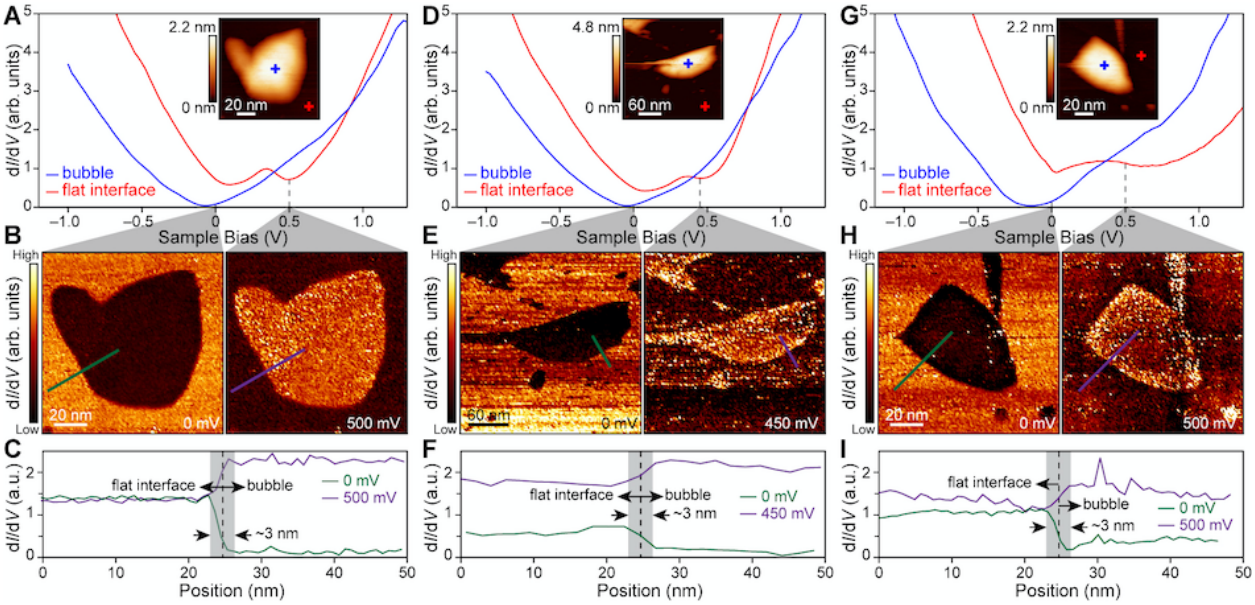

Figure 6.5: STM and STS of multiple nanobubbles. **a**Inset: STM topographic image of a second graphene nanobubble (V_S = 0.7 V, I_t = 50 pA). Representative dI/dV point spectroscopy collected over nanobubbles (blue curve) and flat graphene/α-$RuCl_3$ interfaces (red curve) as indicated by the crosshairs in the inset. **b** dI/dV maps of a graphene nanobubble conducted at the indicated biases corresponding to the Dirac point energies on the nanobubble (left panel) and the flat interface (right panel) (V_AC = 25 mV, I_t = 50 pA). A suppressed LDOS is observed at those biases associated with the local Dirac point energy. **c** Linecuts of the dI/dV maps shown in (B) following the green and purple lines indicated on the 0 mV and 500 mV maps, respectively. In both instances, the change in the LDOS at the bubble boundary (indicated by the black dashed line) takes place over a lateral length of approximately 3 nm. **d, e, and f** same as (a), (b), and (c), respectively, but for a third graphene nanobubble. **g, h, and i** same as (a), (b), and (c), respectively, but for a fourth graphene nanobubble.

into α-$RuCl_3$ (which is otherwise too resistive at cryogenic temperatures to permit local tunneling measurements).

6.5 Plasmonic Response

Armed with the results of STM and STS experiments, we now return to s-SNOM images conducted on graphene nanobubbles. Data were collected on five different nanobubbles over a frequency range of 930 –2280 cm–1(Fig. 6.6). Characteristic images of the near-field amplitude and phase for $\omega = 990cm^{\breve{}}1$ are shown in Fig. 6.6a. Immediately outside the radius of the nanobubble, radial oscillations of both near-field channels decay as a function of distance as shown in Fig. 6.6c. As expected, the spacing between fringes clearly disperses with frequency (Fig. 6.7).

In principle, these fringes could arise from SPPs generated on and propagating away from nanobubbles (λ_p fringes), from SPPs generated at the AFM tip that reflects from the nanobubble boundary(λ_p/2 fringes), or from both. Previous work on similar heterostructures would suggest the near-field behavior is primarily dominated by the latter. To definitively resolve this question, it is useful to consider that the STS data provides unambiguous evidence that the entirety of the graphene nanobubble consists of nominally undoped graphene surrounded by highly-doped graphene with a boundary width on the order of only a few nanometers. We, therefore, model the s-SNOM data of a graphene nanobubble as a raster-scanned dipole over a circular conductivity depletion region surrounded by a bulk possessing high conductivity in a manner similar to our previous study[178](Fig. 6.6b). Expanding on this previous work, we now consider that the SPPs generated at the AFM tip during s-SNOM measurements may possess a wide range of wavelengths relative to the size of the nanobubble. At one extreme, the SPP wavelength is much larger than the nanobubble and can pass through with little to no scattering.

Here, a maximum in both the near-field amplitude and phase is observed at the location immediately outside the nanobubble boundary. At the other extreme, the SPP wavelength is too small to effectively couple to a finite-sized tip, suppressing the generation of SPPs. At intermediate length scales where the SPP wavelength is on the order of several times the nanobubble dimensions, plasmonic reflections are observed that result in λ_p/2 fringes whose amplitude scale is the nanobubble radius(Fig. 6.6b). In contrast to the behavior at large p, here the near-field amplitude possesses a

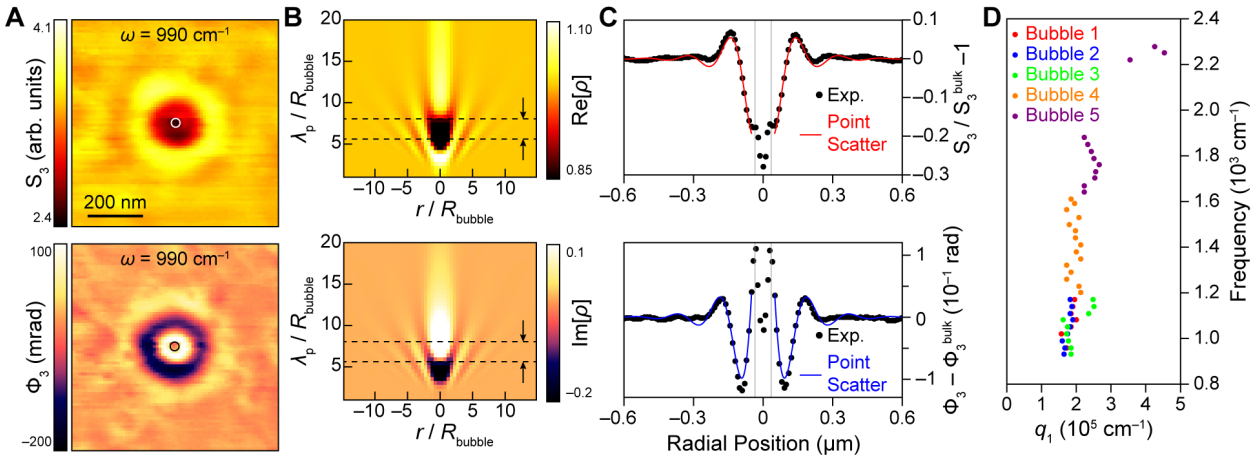

Figure 6.6: Characterization of plasmonic response of nanobubbles using s-SNOM. **a** s-SNOM S_3 amplitude (top panel) and ϕ_3 phase (bottom panel) collected over a graphene nanobubble (ω = 990 cm^{-1}). The bubble perimeter is indicated in each image with a white and black circle, respectively. A characteristic fringe pattern is observed in both the near-field amplitude and phase emanating radially from the bubble. **b** Simulated near-field amplitude (top panel) and phase (bottom panel) based on a raster-scanned dipole over a defect with fixed radius Rbubble and a variable SPP wavelength λ_p. The radial dependence r/R_{bubble} of both amplitude and phase are shown. The black arrows and black dashed box enclose the regime of λ_p/R_{bubble} that resembles the experimental data. **c** Radial line cuts of the images shown in (a) averaged over half-annuli with thicknesses of δr = 10 nm. The gray vertical lines indicate the boundaries of the nanobubble. Based on a model that treats the nanobubble as a point scatterer, the radial dependence of the near-field amplitude and phase is simultaneously fit to the real and imaginary components of $-A[H_1^{(1)}(q_p r)]^2$, respectively ($H_1^{(1)}$) is the Hankel function of first kind of order one, q_p is the complex SPP wavevector, r is the radial coordinate and A is a complex amplitude). **d** The corresponding dispersion of SPPs emanating from five different nanobubbles is extracted using the fitting procedure described in (c).

minimum immediately outside the defect, while the phase has a maximum. A comparison of the experimental and simulated near-field images is shown in Figs. **??**a and b suggest that our experiment takes place in this intermediate regime where plasmonic reflections give rise to $\lambda_p/2$ fringes that generate an amplitude minimum and phase maximum at the nanobubble boundary (indicated by the black dashed boxed region in Fig. 6.6b). In principle, λ_p fringes could exist concurrently as a result of light scattering directly from vacuum into the graphene from the nanobubble itself. Such fringes would have a systematic angular-dependent near-field signal enforced by the angle of the incident light projected onto the 2D plane. Since a systematic angular dependence is neither observed in near-field amplitude nor phase(Fig. 6.7), we exclude the possibility that λ_p fringes are substantially contributing to the observed SPP oscillations. An approximate representation of the radial dependence of the near-field amplitude can be derived by perturbatively treating the nanobubble as a point scatterer. This is a 2D analogue of Rayleigh scattering and may be useful for the analysis of SPP dispersions in a manner analogous to quasiparticle interference (QPI) of 2D electronic states[183, 184]. Within this framework, the scattered polariton field is used as a proxy for the near-fields signal and has the functional form of $-A(H_1^{(1)}(q_p r))^2$, (here, $H_1^{(1)}$ is the Hankel function of the first kind of order one, $q_p = q_1 + iq_2$ is the complex SPP wavevector, is the radial coordinate, and is A complex scaling factor). The real and imaginary components of this function are simultaneously fit to the near-field amplitude and phase, respectively, using A and q_p as fitting parameters. The resulting model line profiles faithfully reproduce the experimental data (Fig. 6.6c). Repeating this fitting procedure for all experimental frequencies and all five bubbles yields the SPP dispersion $\omega(q_1)$ (Fig. 6.6d). The shape of the experimental dispersion is consistent with SPPs propagating in highly doped graphene. All s-SNOM measurements were conducted using a commercial Neaspec system under ambient conditions using commercial Arrow TM AFM probes with a nominal resonant frequency of f = 75 kHz. Three tunable continuous wave quantum cascade lasers produced by Daylight Solutions were used, collectively spanning wavelengths from 4 to 11 m. The detected signal was demodulated at the third harmonic of the tapping frequency in order to minimize background contributions to the scattered light. Simultaneous measurement of the scat-

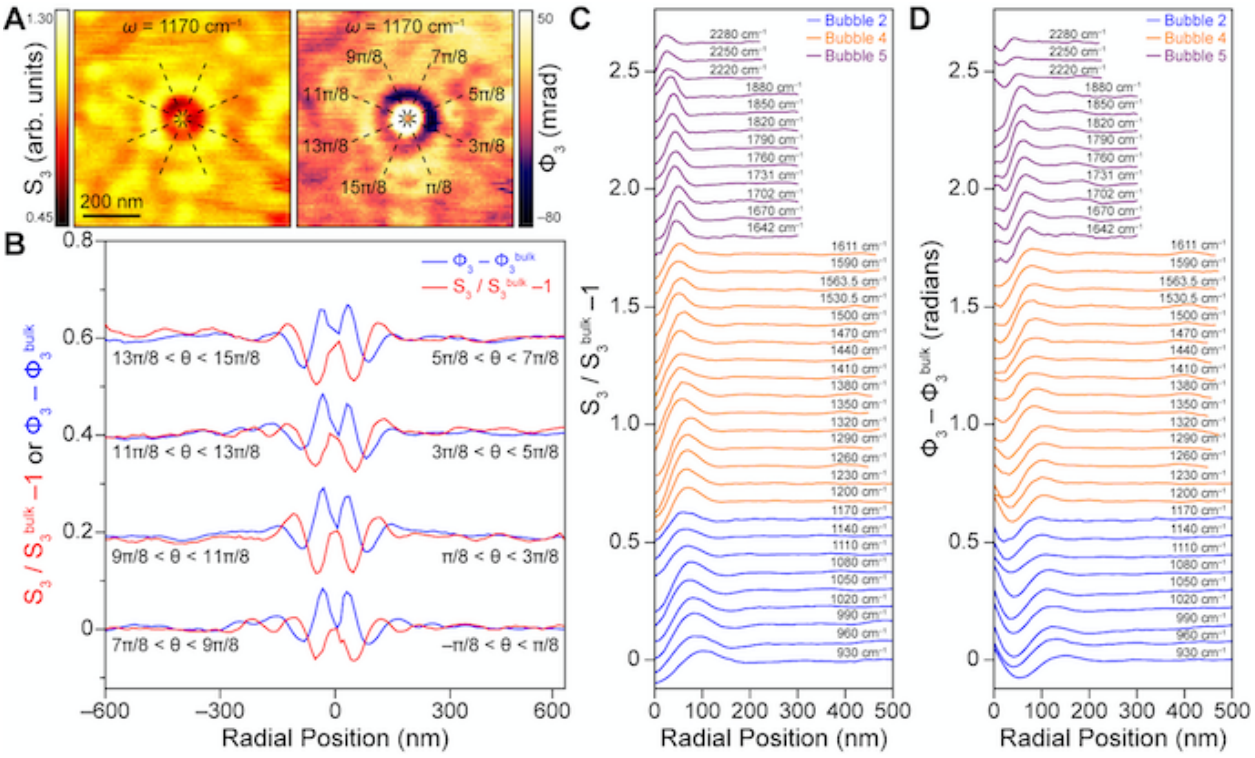

Figure 6.7: S-SNOM on multiple nanobubbles with ω- and angle-dependent near-field linecuts. **a** s-SNOM S3 amplitude (left panel) and ϕ_3 phase (right panel) collected over a graphene nanobubble (ω = 1170 cm–1). The black dashed lines separate the s-SNOM maps into eight angular slices used for the analysis in (b). **b** The radial dependence of the s-SNOM S3 amplitude (red curves) and ϕ_3 phase (blue curves) integrated over the indicated angles designated in (a). The lack of a systematic angular dependence suggests that $_p$ fringes do not contribute significantly to the plasmonic response of nanobubbles. **c** The radial dependence of the S3 amplitude is shown for frequencies spanning $\omega = 930\ cm^{\check{}}1 - 2280\ cm^{\check{}}1$ collected on bubble 2 (blue curves), bubble 4 (orange curves) and bubble 5 (purple curves) referenced in Figure 6.6 of the main manuscript. Since bubbles 1, 2, and 3 all overlap in frequency, only bubble 2 is shown for clarity. All line profiles are truncated at the boundary of the associated nanobubble. **d** Same as (c) but for the radial dependence of the ϕ_3 phase.

tering amplitude and phase was performed through the use of a pseudoheterodyne interferometer.

6.6 DFT Results

Both experimental STM/STS and s-SNOM data provide corroborating evidence that interlayer charge transfer between graphene and α-$RuCl_3$ is eliminated in nanobubbles as a result of < 1 nm of interlayer separation. We now inquire into the precise mechanism by which this charge transfer takes place and how it is suppressed in nanobubbles through a series of DFT calculations on model

graphene/α-$RuCl_3$ heterostructures. Specifically, we explored the role of an intermediate vacuum region between the two layers varying from 0 to 5 Å above the equilibrium separation (Fig. 6.8a). As reported previously[178], the shift in $E_{Dirac}$for the graphene/α-$RuCl_3$ heterostructure with an equilibrium interlayer separation (h_{min}= 3.3 Å) is observed to be 0.54 eV, in good agreement with the experimental data on flat interface regions(Fig. 6.8b). Expanding on this previous result, we show that the theoretical shift in E_{Dirac}effectively disappears once a vacuum spacer layer of just h= h–h_{min}=5 Å is introduced (Fig. 6.8b), revealing a rapid decay in the interlayer charge transfer with layer separation. The theoretical dependence of E_{Dirac}at intermediate interlayer separations shows a rapid jump for h < 1 Å followed by a more gradual decay in the interlayer charge transfer at larger separations(Fig. 6.8c).

The experimental counterpart to this data can be extracted from Fig. 6.4d to visualize as a function of the interlayer separation between graphene and α-$RuCl_3$. Here, $E_{Dirac}$is obtained from the local minima(or curvature maxima when E_{Dirac}presents as a shoulder) of each dI/dV spectrum taken at a known height above the flat region. Figure 6.8c demonstrates that the behavior of the model DFT calculation mirrors the experimental STS: both show two characteristic decay lengths of less than and on the order of a few angstroms, respectively. We speculate that the emergence of two characteristic length scales associated with interlayer charge transfer arises due to a dual mechanism associated with short-range interlayer tunneling and long-range electrostatic effects between the layers. The agreement between theory and experiment shows that the magnitude of interlayer charge transfer is agnostic to the surrounding in-plane charge and strain28environment (i.e., purely dependent on the layer separation). Thus, it would appear that there is little to no charge redistribution in the graphene plane across the nanobubble interface despite large differences in the local charge carrier density. To understand this, we return to the DFT calculations of model heterostructures with variable vacuum spacer layers and plot E_{Dirac}relative to the vacuum energy (green curve in Fig. 6.8d). From this, it is clear that an electrostatic barrier comparable to the offset in E_{Dirac}~ 0.6 eV emerges between the pristine nanobubble and the highly doped graphene/α-$RuCl_3$ region. Ultimately, this large electrostatic barrier enforces the sharp p-n junctions naturally

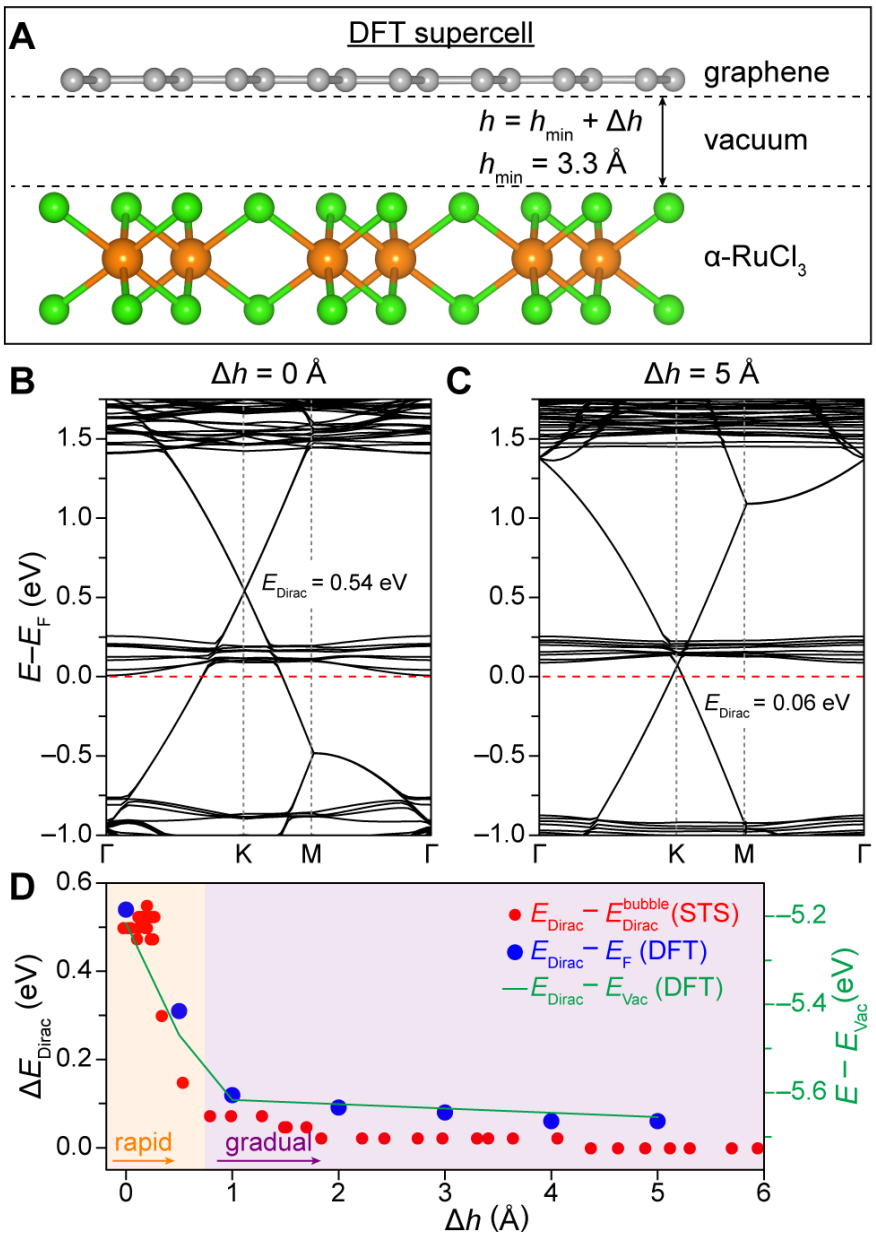

Figure 6.8: DFT and STM analysis of interlayer charge transfer in graphene/α-$RuCl_3$ heterostructures. **a** Side-view of the graphene/α-$RuCl_3$ heterostructure used in DFT calculations. An equilibrium interlayer separation of h_{min} = 3.3 Å is used to model the so-called flat interface observed experimentally. To model the charge transfer behavior between graphene and α-$RuCl_3$ at the edge of nanobubbles (where the interlayer separation increases gradually), additional calculations are performed using interlayer separations of δh = h – h_{min} = 0.5, 1, 2, 3, 4 and 5 Å. Orange, green, and grey spheres indicate Ru, Cl, and C atoms, respectively. **b** Left panel: DFT-calculated band structure for a graphene/α-$RuCl_3$ heterostructure with maximal charge transfer (i.e., h = h_{min} = 3.3 Å). **c** Right panel: Band structure for graphene/α-$RuCl_3$ heterostructure with h = h_{min} + 5 Å, showing minimal interlayer charge transfer. The Fermi levels are set to zero in (b) and (c). **d** The shift in E_{Dirac}relative to its value on the nanobubble plotted as a function of interlayer separation is plotted for both experimental (red dots) and theoretical (blue dots) data. The shift in E_{Dirac}relative to the vacuum energy E_{Vac} is plotted in green. The rapid decay is highlighted in orange, while the subsequent gradual decay is highlighted in purple.

generated in nanobubbles.

In the following we briefly describe the ab initio method used in this work. The ab initio calculations were performed within the Vienna Ab initio Simulation Package (VASP)[185] using a projector-augmented wave (PAW) pseudopotential in conjunction with the Perdew–Burke–Ernzerhof (PBE)[83] functionals and a plane-wave basis set with an energy cutoff at 400 eV. For the heterostructures with graphene and monolayer α-$RuCl_3$, we used a hexagonal supercell containing 82 atoms (composed of a 5×5 graphene supercell and $\sqrt{3} \times \sqrt{3}$ α-$RuCl_3$ supercell). The resulting strain is 2.5 % for the α-$RuCl_3$ monolayer. The surface Brillouin zone was sampled by a $3 \times 3 \times 1$ Monkhorst–Pack k-mesh. A vacuum region of 15 Å was applied to avoid artificial interaction between the periodic images along the z direction. Because of the absence of strong chemical bonding between layers, van der Waals density functional in the opt88 form[156] was employed for structural optimization. All structures were fully relaxed until the force on each atom was less than 0.01 eV^{-1}. Spin-orbital couplings are included in the electronic calculations. With small Bader charges of 7.01 e (out of 8 e) per orbital, the Ru-4d states cannot be considered fully localized, and therefore, the use of large values of U4d is understood as an ad hoc fitting parameter without a physical basis. Instead, each Chlorine 3p orbital charge is 7.34 e (out of 7 e), indicating the importance of employing correction on both Ru and Cl elements. The Hubbard U terms are computed by employing the generalized Kohn–Sham equations within density functional theory including mean-field interactions, as provided by the Octopus package[186, 187] using the ACBN0[188] functional together with the local density approximation (LDA) functional describing the semilocal DFT part. We compute ab initio the Hubbard U and Hund's J for the 4d orbitals of Ruthenium and 3p orbital of Chlorine. We employ norm-conserving HGH pseudopotentials to get converged effective Hubbard U values (1.96 eV for Ru 4d orbitals and 5.31 eV for Cl 3p orbitals) with spin-orbital couplings.

Finally, we consider the influence of screening on p-n nanojunctions. Poor screening in graphene permits long-range inhomogeneous potentials extending > 100 nm from metallic contacts[189, 190]. Contrary to this behavior, mutual doping at the graphene/α-$RuCl_3$ interface leads to the

formation of an interlayer dipole that is largely confined to the first atomic layers of the heterojunction interface. The electrostatics of this situation is analogous to a split-gate device, where the lateral length scale of the associated bare potential near p-n junctions scales with the thickness of the gate dielectric (can be substantially smaller than 100 nm). In this context, the poor screening in graphene is less relevant to the resulting minimum feature size than the length scale of the underlying bare potential. For graphene/α-$RuCl_3$, the effective gate dielectric thickness is on the order of the layer separation (< 1 nm), permitting nanometer-scale depletion regions at nanobubble boundaries.

In conclusion, we have measured the electronic and photonic behavior of nanobubbles in graphene/α-$RuCl_3$ heterostructures, revealing massive shifts in the local interlayer charge transfer over lateral length scales of only a few nanometers. Such narrow p-n junctions in graphene have previously been inaccessible using standard doping techniques and have many potential applications for studying fundamental electronic structure properties in graphene and related materials. At the same time, our results demonstrate that work function-mediated charge transfer is a viable route toward creating nanoscale conductivity features in graphene that act as local plasmon scatterers. The insights gained in our DFT calculations provide a detailed understanding of the dependence of charge transfer on interfacial separation and reveal abrupt electrostatic barriers at nanobubble boundaries enforced by local dipoles that give rise to nanometer p-n junctions. This work provides the experimental and conceptual foundation for future device design and validates the use of interstitial layers in charge-transfer heterostructures to predictively influence the local electronic and plasmonic behavior.

Chapter 7: α-$RuCl_3$ Heterointerfaces

The close proximity of α-$RuCl_3$ to other two-dimensional materials has led to intriguing interfacial physics that has captured the attention of researchers. In this chapter, we will focus on the results obtained using scanning tunneling microscopy (STM) on graphene/α-$RuCl_3$ and WSe_2/α-$RuCl_3$ heterostructures, which are complementary to other theoretical and experimental techniques.

The first part of this chapter discusses the moiré pattern observed in Graphene/α-$RuCl_3$ heterostructures. Moiré patterns occur as a result of a twist angle between layers and lead to a periodic supercell. The STM results show different moiré wavelengths in graphene/α-$RuCl_3$, highly sensitive to the strain fields. A theoretical model, InterMatch model, is introduced to explain this variation in periodicity and predict equilibrium moiré superlattice configurations for the lattice-mismatched graphene/α-$RuCl_3$ interface. This model takes into account the electronic properties of the graphene layer and the α-$RuCl_3$ layer, as well as the lattice mismatch and the twist angle between the two layers. Our STM results are used to validate the InterMatch as an effective method in predicting the charge transfer, strain, and stability of interfaces.

The second part of this chapter focuses on the optoelectronic properties of WSe_2/α-$RuCl_3$ heterostructures. Here we focus on the STM results which demonstrate the electronic property of WSe_2 in contact with α-$RuCl_3$ is significantly modified. Charge transfer between layers gives rise to a massive shift in the Fermi level and results in p doped WSe_2. Additionally, THz-infrared nano-spectroscopy was used to investigate the optoelectronic properties of the heterostructure. Our DFT calculations also confirm the shift of Fermi level to the valence band edge in agreement with experimental findings.

Overall, the results presented in this chapter highlight the potential of α-$RuCl_3$ as a unique two-dimensional material with intriguing interfacial physics. The combination of STM and other

techniques provides a powerful tool for investigating the properties of these heterointerfaces, which can lead to the development of new materials with tailored properties for various applications.

7.1 InterMatch Method and Moiré Pattern of Graphene/α-$RuCl_3$

In this section we introduce a high-throughput computational framework, InterMatch, for efficiently predicting charge transfer, strain, and superlattice structure of an interface by leveraging the databases of individual bulk materials. We implement this method to explain experimental observation of factor of 10 variation in the supercell periodicity within a few microns in graphene/α-$RuCl_3$ by exploring low energy superlattice structures as a function of twist angle using InterMatch.

7.1.1 Introduction

With increasing control in interface fabrication, interfacial systems form an arena of limitless possibilities[191]. Recent developments with moiré heterostructures[192] further enlarged the phase space to include the twist angle. However, the vast space of possibilities also implies it is crucial to go beyond serendipitous discoveries and empirical explorations to effectively harness the intrinsic potential of interfacial systems. The traditional approach to theoretically studying interfaces is to carry out density-functional theory (DFT) calculations on a supercell system consisting of two materials[193, 194, 195, 196, 197]. While such approaches are rigorous, computational limitations regularly require imposing unnatural strain to form a periodic structure. Moreover, the $O(N^3)$ scaling of DFT in the number of electrons N for each such calculation prohibits a comprehensive exploration. Some of us recently proposed an "intermediate scale" approach called Mismatched Interface Theory (MINT)[198], which can predict charge transfer and natural strain approximating one layer of the interface using finite-size scaling of atomic clusters. While MINT calculations are computationally affordable, they are not fast enough for an exhaustive survey in real-time. Therefore, a comprehensive and fast approach to scanning the relevant phase space of interfacial combinations is greatly needed.

With advancements in widely available comprehensive materials databases[199, 200, 201, 202,

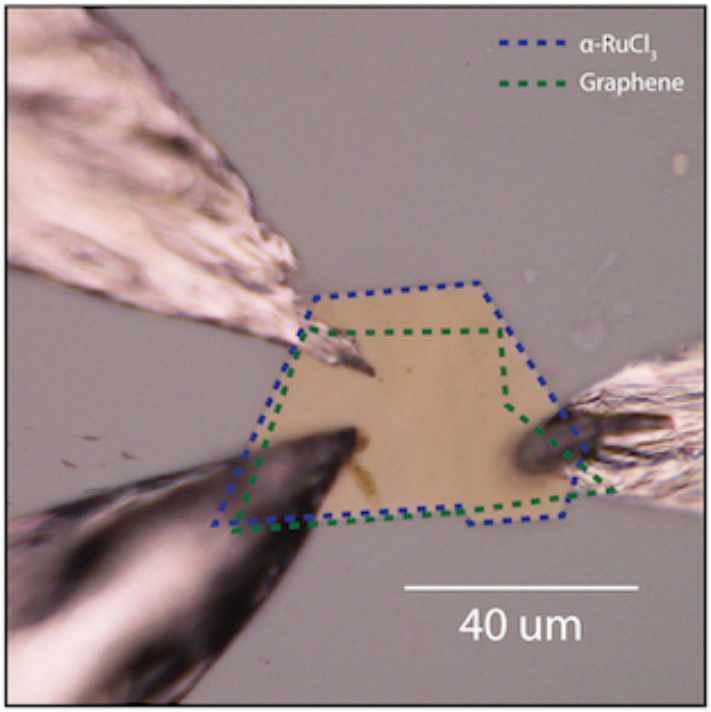

Figure 7.1: Optical image of the measured device of GR/α-$RuCl_3$ contacted with bismuth indium tin for the STM measurements. The blue and green dashed lines show the boundary of α-$RuCl_3$ and graphene, respectively.

203, 204, 205, 206, 207, 208, 209, 210, 211], it is timely to establish a high-throughput approach to interface design that can leverage the information contained in these databases to make predictions of interface physics. Indeed, efforts to make interfacial predictions using bulk material databases are beginning to emerge[212, 213, 214, 215]. However, so far, the existing approaches aid growth and calculation decisions for a specific pair of materials rather than allowing for a comprehensive query to yield fast, approximate predictions over a wide range of possible interfaces. In this work, we benchmark InterMatch predictions for the charge transfer against experimental measurements and supercell DFT predictions.

7.1.2 Brief Overview of InterMatch Method

We introduce InterMatch, which uses information readily available from preexisting materials databases such as the Materials Project and 2DMatPedia databases to predict charge transfer[216],

strain[217], stability[218], and optimal superlattice[219] of an atomic interface. Using these predictions, InterMatch can narrow the candidate pool from $C > O(10^6)$ to $O(10)$ that can then be investigated in greater detail using MINT or supercell DFT. We first illustrate how two branches of InterMatch predict the charge transfer and optimal superlattice after querying the entries of the Materials Project for each of the constituents of the interface. We then benchmark InterMatch predictions for the charge transfer against experimental measurements and supercell DFT predictions. We then employ InterMatch's branches to address two bottleneck problems obstructing design of interfaces towards the goal of discovering new physics: the problem of doping transition metal dichalcogenides and the problem of predicting stable interface structure, applied to the graphene/α-$RuCl_3$ system. We comment on many other classes of interfaces that can be optimized using InterMatch.

7.1.3 STM on Moiré Pattern of Graphene/α-$RuCl_3$

As an example of the power of Intermatch to understand superlattice structure, we consider the graphene/α-$RuCl_3$ heterostructure (graphene/α-$RuCl_3$). This system has attracted great interest due to the presence of strong modulation doping[220] and enhancement of α-$RuCl_3$'s proximity to the Kitaev spin liquid phase. However, relatively little attention has been paid to the atomic scale structure of the heterostructure and the possible influence on electronic properties. In order to study this experimentally, we used scanning tunneling microscopy (STM) to investigate the properties of graphene/α-$RuCl_3$ heterostructures created by mechanical exfoliation, as shown in Fig. 7.1. The angle between the α-$RuCl_3$ substrate and graphene was not intentionally controlled. Shown in Fig. 7.2a-c are a set of STM topographs taken at various locations of the graphene/α-$RuCl_3$ heterostructure. The locations are within a few microns of each other on the sample shown in Fig. 7.1. Intriguingly, all three of the regions show moiré patterns with large wavelengths, 2.7 nm in Fig. 7.2a, 11.7 nm in Fig. 7.2b and 25.7 nm in Fig. 7.2c. All three of these wavelengths are much larger than the wavelength set by the difference in lattice constants.

Using InterMatch, we perform a comprehensive mapping of the space of superlattice con-

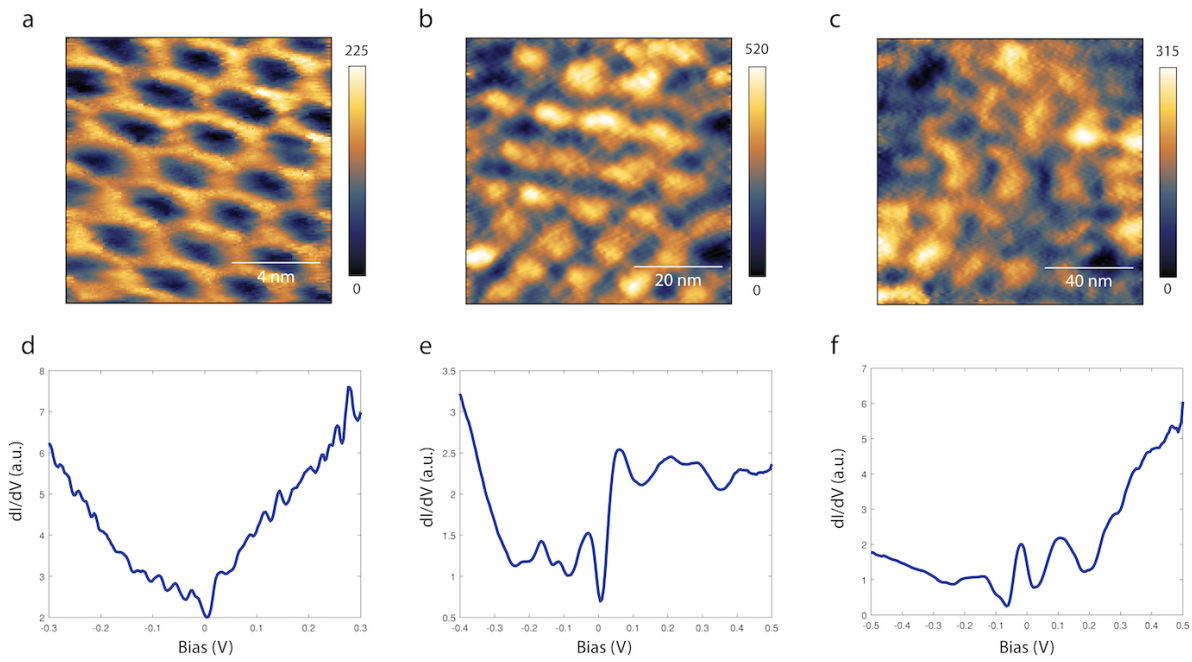

Figure 7.2: Scanning Tunneling Microscopy and Spectrsocopy **a** STM topographic images (in pm) of graphene/α-$RuCl_3$ on 2.7 nm (set points of -100 mV and -100 pA), 11.7 nm and 25.7nm (set points of -1 V and -50 pA) moiré patterns due to atomic reconstruction. **b** dI/dV measurements corresponding to the three moiré patterns in (b)-(d) showing strong resonances dependent on moiré wavelengths.

figurations spanned by $(\theta, L, \mathcal{E})$ where θ is the twist angle, L is the moiré period, and $\mathcal{E}$ is the elastic energy of the interface. The resulting spectrum of low-energy superlattice configurations for $0^\circ \leq \theta \leq 30^\circ$ and $0 \text{ nm} \leq L \leq 30 \text{ nm}$ is shown in Fig. 7.3. We identify four prominent moiré length scales (blue boxes in Fig. 7.3) occurring within a 5° range between 15°-20°. Three of the four length scales coincide with those observed in STM at $L = 2.7,\ 11.7,\ 25.7$ nm, shown in Fig. 7.2a-c. Correctly identifying energetically favorable graphene/α-$RuCl_3$ superlattices over a narrow range of twist angles showcases InterMatch's capability to predict interfacial structure of complex (e.g extremely lattice-mismatched) systems.

The presence of an atomic reconstruction at the interface of graphene/α-$RuCl_3$ can have dramatic consequences for the spectroscopic properties of the material. Shown in Fig. 7.2d-f are scanning tunneling spectra averaged over the regions shown in Fig. 7.2a-c. These spectra show dramatic differences from the simple expectation for a doped Dirac spectrum as might be expected from charge transfer alone. Instead, we observe strong resonances in all three regions, with the

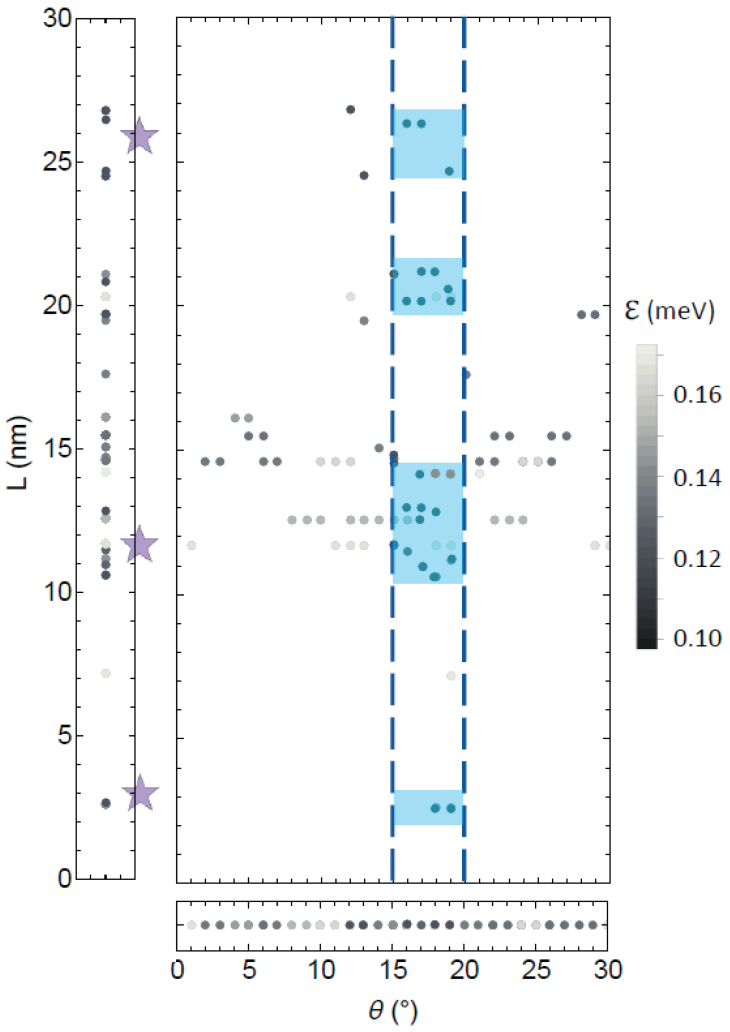

Figure 7.3: InterMatch predictions for low-energy graphene/α-$RuCl_3$ superlattice configurations as a function of period L, twist angle θ, and elastic energy $\mathcal{E}$. Left panel is a projection onto the L-axis, bottom panel is a projection onto the θ-axis. Dashed box indicates interval of θ containing largest range of stable superlattice periods, shaded blue boxes indicate regions of likely superlattice configurations. Purple stars denote the periodicities extracted from the experiment.

spacing between resonances following the expectation from Landau levels on a Dirac spectrum. Previously, such spectra have been observed when graphene has a periodic buckling[221], where it was ascribed to periodic strain in the material. In our case, apart from the strain associated with the moiré lattice[89], we expect that there will also be strong periodic variations in the doping[222] that contribute to the formation of resonances. We showcase the use of InterMatch by identifying high-charge transfer substrates by predicting equilibrium moiré superlattice configurations for the lattice-mismatched graphene/α-$RuCl_3$ interface that are validated by STM measurements. The presence of such long-wavelength superlattice modulations at van der Waals interfaces presents new opportunities to tailor bandstructure using materials that do not have a close match in lattice constants. The evolving interface database provides open access to InterMatch results which we hope will help guide future exploration of interfacial systems.

7.2 WSe_2/α-$RuCl_3$ Heterostructure

We investigate heterostructures composed of monolayer WSe_2 stacked on α-$RuCl_3$ using a combination of THz-infrared nano-spectroscopy and imaging and scanning tunneling spectroscopy (STS) . In this chapter we mostly focus on STM results. Our observations reveal itinerant carriers in the heterostructure prompted by charge transfer across the WSe_2/α-$RuCl_3$ interface. Local STS measurements show the Fermi level is shifted to the valence band edge of WSe_2 which is consistent with p-type doping of TMD. Our experimental results are in agreement with density functional theory (DFT) calculations, which verify significant p-type doping. The results of this work is crucial for future device design and contact engineering in TMD heterobilayer leveraging interfacial physics.

7.2.1 Introduction

Radical modifications of material properties can be produced by proximity effects across interfaces. Work-function mediated charge transfer can enhance the conductivity at interfaces between proximate semiconductors and semi-metals[178, 181]. Layered heterostructures can, further, host interfacial effects including proximity-induced magnetism[179] and proximal superconductivity[223]. Electrostatic screening at interfaces is also known to modify the binding energy of excitons in two-dimensional semiconductors[224]. Transition metal dichalcogenides (TMDs) are particularly well suited for manipulation of spin, valley, and charge degrees of freedom of electrostatic carriers[225]. Their optoelectronic properties are, however, critically dependent on the specific details of excitations in the system[226]. Two types of excitations: bound excitons, and a free electron/hole plasma (EHP), are dominant at the extremes of low and high carrier concentrations in TMDs, respectively. Excitons involve electron and hole pairs which are bound by the Coulomb interaction, forming a bosonic quasiparticle at low densities. At the highest densities the Coulomb interaction, which binds the exciton, is screened and the electronic carriers form a charge separated EHP. In this work, we explore the nanotextured interplay between excitons and

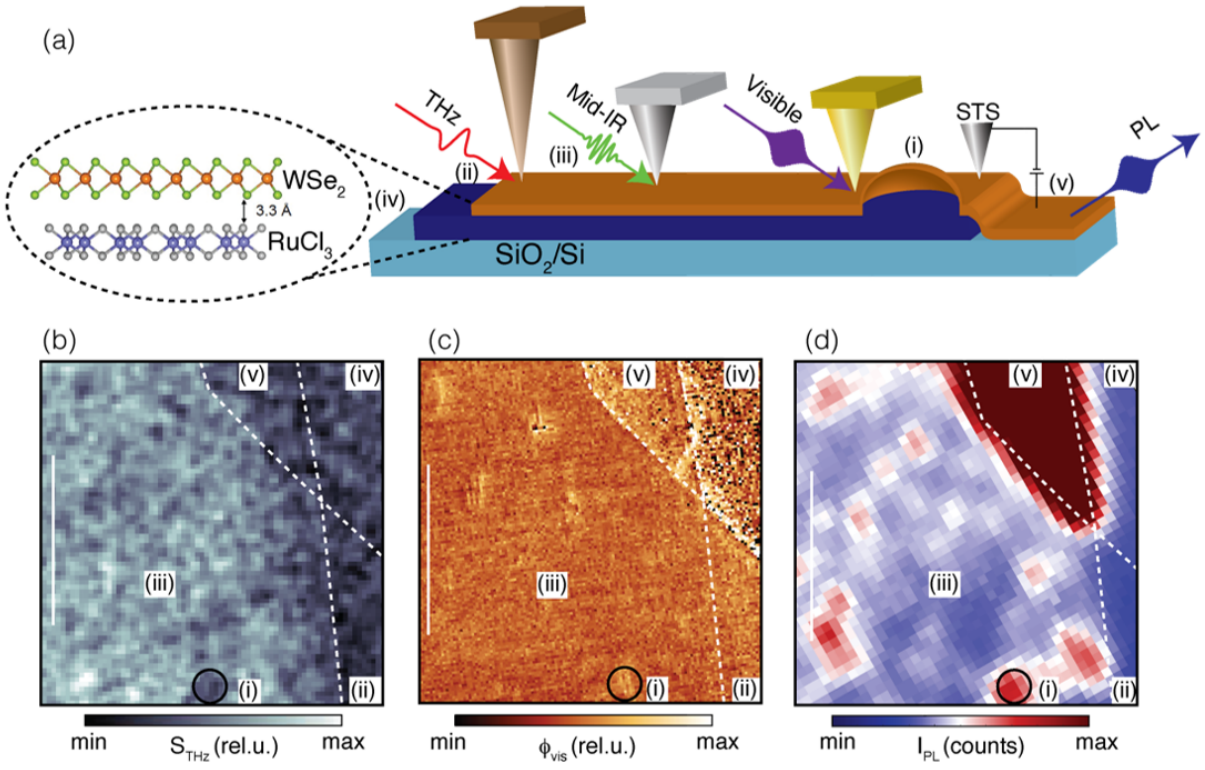

Figure 7.4: Local electrodynamics of excitons and an electron-hole plasma resolved with local multi-messenger spectroscopies. **a** Schematic of the experiment. **b-d** co-located optical images showing (b) spectrally integrated nano-THz amplitude contrast. (c) nano-optical infrared phase measured with 750 nm incident light. (d) Integrated photo-luminance intensity obtained with diffraction-limited spatial resolution.

EHP mediated by charge transfer in WSe_2/α-$RuCl_3$ heterostructures.

7.2.2 Topographies Using Various Methods

To investigate the local properties of WSe_2/α-$RuCl_3$ heterostructures, we employ a multi-messenger nano-imaging / nano-spectroscopy approach, illustrated in Figure 7.4. Representative co-located maps of nano-optical contrast collected with THz and visible radiation are shown in Fig. 7.4b-c. Distinct nano-optical spectra are observed over a broad field of view, where the WSe_2/α-$RuCl_3$ heterostructure (region iii), multilayer α-$RuCl_3$ (region ii) and a WSe_2 monolayer (region v) are identified. Variations of the nano-optical contrast are also observed within the heterostructure (region i). These variations arise from 'nano-bubbles', identified in co-located maps of AFM topography, where WSe_2 is separated from α-$RuCl_3$ by nanometer distances. The observed inhomogeneous contrasts underscore the need for local spectroscopies to investigate the electrodynamics of the WSe_2/α-$RuCl_3$ heterobilayer. Nanoscale spectroscopy provides quantitative information about the characteristics of dipole-active resonances in the heterobilayer. Optical contrasts, with spatial resolution below the diffraction limit, are collected with scanning near-field optical microscopy (SNOM) in Figures 7.4(b) and 7.4(c). In SNOM measurements, the metalized tip of an atomic force microscope (AFM) is illuminated with a laser. The evanescent field, confined to the region around the tip apex, accesses optical contrasts with a spatial resolution of about 20 nm. Conventional methods for nano-optical measurements allow us to extract the complex frequency dependent near-field amplitude and phase of the scattered light as a function of the probe energy, E. Nano-optical contrasts can be used to constrain the local optical response functions of samples. Dipole active resonances – which can originate from a plethora of excitations including excitons, phonons, and free-charge carriers – modify the local optical response function and the measured nano-optical contrast. SNOM, therefore, provides access to the local optical response associated with these resonances with nano-scale spatial resolution.

7.2.3 STM/STS Measurements

Scanning tunneling spectroscopy (STS) measurements directly reveal the modified band alignment of the WSe_2/α-$RuCl_3$ heterostructure and confirm the presence of itinerant carriers at the

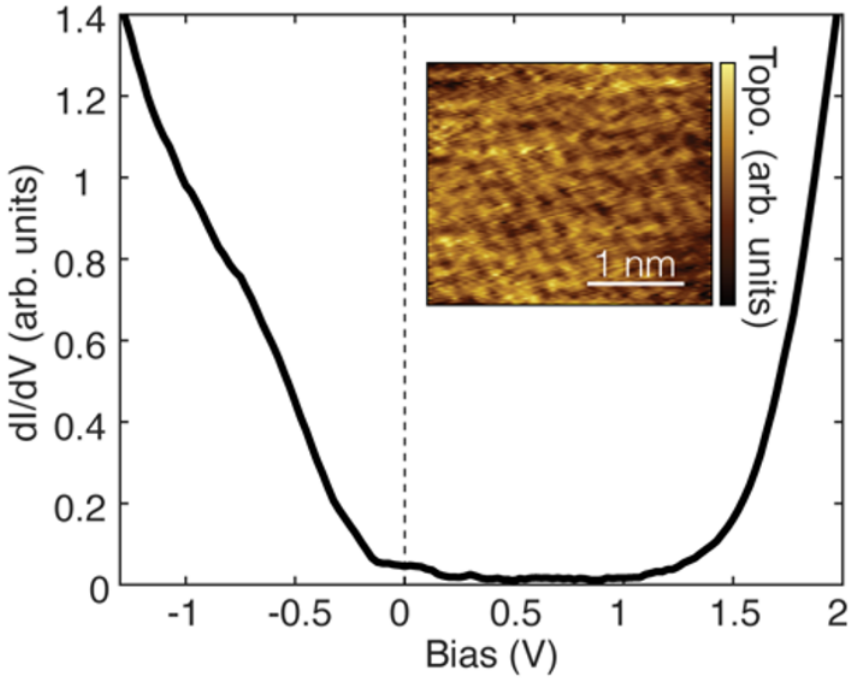

Figure 7.5: STS dI/dV point spectra recorded with current and bias set points of -100 pA and -0.2 V respectively. The inset shows atomic resolution of STM topography from the surface.

interface. Scanning tunneling microscopy (STM) topography recorded at the WSe_2 surface with atomic resolution is shown in the inset of Fig. 7.5 (b). The atomic flatness of the region verifies that WSe_2 and α-$RuCl_3$ are in good contact over the entire investigated area. Scanning tunneling spectroscopy (STS) measurements of the differential conductance (dI/dV) provide information about the density of electronic states (DOS) at various energies. The area-averaged dI/dV spectrum, shown in Fig. 7.5 (b), reveals a ~1.7 V semiconducting gap. Further, the STS spectra show that the Fermi level of WSe_2/α-$RuCl_3$ is shifted to the valence band edge. Our observations in Fig. 7.5b are consistent with the notion of static p-type doping within the heterostructure.

7.2.4 DFT Calculations

DFT calculations corroborate the notion of p-type doping of WSe_2. The bandstructure of WSe_2/α-$RuCl_3$ interface shown in Fig. 7.6 reveals a type-III band-alignment with partially occupied valence bands. These calculations, further, provide a theoretical estimate of the itinerant hole density: $n = 4 \times 10^{12} cm^{-2}$. We remark that the carrier density extracted from our optical

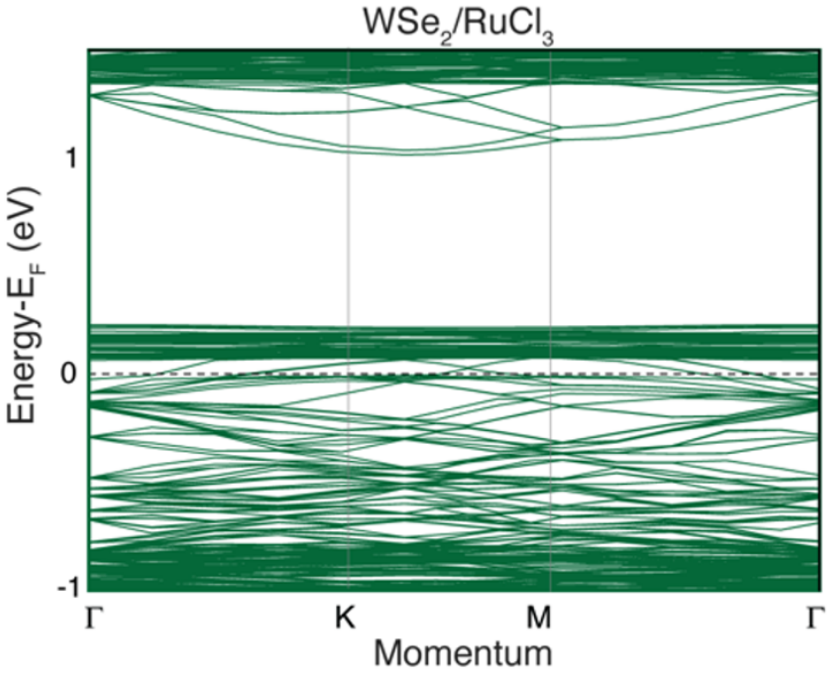

Figure 7.6: DFT calculations reveal itinerant carriers in WSe_2/-α-$RuCl_3$ **a** DFT band structure calculations of the WSe_2/α-$RuCl_3$ heterostructure.

data yields an estimate for the hole density of n = $7 \times 10^{12} cm^{-2}$, which is slightly larger than the theoretically predicted value. These calculations verify that itinerant holes are produced by charge transfer consistent with our STS and SNOM measurements.

We used first-principles calculations to explore the electronic structure of the heterostructure. The charge transfer at the interface is important to understand the interface-modified electronic structures. We obtain that the charge transfer from WSe_2 to α-$RuCl_3$ is 0.20 electrons in the simulated supercell, corresponding to electron doping with the density concentration of n = $3.95 \times 10^{12} cm^{-2}$ in the α-$RuCl_3$ layer.

In conclusion, we have investigated WSe_2/α-$RuCl_3$ heterostructures from THz to visible frequencies and STS spectroscopy all with < 20 nanometer spatial resolution. The experiments and calculations establish an itinerant hole density of n = $7 \times 10^{12} cm^{-2}$. The results are in good qualitative agreement, and in rough quantitative agreement with our DFT theoretical calculations. Heterogeneous densities of bound and itinerant carriers are observed on mesoscopic length scales, which highlights the importance of local spectroscopies in quantitative measurements. The results

of this work opens a new avenue toward contact engineering of TMD heterobilayer using α-$RuCl_3$ and accessing new physics in these materials.

Chapter 8: Conclusion and Outlook

This thesis reveals a wide range of unique properties hosted by 2D materials using STM/STS probes. In particular, we focused on the potential of carrier confinement in TMD heterobilayers and charge transfer based α-$RuCl_3$ heterointerfaces. In each chapter, we discussed interesting optoelectronic properties studied in 2D devices. Nevertheless, there is so much to be done to fully understand the optical and electronic behavior in 2D devices to access novel condensed matter systems and quantum applications. I hope the research presented here has shed light on the vast opportunities that 2D materials can bring and I eagerly look forward to seeing further studies in the field of 2D materials. In the following, I would like to summarize this thesis and provide a few future directions and insights for investigating 2D materials.

Firstly, we showed that small angle twisted WSe_2/$MoSe_2$ is a promising platform to host quantum confinement due to the deep potential created by the moiré pattern. The depth of the potential determined by our work is one order of magnitude larger than the theoretical predictions. We introduced the energy relaxation model to understand the underlying mechanism leading to such a large potential. Our experimental data are well captured by the energy relaxation model showing internal strain and corrugation can lead to band structure modification. The importance of moiré potential is trapped carriers as well as the formation of flat bands which are ideal for investigations of strongly correlated states such as exciton condensate. Exciton condensation is a macroscopic and collective quantum phenomenon due to the high density of electron-hole pairs and the Coulomb interactions. Excitons are expected to be trapped in the 2D array of deep potentials created by moiré due to flat band formation and thus the suppression of kinetic energy. Increasing the density of these bound states in WSe_2/$MoSe_2$ would result in achieving interlayer exciton condensation. Evidence of high-temperature exciton condensation also has been shown in the same heterostructure separated by a thin layer of tunneling barrier to lessen the effect of re-

combination of electron-hole pairs between layers. This is indeed a promising platform for further optical and transport studies to investigate Bose-Einstein condensation. However, there are some technical challenges. For instance, in order to study the BEC, separate gating and contacts to each layer are required to tune the carrier density in each layer. So far, the Platinum pre-pattern method discussed in chapter 2, has shown suitable contact to p-doped WSe_2, however, reliable contacts to n-doped $MoSe_2$ remain lacking. Contact engineering plays a critical role in the 2D field and can open up many avenues for further quantum studies in this heterobilayer. Another challenge to achieveg BEC in this heterobilayer is high-quality single crystals of both WSe_2 and $MoSe_2$. Even though the defect density may enhance the contact resistance, it can create bound states at various energies in conflict with the collective phenomena.

Another exciting idea for STM experiments is measuring twisted WSe_2 $MoSe_2$ with a gatable geometry to be able to tune the carrier density and detect the flat bands created by large moiré potential. Since the width of the band is small, low-temperature measurements are required to resolve the energy resolution. Nevertheless, low resistance contact to heterobilayer in open-face device geometry is so far lacking. Ideally, this geometry would permit us to simulate the Fermi-Hubbard model using $WSe_2/MoSe_2$ platform at various twist angles as the twist angle is a powerful tuning knob to control the interaction strength. Further, a double gate geometry can create an electric field to impact the correlated states as was shown in transport studies however the metallic tip and an open-face device interfere with this idea.

Another interesting measurement is studying quantum hall in $WSe_2/MoSe_2$. During my Ph.D., I was involved in this effort in collaboration with Prof. Dean's group. The idea is to detect the correlated states due to flat bands and large moiré potential. This heterobilayer is less complicated compared to twisted homobilayes; the Pt contact is only made to WSe_2 and as a result, all the carriers are populated in WSe_2. Therefore, $MoSe_2$ contribution is limited to the creation of moiré potential but can not host carriers as opposed to homobilayers. There are several obstacles along the way to conducting transport on such devices. In order to carry out quantum hall measurements at least four ohmic contacts are required but this is challenging at base temperature due to high

contact resistance. Another challenge is the large moiré wavelength is more susceptible to strain and inhomogeneity due to large lattice mismatch at small angles. Therefore, different areas of the sample behave differently. This results in a mix of all the states existing in the device and are extremely difficult to understand.

A promising future approach is studying exciton condensation in $WSe_2/MoSe_2$ by optical STM. Combining optical pumping with a powerful local probe such as STM allows us to detect moiré -dependent electronic states while exciton condensation occurs. There have been tremendous efforts to develop this technique for low-dimension physics however device geometry adds to the complexity of the experiment. Robust contacts to TMDs are required to gate the device at enough low temperature necessary for condensation. However, in open-face devices, it has been so far challenging without compromising the surface cleanness. Moreover, the interaction of the metallic tip with the surface is inevitable and can perturb the electronic states.

In chapter 4, we utilized $WSe_2/MoSe_2$ nanobubbles as a test bed to show deeply localized states at the boundary due to the highly doped area. This is a continuous change in band structure from the center of nanobubble to the edge. We provide a clear picture of local electronic states as well as emission energy using STM and near-field photoluminescence. Our finding shows TMD heterobilayers as excellent candidates to trap carriers for quantum emitters. Our theoretical calculations, self-consistent Schrodinger-Poisson, demonstrate strong doping, as well as strain, are responsible for the formation of deeply localized states. Our work provides a clear route to engineer material interface and achieves optical emitters, a crucial elements for a range of quantum information processors. An interesting direction by STM is studying the doping effect on the localized state in a more controllable way using electrostatic back gate and sharp interface. This would allow us to manipulate the energy position of the bound state by tuning the carrier density. One obstacle to tackle is making the contact to TMDs for gatable geometry and so far it has been challenging. Another interesting follow-up work would be measuring the exciton emission energy while performing STM measurements simultaneously which is an ongoing effort in our group.

In chapter 5, we investigated the effect of electric fields to achieve continuous band gap tuning

in a twisted TMD heterobilayer. We observe continuous band gap tuning up to ~400 meV change by sweeping the back gate to +(-) 70 V which was inaccessible in previous studies. In contrast, the Fermi level position remains almost unchanged in the presence of back gate voltage demonstrating a minor doping effect. The results of our study can be explained well by considering a finite tip size leading to an enhanced electric field. The results of this work can be transferred to other techniques, such as optical spectroscopy to access large electric fields necessary for numerous quantum studies. An interesting future study is measuring a gatable WSe_2/WS_2 heterobilayer using optical methods such as nano-PL to investigate the exciton energy as a function of back gate voltage. One can also leverage the results of this work and design a device with pre pattern graphite back gate to create a spatially tunable band gap to trap excitons.

In chapter 6, we revealed a sharp p-n Junction in graphene/α-$RuCl_3$ which is achieved within the 3 nm lateral length scale and 0.6 eV band offset. This results in a large electric field in the order of 10^8 V/m. This is one order of magnitude sharper than the previously reported results by back gate, adatoms, or ion implantation. In this study, we leverage the charge transfer between graphene and α-$RuCl_3$ due to work function difference and massive Dirac point shift. We investigated the nanobubbles as a test bed for p-n junctions by a multimessenger experimental approach, STM and s-SNOM. This work opens an opportunity for studying interfacial physics in graphene which requires sharp and clean junctions. One of these phenomena that is intriguing to study by STM is Veselago lensing which is the analogy of optical lenses in electronics. It has been theoretically predicted that a sharp p-n junction in graphene is responsible to focus the electron current on the other side of the junction. However, an abrupt change in carrier density at the interface is crucial to observe this phenomenon. Using the results we presented in this chapter, one can achieve the sharp junction in graphene using α-$RuCl_3$ charge transfer mechanism. Thin layers of h-BN can be also used as a spacer to adjust the charge transfer between graphene and α-$RuCl_3$ leading to a controllable p-n junction. And as a result of Veselago Lensing, we expect to detect the image of any defect or current flow on the other side of the interface. One important factor to consider to conduct the STM experiment on such devices is the interaction of the tip with the surface and

the tip interference with the electron trajectories. Nonetheless, accessing sharp p-n junctions in graphene using α-$RuCl_3$ is a promising platform for future research in this area.

In chapter 7, we utilized low-temperature scanning tunneling microscopy (STM) on a graphene/α-$RuCl_3$ heterostructure to validate the InterMatch method in predicting the charge transfer, strain, and stability of interfaces. By applying the InterMatch method to moiré patterns of graphene/α-$RuCl_3$, we successfully predicted the stable interface structure. Our STM topographs revealed three regions with distinct moiré wavelengths due to atomic reconstructions. We conducted a thorough exploration of the space of superlattice configurations and identified the energetically favorable superlattices that occur within a narrow range of twist angles, which is in agreement with the STM results. Furthermore, the spectra of these regions showed strong resonances, with the spacing between resonances following the expected pattern from Landau levels on a Dirac spectrum due to strain and doping. Our STM measurements demonstrate the effectiveness of the InterMatch method in predicting the charge transfer and stability of interfaces between materials. One promising avenue for further research is the investigation of the moiré physics in graphene/α-$RuCl_3$ using quantum transport measurements and detection of the resonances observed with STM. One can study the behavior of the resonances, which resemble a strong pseudo-magnetic field, and the dramatic effect they can have on the band structure of graphene.

In the latter part of this chapter, we examined the WSe_2/α-$RuCl_3$ heterostructure using various techniques. Our STM measurements on this heterostructure revealed a significant charge transfer between the two layers, resulting in the Fermi level shift to the valence band of WSe_2. Our optical measurements and DFT calculations confirmed the observations made by STM of a heavily p-doped WSe_2. These findings are encouraging and could potentially be used to address the contact problem of WSe_2 by leveraging interfacial physics and charge transfer. One possible solution is to utilize α-$RuCl_3$ as the contact electrodes to WSe_2, thereby achieving low-resistance contacts, which are essential for observing correlated states in WSe_2 bilayers. Achieving gate-tunable TMD devices with ohmic contact resistance will open routes toward the discovery of novel strongly correlated phenomena in these materials. I eagerly look forward to seeing how the field evolves by

leveraging these methods to solve contact problem in TMDs and access novel quantum systems in 2D semiconductors.

References

[1] K. S. Novoselov *et al.*, "Electric field effect in atomically thin carbon films," *science*, vol. 306, no. 5696, pp. 666–669, 2004.

[2] Y. Cao *et al.*, "Unconventional superconductivity in magic-angle graphene superlattices," *Nature*, vol. 556, no. 7699, pp. 43–50, 2018.

[3] Y. Cao *et al.*, "Correlated insulator behaviour at half-filling in magic-angle graphene superlattices," *Nature*, vol. 556, no. 7699, pp. 80–84, 2018.

[4] M. Yankowitz *et al.*, "Tuning superconductivity in twisted bilayer graphene," *Science*, vol. 363, no. 6431, pp. 1059–1064, 2019.

[5] D. J. Griffiths and D. F. Schroeter, *Introduction to quantum mechanics*. Cambridge university press, 2018.

[6] J. Bardeen, "Tunnelling from a many-particle point of view," *Physical review letters*, vol. 6, no. 2, p. 57, 1961.

[7] C. J. Chen, *Introduction to Scanning Tunneling Microscopy Third Edition*. Oxford University Press, USA, 2021, vol. 69.

[8] J. Tersoff and D. R. Hamann, "Theory of the scanning tunneling microscope," *Physical Review B*, vol. 31, no. 2, p. 805, 1985.

[9] W. C. Michels and N. L. Curtis, "A pentode lock-in amplifier of high frequency selectivity," *Review of Scientific Instruments*, vol. 12, no. 9, pp. 444–447, 1941.

[10] C. Cosens, "A balance-detector for alternating-current bridges," *Proceedings of the physical society*, vol. 46, no. 6, p. 818, 1934.

[11] G. Gautschi and G. Gautschi, *Piezoelectric sensors*. Springer, 2002.

[12] C. Wöll, S Chiang, R. Wilson, and P. Lippel, "Determination of atom positions at stacking-fault dislocations on au (111) by scanning tunneling microscopy," *Physical Review B*, vol. 39, no. 11, p. 7988, 1989.

[13] J. V. Barth, H. Brune, G. Ertl, and R. Behm, "Scanning tunneling microscopy observations on the reconstructed au (111) surface: Atomic structure, long-range superstructure, rotational domains, and surface defects," *Physical Review B*, vol. 42, no. 15, p. 9307, 1990.

[14] W Chen, V Madhavan, T Jamneala, and M. Crommie, "Scanning tunneling microscopy observation of an electronic superlattice at the surface of clean gold," *Physical Review Letters*, vol. 80, no. 7, p. 1469, 1998.

[15] K. F. Mak, C. Lee, J. Hone, J. Shan, and T. F. Heinz, "Atomically thin mos 2: A new direct-gap semiconductor," *Physical review letters*, vol. 105, no. 13, p. 136 805, 2010.

[16] W. Zhao *et al.*, "Evolution of electronic structure in atomically thin sheets of ws2 and wse2," *ACS nano*, vol. 7, no. 1, pp. 791–797, 2013.

[17] N. E. Staley, J. Wu, P. Eklund, Y. Liu, L. Li, and Z. Xu, "Electric field effect on superconductivity in atomically thin flakes of nbse 2," *Physical Review B*, vol. 80, no. 18, p. 184 505, 2009.

[18] A. Kundu, Z. B. Siu, and M. b. A. Jalil, "Ruderman-kittel-kasuya-yosida (rkky) interaction in weyl semimetals with tilted energy dispersion," *New Journal of Physics*, 2022.

[19] M. Bonilla *et al.*, "Strong room-temperature ferromagnetism in vse2 monolayers on van der waals substrates," *Nature nanotechnology*, vol. 13, no. 4, pp. 289–293, 2018.

[20] Z. Guguchia *et al.*, "Magnetism in semiconducting molybdenum dichalcogenides," *Science advances*, vol. 4, no. 12, eaat3672, 2018.

[21] A. Kogar *et al.*, "Signatures of exciton condensation in a transition metal dichalcogenide," *Science*, vol. 358, no. 6368, pp. 1314–1317, 2017.

[22] Z. Wang *et al.*, "Evidence of high-temperature exciton condensation in two-dimensional atomic double layers," *Nature*, vol. 574, no. 7776, pp. 76–80, 2019.

[23] C. Xu *et al.*, "Possible kitaev quantum spin liquid state in 2d materials with $S = 3/2$," *Phys. Rev. Lett.*, vol. 124, p. 087 205, 8 2020.

[24] M. Chhowalla, H. S. Shin, G. Eda, L.-J. Li, K. P. Loh, and H. Zhang, "The chemistry of two-dimensional layered transition metal dichalcogenide nanosheets," *Nature chemistry*, vol. 5, no. 4, pp. 263–275, 2013.

[25] A. Splendiani *et al.*, "Emerging photoluminescence in monolayer mos2," *Nano letters*, vol. 10, no. 4, pp. 1271–1275, 2010.

[26] A. F. Rigosi, H. M. Hill, K. T. Rim, G. W. Flynn, and T. F. Heinz, "Electronic band gaps and exciton binding energies in monolayer m o x w 1- x s 2 transition metal dichalcogenide alloys probed by scanning tunneling and optical spectroscopy," *Physical Review B*, vol. 94, no. 7, p. 075 440, 2016.

[27] C. Zhang *et al.*, "Probing critical point energies of transition metal dichalcogenides: Surprising indirect gap of single layer wse2," *Nano letters*, vol. 15, no. 10, pp. 6494–6500, 2015.

[28] M. M. Ugeda *et al.*, "Giant bandgap renormalization and excitonic effects in a monolayer transition metal dichalcogenide semiconductor," *Nature materials*, vol. 13, no. 12, pp. 1091–1095, 2014.

[29] M. Yankowitz, D. McKenzie, and B. J. LeRoy, "Local spectroscopic characterization of spin and layer polarization in wse 2," *Physical review letters*, vol. 115, no. 13, p. 136 803, 2015.

[30] X. Lu *et al.*, "Superconductors, orbital magnets and correlated states in magic-angle bilayer graphene," *Nature*, vol. 574, no. 7780, pp. 653–657, 2019.

[31] G. Chen *et al.*, "Evidence of a gate-tunable mott insulator in a trilayer graphene moiré superlattice," *Nature Physics*, vol. 15, no. 3, pp. 237–241, 2019.

[32] Y. Cao *et al.*, "Tunable correlated states and spin-polarized phases in twisted bilayer–bilayer graphene," *Nature*, vol. 583, no. 7815, pp. 215–220, 2020.

[33] C. Shen *et al.*, "Correlated states in twisted double bilayer graphene," *Nature Physics*, vol. 16, no. 5, pp. 520–525, 2020.

[34] L. Wang *et al.*, "Correlated electronic phases in twisted bilayer transition metal dichalcogenides," *Nature materials*, vol. 19, no. 8, pp. 861–866, 2020.

[35] A. L. Sharpe *et al.*, "Emergent ferromagnetism near three-quarters filling in twisted bilayer graphene," *Science*, vol. 365, no. 6453, pp. 605–608, 2019.

[36] M Serlin *et al.*, "Intrinsic quantized anomalous hall effect in a moiré heterostructure," *Science*, vol. 367, no. 6480, pp. 900–903, 2020.

[37] M. Yankowitz *et al.*, "Emergence of superlattice dirac points in graphene on hexagonal boron nitride," *Nature physics*, vol. 8, no. 5, pp. 382–386, 2012.

[38] A. Kerelsky *et al.*, "Maximized electron interactions at the magic angle in twisted bilayer graphene," *Nature*, vol. 572, no. 7767, pp. 95–100, 2019.

[39] E. J. Telford *et al.*, "Coupling between magnetic order and charge transport in a two-dimensional magnetic semiconductor," *Nature Materials*, vol. 21, no. 7, pp. 754–760, 2022.

[40] N. P. Wilson *et al.*, "Interlayer electronic coupling on demand in a 2d magnetic semiconductor," *Nature Materials*, vol. 20, no. 12, pp. 1657–1662, 2021.

[41] T. S. Ghiasi, A. A. Kaverzin, A. H. Dismukes, D. K. de Wal, X. Roy, and B. J. van Wees, "Electrical and thermal generation of spin currents by magnetic bilayer graphene," *Nature nanotechnology*, vol. 16, no. 7, pp. 788–794, 2021.

[42] D. Edelberg *et al.*, "Approaching the intrinsic limit in transition metal diselenides via point defect control," *Nano letters*, vol. 19, no. 7, pp. 4371–4379, 2019.

[43] H. Fang *et al.*, "Degenerate n-doping of few-layer transition metal dichalcogenides by potassium," *Nano letters*, vol. 13, no. 5, pp. 1991–1995, 2013.

[44] C. J. McClellan, E. Yalon, K. K. Smithe, S. V. Suryavanshi, and E. Pop, "Effective n-type doping of monolayer mos 2 by alo x," in *2017 75th annual device research conference (DRC)*, IEEE, 2017, pp. 1–2.

[45] H.-M. Li *et al.*, "Ultimate thin vertical p–n junction composed of two-dimensional layered molybdenum disulfide," *Nature communications*, vol. 6, no. 1, p. 6564, 2015.

[46] H.-J. Chuang *et al.*, "Low-resistance 2d/2d ohmic contacts: A universal approach to high-performance wse2, mos2, and mose2 transistors," *Nano letters*, vol. 16, no. 3, pp. 1896–1902, 2016.

[47] X. Cui *et al.*, "Multi-terminal transport measurements of mos2 using a van der waals heterostructure device platform," *Nature nanotechnology*, vol. 10, no. 6, pp. 534–540, 2015.

[48] Z. Wang, F. Liu, and M. Chou, "Fractal landau-level spectra in twisted bilayer graphene," *Nano letters*, vol. 12, no. 7, pp. 3833–3838, 2012.

[49] H. C. Movva *et al.*, "High-mobility holes in dual-gated wse2 field-effect transistors," *ACS nano*, vol. 9, no. 10, pp. 10 402–10 410, 2015.

[50] L. J. McGilly *et al.*, "Visualization of moiré superlattices," *Nature Nanotechnology*, vol. 15, no. 7, pp. 580–584, 2020.

[51] K. L. Seyler *et al.*, "Signatures of moiré-trapped valley excitons in mose 2/wse 2 heterobilayers," *Nature*, vol. 567, no. 7746, pp. 66–70, 2019.

[52] F. Wu, T. Lovorn, and A. H. MacDonald, "Theory of optical absorption by interlayer excitons in transition metal dichalcogenide heterobilayers," *Phys. Rev. B*, vol. 97, p. 035 306, 3 2018.

[53] H. Yu, G.-B. Liu, J. Tang, X. Xu, and W. Yao, "Moiré excitons: From programmable quantum emitter arrays to spin-orbit–coupled artificial lattices," *Science Advances*, vol. 3, no. 11, 2017.

[54] K. Tran *et al.*, "Evidence for moiré excitons in van der waals heterostructures," *Nature*, vol. 567, no. 7746, pp. 71–75, 2019.

[55] L. Wang *et al.*, "Correlated electronic phases in twisted bilayer transition metal dichalcogenides," *Nature materials*, pp. 1–6, 2020.

[56] J. Wang *et al.*, "Diffusivity reveals three distinct phases of interlayer excitons in $MoSe_2/WSe_2$ heterobilayers," *Phys. Rev. Lett.*, vol. 126, p. 106 804, 10 2021.

[57] L. A. Jauregui *et al.*, "Electrical control of interlayer exciton dynamics in atomically thin heterostructures," *Science*, vol. 366, no. 6467, pp. 870–875, 2019.

[58] E. C. Regan *et al.*, "Mott and generalized wigner crystal states in wse 2/ws 2 moiré superlattices," *Nature*, vol. 579, no. 7799, pp. 359–363, 2020.

[59] Z. Wang *et al.*, "Evidence of high-temperature exciton condensation in two-dimensional atomic double layers," *Nature*, vol. 574, no. 7776, pp. 76–80, 2019.

[60] F. Wu, T. Lovorn, E. Tutuc, and A. H. MacDonald, "Hubbard model physics in transition metal dichalcogenide moiré bands," *Phys. Rev. Lett.*, vol. 121, p. 026 402, 2 2018.

[61] Y. Zhang, N. F. Q. Yuan, and L. Fu, *Moiré quantum chemistry: Charge transfer in transition metal dichalcogenide superlattices*, 2019. arXiv: `1910.14061 [cond-mat.str-el]`.

[62] K. Tran *et al.*, "Evidence for moiré excitons in van der waals heterostructures," *Nature*, vol. 567, no. 7746, pp. 71–75, 2019.

[63] H. Yu, G.-B. Liu, J. Tang, X. Xu, and W. Yao, "Moiré excitons: From programmable quantum emitter arrays to spin-orbit–coupled artificial lattices," *Science advances*, vol. 3, no. 11, e1701696, 2017.

[64] D. A. Ruiz-Tijerina and V. I. Fal'ko, "Interlayer hybridization and moiré superlattice minibands for electrons and excitons in heterobilayers of transition-metal dichalcogenides," *Phys. Rev. B*, vol. 99, p. 125 424, 12 2019.

[65] C. Zhang *et al.*, "Interlayer couplings, moiré patterns, and 2d electronic superlattices in mos2/wse2 hetero-bilayers," *Science advances*, vol. 3, no. 1, e1601459, 2017.

[66] Y. Pan *et al.*, "Quantum-confined electronic states arising from the moiré pattern of mos2–wse2 heterobilayers," *Nano letters*, vol. 18, no. 3, pp. 1849–1855, 2018.

[67] Z. Zhang *et al.*, "Flat bands in twisted bilayer transition metal dichalcogenides," *Nature Physics*, pp. 1–4, 2020.

[68] H. Li *et al.*, *Imaging moiré flat bands in 3d reconstructed wse2/ws2 superlattices*, 2020. arXiv: 2007.06113 [cond-mat.mes-hall].

[69] M. R. Rosenberger *et al.*, "Twist angle-dependent atomic reconstruction and moiré patterns in transition metal dichalcogenide heterostructures," *ACS nano*, vol. 14, no. 4, pp. 4550–4558, 2020.

[70] A. Weston *et al.*, "Atomic reconstruction in twisted bilayers of transition metal dichalcogenides," *Nature Nanotechnology*, pp. 1–6, 2020.

[71] D. Halbertal *et al.*, *Moiré metrology of energy landscapes in van der waals heterostructures*, 2020. arXiv: 2008.04835 [cond-mat.mes-hall].

[72] I. Maity, P. K. Maiti, H. R. Krishnamurthy, and M. Jain, *Reconstruction of moiré lattices in twisted transition metal dichalcogenide bilayers*, 2019. arXiv: 1912.08702 [cond-mat.mtrl-sci].

[73] V. Enaldiev, V Zólyomi, C. Yelgel, S. Magorrian, and V. Fal'ko, "Stacking domains and dislocation networks in marginally twisted bilayers of transition metal dichalcogenides," *Physical Review Letters*, vol. 124, no. 20, p. 206 101, 2020.

[74] D. Edelberg, H. Kumar, V. Shenoy, H. Ochoa, and A. N. Pasupathy, "Tunable strain soliton networks confine electrons in van der waals materials," *Nature Physics*, pp. 1–6, 2020.

[75] Y. Bai *et al.*, "Excitons in strain-induced one-dimensional moiré potentials at transition metal dichalcogenide heterojunctions," *Nature Materials*, vol. 19, no. 10, pp. 1068–1073, 2020.

[76] M. H. Naik and M. Jain, "Ultraflatbands and shear solitons in moiré patterns of twisted bilayer transition metal dichalcogenides," *Phys. Rev. Lett.*, vol. 121, p. 266 401, 26 2018.

[77] J. Kang, J. Li, S.-S. Li, J.-B. Xia, and L.-W. Wang, "Electronic structural moiré pattern effects on mos2/mose2 2d heterostructures," *Nano letters*, vol. 13, no. 11, pp. 5485–5490, 2013.

[78] N. R. Wilson *et al.*, "Determination of band offsets, hybridization, and exciton binding in 2d semiconductor heterostructures," *Science Advances*, vol. 3, no. 2, 2017.

[79] S. Carr, D. Massatt, S. B. Torrisi, P. Cazeaux, M. Luskin, and E. Kaxiras, "Relaxation and domain formation in incommensurate two-dimensional heterostructures," *Physical Review B*, vol. 98, no. 22, p. 224 102, 2018.

[80] G. Kresse and J. Furthmüller, "Efficient iterative schemes for ab initio total-energy calculations using a plane-wave basis set," *Phys. Rev. B*, vol. 54, pp. 11 169–11 186, 16 1996.

[81] G. Kresse and D. Joubert, "From ultrasoft pseudopotentials to the projector augmented-wave method," *Phys. Rev. B*, vol. 59, pp. 1758–1775, 3 1999.

[82] S. Grimme, J. Antony, S. Ehrlich, and H. Krieg, "A consistent and accurate ab initio parametrization of density functional dispersion correction (dft-d) for the 94 elements h-pu," *The Journal of chemical physics*, vol. 132, no. 15, p. 154 104, 2010.

[83] J. P. Perdew, K. Burke, and M. Ernzerhof, "Generalized gradient approximation made simple," *Phys. Rev. Lett.*, vol. 77, pp. 3865–3868, 18 1996.

[84] J. Klimeš, D. R. Bowler, and A. Michaelides, "Van der waals density functionals applied to solids," *Physical Review B*, vol. 83, no. 19, p. 195 131, 2011.

[85] D. Halbertal *et al.*, "Moiré metrology of energy landscapes in van der waals heterostructures," *Nature communications*, vol. 12, no. 1, p. 242, 2021.

[86] D. Halbertal, S. Shabani, A. N. Passupathy, and D. Basov, "Extracting the strain matrix and twist angle from the moiré superlattice in van der waals heterostructures," *ACS nano*, vol. 16, no. 1, pp. 1471–1476, 2022.

[87] S. Carr, D. Massatt, S. B. Torrisi, P. Cazeaux, M. Luskin, and E. Kaxiras, "Relaxation and domain formation in incommensurate two-dimensional heterostructures," *Physical Review B*, vol. 98, no. 22, p. 224 102, 2018.

[88] S. Zhou, J. Han, S. Dai, J. Sun, and D. J. Srolovitz, "Van der waals bilayer energetics: Generalized stacking-fault energy of graphene, boron nitride, and graphene/boron nitride bilayers," *Physical Review B*, vol. 92, no. 15, p. 155 438, 2015.

[89] S. Shabani *et al.*, "Deep moiré potentials in twisted transition metal dichalcogenide bilayers," *Nature Physics*, vol. 17, no. 6, pp. 720–725, 2021.

[90] T. Benschop *et al.*, "Measuring local moiré lattice heterogeneity of twisted bilayer graphene," *Physical Review Research*, vol. 3, no. 1, p. 013 153, 2021.

[91] Y. Jiang *et al.*, "Visualizing strain-induced pseudomagnetic fields in graphene through an hbn magnifying glass," *Nano letters*, vol. 17, no. 5, pp. 2839–2843, 2017.

[92] Y. Bai *et al.*, "Excitons in strain-induced one-dimensional moiré potentials at transition metal dichalcogenide heterojunctions," *Nature Materials*, vol. 19, no. 10, pp. 1068–1073, 2020.

[93] M. R. Rosenberger *et al.*, "Twist angle-dependent atomic reconstruction and moiré patterns in transition metal dichalcogenide heterostructures," *ACS nano*, vol. 14, no. 4, pp. 4550–4558, 2020.

[94] S. Moore *et al.*, "Nanoscale lattice dynamics in hexagonal boron nitride moiré superlattices," *Nature Communications*, vol. 12, no. 1, p. 5741, 2021.

[95] K. Lee *et al.*, "Ultrahigh-resolution scanning microwave impedance microscopy of moiré lattices and superstructures," *Science advances*, vol. 6, no. 50, eabd1919, 2020.

[96] P. V. Nguyen *et al.*, "Visualizing electrostatic gating effects in two-dimensional heterostructures," *Nature*, vol. 572, no. 7768, pp. 220–223, 2019.

[97] L. A. Jauregui *et al.*, "Electrical control of interlayer exciton dynamics in atomically thin heterostructures," *Science*, vol. 366, no. 6467, pp. 870–875, 2019.

[98] H. Li *et al.*, "Optoelectronic crystal of artificial atoms in strain-textured molybdenum disulphide," *Nature communications*, vol. 6, no. 1, pp. 1–7, 2015.

[99] Y. Koo *et al.*, "Tip-induced nano-engineering of strain, bandgap, and exciton funneling in 2d semiconductors," *Advanced Materials*, vol. 33, no. 17, p. 2 008 234, 2021.

[100] K. Parto, S. I. Azzam, K. Banerjee, and G. Moody, "Defect and strain engineering of monolayer wse2 enables site-controlled single-photon emission up to 150 k," *Nature communications*, vol. 12, no. 1, pp. 1–8, 2021.

[101] D. J. Trainer, Y. Zhang, F. Bobba, X. Xi, S.-W. Hla, and M. Iavarone, "The effects of atomic-scale strain relaxation on the electronic properties of monolayer mos2," *ACS nano*, vol. 13, no. 7, pp. 8284–8291, 2019.

[102] M. Gabel, P. Z. El-Khoury, and Y. Gu, "Imaging charged exciton localization in van der waals wse2/mose2 heterobilayers," *The Journal of Physical Chemistry Letters*, vol. 12, no. 43, pp. 10 589–10 594, 2021.

[103] K. P. Dhakal *et al.*, "Local strain induced band gap modulation and photoluminescence enhancement of multilayer transition metal dichalcogenides," *Chemistry of Materials*, vol. 29, no. 12, pp. 5124–5133, 2017.

[104] A. Branny, S. Kumar, R. Proux, and B. D. Gerardot, "Deterministic strain-induced arrays of quantum emitters in a two-dimensional semiconductor," *Nature communications*, vol. 8, no. 1, pp. 1–7, 2017.

[105] C. Cho *et al.*, "Highly strain-tunable interlayer excitons in mos2/wse2 heterobilayers," *Nano letters*, vol. 21, no. 9, pp. 3956–3964, 2021.

[106] M. Turunen *et al.*, "Quantum photonics with layered 2d materials," *Nature Reviews Physics*, pp. 1–18, 2022.

[107] T. Chowdhury, K. Jo, S. B. Anantharaman, T. H. Brintlinger, D. Jariwala, and T. J. Kempa, "Anomalous room-temperature photoluminescence from nanostrained mose2 monolayers," *ACS Photonics*, vol. 8, no. 8, pp. 2220–2226, 2021.

[108] H. Lee *et al.*, "Inducing and probing localized excitons in atomically thin semiconductors via tip-enhanced cavity-spectroscopy," *Advanced Functional Materials*, vol. 31, no. 33, p. 2 102 893, 2021.

[109] Y. Luo, N. Liu, B. Kim, J. Hone, and S. Strauf, "Exciton dipole orientation of strain-induced quantum emitters in wse2," *Nano letters*, vol. 20, no. 7, pp. 5119–5126, 2020.

[110] S. Zhang *et al.*, "Nano-spectroscopy of excitons in atomically thin transition metal dichalcogenides," *Nature Communications*, vol. 13, no. 1, pp. 1–8, 2022.

[111] F. Liu, M. E. Ziffer, K. R. Hansen, J. Wang, and X. Zhu, "Direct determination of band-gap renormalization in the photoexcited monolayer mos 2," *Physical review letters*, vol. 122, no. 24, p. 246 803, 2019.

[112] K. Yao *et al.*, "Optically discriminating carrier-induced quasiparticle band gap and exciton energy renormalization in monolayer mos 2," *Physical Review Letters*, vol. 119, no. 8, p. 087 401, 2017.

[113] A. Chernikov, C. Ruppert, H. M. Hill, A. F. Rigosi, and T. F. Heinz, "Population inversion and giant bandgap renormalization in atomically thin ws 2 layers," *Nature Photonics*, vol. 9, no. 7, pp. 466–470, 2015.

[114] Y. Li *et al.*, "Measurement of the optical dielectric function of monolayer transition-metal dichalcogenides: Mos 2, mo s e 2, ws 2, and ws e 2," *Physical Review B*, vol. 90, no. 20, p. 205 422, 2014.

[115] T. I. Andersen *et al.*, "Excitons in a reconstructed moiré potential in twisted wse2/wse2 homobilayers," *Nature Materials*, vol. 20, no. 4, pp. 480–487, 2021.

[116] X. Wang *et al.*, "Moiré trions in mose2/wse2 heterobilayers," *Nature Nanotechnology*, vol. 16, no. 11, pp. 1208–1213, 2021.

[117] Z. Zhang *et al.*, "Correlated interlayer exciton insulator in double layers of monolayer wse2 and moir\'e ws2/wse2," *arXiv preprint arXiv:2108.07131*, 2021.

[118] T. P. Darlington *et al.*, "Imaging strain-localized excitons in nanoscale bubbles of monolayer wse2 at room temperature," *Nature Nanotechnology*, vol. 15, no. 10, pp. 854–860, 2020.

[119] C. Carmesin *et al.*, "Quantum-dot-like states in molybdenum disulfide nanostructures due to the interplay of local surface wrinkling, strain, and dielectric confinement," *Nano letters*, vol. 19, no. 5, pp. 3182–3186, 2019.

[120] L Chirolli, E Prada, F Guinea, R Roldán, and P San-Jose, "Strain-induced bound states in transition-metal dichalcogenide bubbles," *2D Materials*, vol. 6, no. 2, p. 025 010, 2019.

[121] D. J. Morrow and X. Ma, "Trapping interlayer excitons in van der waals heterostructures by potential arrays," *Phys. Rev. B*, vol. 104, pp. 195 302–195 312, 19 2021.

[122] D. Edelberg *et al.*, "Approaching the intrinsic limit in transition metal diselenides via point defect control," *Nano letters*, vol. 19, no. 7, pp. 4371–4379, 2019.

[123] S. Son *et al.*, "Strongly adhesive dry transfer technique for van der waals heterostructure," *2D Materials*, vol. 7, no. 4, p. 041 005, 2020.

[124] W.-T. Hsu *et al.*, "Second harmonic generation from artificially stacked transition metal dichalcogenide twisted bilayers," *ACS nano*, vol. 8, no. 3, pp. 2951–2958, 2014.

[125] P. Z. El-Khoury and Z. D. Schultz, "From sers to ters and beyond: Molecules as probes of nanoscopic optical fields," *The Journal of Physical Chemistry C*, vol. 124, no. 50, pp. 27 267–27 275, 2020.

[126] A. V. Tyurnina *et al.*, "Strained bubbles in van der waals heterostructures as local emitters of photoluminescence with adjustable wavelength," *ACS photonics*, vol. 6, no. 2, pp. 516–524, 2019.

[127] L. Sigl *et al.*, "Optical dipole orientation of interlayer excitons in mose 2- wse 2 heterostacks," *Physical Review B*, vol. 105, no. 3, p. 035 417, 2022.

[128] H. Su *et al.*, "Dark-exciton driven energy funneling into dielectric inhomogeneities in two-dimensional semiconductors," *Nano Letters*, vol. 22, no. 7, pp. 2843–2850, 2022.

[129] M. G. Harats, J. N. Kirchhof, M. Qiao, K. Greben, and K. I. Bolotin, "Dynamics and efficient conversion of excitons to trions in non-uniformly strained monolayer ws2," *Nature Photonics*, vol. 14, no. 5, pp. 324–329, 2020.

[130] H. Lee *et al.*, "Drift-dominant exciton funneling and trion conversion in 2d semiconductors on the nanogap," *Science advances*, vol. 8, no. 5, p. 5236, 2022.

[131] H. C. Kamban and T. G. Pedersen, "Interlayer excitons in van der waals heterostructures: Binding energy, stark shift, and field-induced dissociation," *Scientific reports*, vol. 10, no. 1, pp. 1–10, 2020.

[132] A. Bussy, G. Pizzi, and M. Gibertini, "Strain-induced polar discontinuities in two-dimensional materials from combined first-principles and schrödinger-poisson simulations," *Physical Review B*, vol. 96, no. 16, p. 165 438, 2017.

[133] A. Kormányos *et al.*, "K· p theory for two-dimensional transition metal dichalcogenide semiconductors," *2D Materials*, vol. 2, no. 2, p. 022 001, 2015.

[134] K.-A. N. Duerloo, M. T. Ong, and E. J. Reed, "Intrinsic piezoelectricity in two-dimensional materials," *The Journal of Physical Chemistry Letters*, vol. 3, no. 19, pp. 2871–2876, 2012.

[135] K. Li *et al.*, "Morphology deformation and giant electronic band modulation in long-wavelength ws2 moiré superlattices," *Nano Letters*, vol. 22, no. 14, pp. 5997–6003, 2022, PMID: 35839083. eprint: https://doi.org/10.1021/acs.nanolett.2c02418.

[136] D. J. Rizzo *et al.*, "Nanometer-scale lateral p–n junctions in graphene/-rucl3 heterostructures," *Nano Letters*, vol. 22, no. 5, pp. 1946–1953, 2022, PMID: 35226804.

[137] J. Balgley *et al.*, "Ultra-sharp lateral pn junctions in modulation-doped graphene," *arXiv preprint arXiv:2203.06295*, 2022.

[138] X. Wu, D. Vanderbilt, and D. Hamann, "Systematic treatment of displacements, strains, and electric fields in density-functional perturbation theory," *Physical Review B*, vol. 72, no. 3, p. 035 105, 2005.

[139] V. Zatko *et al.*, "Band-gap landscape engineering in large-scale 2d semiconductor van der waals heterostructures," *ACS nano*, vol. 15, no. 4, pp. 7279–7289, 2021.

[140] K. Wang *et al.*, "Electrical control of charged carriers and excitons in atomically thin materials," *Nature nanotechnology*, vol. 13, no. 2, pp. 128–132, 2018.

[141] M. R. Molas, K. Nogajewski, A. O. Slobodeniuk, J. Binder, M. Bartos, and M. Potemski, "The optical response of monolayer, few-layer and bulk tungsten disulfide," *Nanoscale*, vol. 9, no. 35, pp. 13 128–13 141, 2017.

[142] A. Arora, K. Nogajewski, M. Molas, M. Koperski, and M. Potemski, "Exciton band structure in layered mose 2: From a monolayer to the bulk limit," *Nanoscale*, vol. 7, no. 48, pp. 20 769–20 775, 2015.

[143] E. Del Corro *et al.*, "Excited excitonic states in 1l, 2l, 3l, and bulk wse2 observed by resonant raman spectroscopy," *Acs Nano*, vol. 8, no. 9, pp. 9629–9635, 2014.

[144] A Chaves *et al.*, "Bandgap engineering of two-dimensional semiconductor materials," *npj 2D Materials and Applications*, vol. 4, no. 1, pp. 1–21, 2020.

[145] M. Kang *et al.*, "Universal mechanism of band-gap engineering in transition-metal dichalcogenides," *Nano letters*, vol. 17, no. 3, pp. 1610–1615, 2017.

[146] S. Shabani *et al.*, "Ultralocalized optoelectronic properties of nanobubbles in 2d semiconductors," *Nano Letters*, vol. 22, no. 18, pp. 7401–7407, 2022.

[147] A. Ciarrocchi, D. Unuchek, A. Avsar, K. Watanabe, T. Taniguchi, and A. Kis, "Polarization switching and electrical control of interlayer excitons in two-dimensional van der waals heterostructures," *Nature photonics*, vol. 13, no. 2, pp. 131–136, 2019.

[148] Z. Qiu *et al.*, "Giant gate-tunable bandgap renormalization and excitonic effects in a 2d semiconductor," *Science advances*, vol. 5, no. 7, eaaw2347, 2019.

[149] D. Thureja *et al.*, "Electrically tunable quantum confinement of neutral excitons," *Nature*, vol. 606, no. 7913, pp. 298–304, 2022.

[150] J. Klein *et al.*, "Controlling exciton many-body states by the electric-field effect in monolayer mos 2," *Physical Review Research*, vol. 3, no. 2, p. L022009, 2021.

[151] Y. Tang *et al.*, "Tuning layer-hybridized moiré excitons by the quantum-confined stark effect," *Nature Nanotechnology*, vol. 16, no. 1, pp. 52–57, 2021.

[152] S. Gao and L. Yang, "Renormalization of the quasiparticle band gap in doped two-dimensional materials from many-body calculations," *Physical Review B*, vol. 96, no. 15, p. 155 410, 2017.

[153] G. Kresse and J. Hafner, "Ab initio molecular dynamics for liquid metals," *Physical review B*, vol. 47, no. 1, p. 558, 1993.

[154] P. E. Blöchl, "Projector augmented-wave method," *Physical review B*, vol. 50, no. 24, p. 17 953, 1994.

[155] J. P. Perdew, K. Burke, and M. Ernzerhof, "Generalized gradient approximation made simple," *Physical review letters*, vol. 77, no. 18, p. 3865, 1996.

[156] J. Klimeš, D. R. Bowler, and A. Michaelides, "Van der waals density functionals applied to solids," *Physical Review B*, vol. 83, no. 19, p. 195 131, 2011.

[157] C. Beenakker, "Specular andreev reflection in graphene," *Physical review letters*, vol. 97, no. 6, p. 067 007, 2006.

[158] A Ossipov, M Titov, and C. W. Beenakker, "Reentrance effect in a graphene n- p- n junction coupled to a superconductor," *Physical Review B*, vol. 75, no. 24, p. 241 401, 2007.

[159] Y. Zhao *et al.*, "Creating and probing electron whispering-gallery modes in graphene," *Science*, vol. 348, no. 6235, pp. 672–675, 2015.

[160] T. L. Le and V. L. Nguyen, "Quantitative study of electronic whispering gallery modes in electrostatic-potential induced circular graphene junctions," *Journal of Physics: Condensed Matter*, vol. 32, no. 25, p. 255 502, 2020.

[161] J. Lee *et al.*, "Imaging electrostatically confined dirac fermions in graphene quantum dots," *Nature Physics*, vol. 12, no. 11, pp. 1032–1036, 2016.

[162] C. Gutiérrez, L. Brown, C.-J. Kim, J. Park, and A. N. Pasupathy, "Klein tunnelling and electron trapping in nanometre-scale graphene quantum dots," *Nature Physics*, vol. 12, no. 11, pp. 1069–1075, 2016.

[163] C. Gutiérrez *et al.*, "Interaction-driven quantum hall wedding cake–like structures in graphene quantum dots," *Science*, vol. 361, no. 6404, pp. 789–794, 2018.

[164] J. Velasco Jr *et al.*, "Visualization and control of single-electron charging in bilayer graphene quantum dots," *Nano letters*, vol. 18, no. 8, pp. 5104–5110, 2018.

[165] J. M. Pereira Jr, V Mlinar, F. Peeters, and P Vasilopoulos, "Confined states and direction-dependent transmission in graphene quantum wells," *Physical Review B*, vol. 74, no. 4, p. 045 424, 2006.

[166] V. V. Cheianov, V. Fal'ko, and B. Altshuler, "The focusing of electron flow and a veselago lens in graphene pn junctions," *Science*, vol. 315, no. 5816, pp. 1252–1255, 2007.

[167] G.-H. Lee, G.-H. Park, and H.-J. Lee, "Observation of negative refraction of dirac fermions in graphene," *Nature Physics*, vol. 11, no. 11, pp. 925–929, 2015.

[168] L. Xiong *et al.*, "Photonic crystal for graphene plasmons," *Nature communications*, vol. 10, no. 1, p. 4780, 2019.

[169] X. Zhou *et al.*, "Atomic-scale characterization of graphene p–n junctions for electron-optical applications," *ACS nano*, vol. 13, no. 2, pp. 2558–2566, 2019.

[170] B. Özyilmaz, P. Jarillo-Herrero, D. Efetov, and P. Kim, "Electronic transport in locally gated graphene nanoconstrictions," *Applied Physics Letters*, vol. 91, no. 19, p. 192 107, 2007.

[171] P. Willke *et al.*, "Doping of graphene by low-energy ion beam implantation: Structural, electronic, and transport properties," *Nano letters*, vol. 15, no. 8, pp. 5110–5115, 2015.

[172] G. Wang *et al.*, "Seamless lateral graphene p–n junctions formed by selective in situ doping for high-performance photodetectors," *Nature Communications*, vol. 9, no. 1, p. 5168, 2018.

[173] C. Praveen, S. Piccinin, and S. Fabris, "Adsorption of alkali adatoms on graphene supported by the au/ni (111) surface," *Physical Review B*, vol. 92, no. 7, p. 075 403, 2015.

[174] C. R. Dean *et al.*, "Boron nitride substrates for high-quality graphene electronics," *Nature nanotechnology*, vol. 5, no. 10, pp. 722–726, 2010.

[175] Y. Zhang *et al.*, "Giant phonon-induced conductance in scanning tunnelling spectroscopy of gate-tunable graphene," *Nature Physics*, vol. 4, no. 8, pp. 627–630, 2008.

[176] S. Biswas, Y. Li, S. M. Winter, J. Knolle, and R. Valentí, "Electronic properties of α- rucl 3 in proximity to graphene," *Physical Review Letters*, vol. 123, no. 23, p. 237 201, 2019.

[177] E. Gerber, Y. Yao, T. A. Arias, and E.-A. Kim, "Ab initio mismatched interface theory of graphene on α- rucl 3: Doping and magnetism," *Physical Review Letters*, vol. 124, no. 10, p. 106 804, 2020.

[178] D. J. Rizzo *et al.*, "Charge-transfer plasmon polaritons at graphene/α-rucl3 interfaces," *Nano letters*, vol. 20, no. 12, pp. 8438–8445, 2020.

[179] B. Zhou, J Balgley, P. Lampen-Kelley, J.-Q. Yan, D. G. Mandrus, and E. A. Henriksen, "Evidence for charge transfer and proximate magnetism in graphene–α- rucl 3 heterostructures," *Physical Review B*, vol. 100, no. 16, p. 165 426, 2019.

[180] Y. Wang *et al.*, "Modulation doping via a two-dimensional atomic crystalline acceptor," *Nano letters*, vol. 20, no. 12, pp. 8446–8452, 2020.

[181] S. Mashhadi *et al.*, "Spin-split band hybridization in graphene proximitized with α-rucl3 nanosheets," *Nano letters*, vol. 19, no. 7, pp. 4659–4665, 2019.

[182] A. F. May, J. Yan, and M. A. McGuire, "A practical guide for crystal growth of van der waals layered materials," *Journal of Applied Physics*, vol. 128, no. 5, p. 051 101, 2020.

[183] M. Crommie, C. P. Lutz, and D. Eigler, "Imaging standing waves in a two-dimensional electron gas," *Nature*, vol. 363, no. 6429, pp. 524–527, 1993.

[184] P. Roushan *et al.*, "Topological surface states protected from backscattering by chiral spin texture," *Nature*, vol. 460, no. 7259, pp. 1106–1109, 2009.

[185] G. Kresse and J. Furthmüller, "Efficient iterative schemes for ab initio total-energy calculations using a plane-wave basis set," *Physical review B*, vol. 54, no. 16, p. 11 169, 1996.

[186] X. Andrade *et al.*, "Real-space grids and the octopus code as tools for the development of new simulation approaches for electronic systems," *Physical Chemistry Chemical Physics*, vol. 17, no. 47, pp. 31 371–31 396, 2015.

[187] N. Tancogne-Dejean *et al.*, "Octopus, a computational framework for exploring light-driven phenomena and quantum dynamics in extended and finite systems," *The Journal of chemical physics*, vol. 152, no. 12, p. 124 119, 2020.

[188] N. Tancogne-Dejean, M. J. Oliveira, and A. Rubio, "Self-consistent dft+ u method for real-space time-dependent density functional theory calculations," *Physical Review B*, vol. 96, no. 24, p. 245 133, 2017.

[189] P. Khomyakov, A. Starikov, G Brocks, and P. J. Kelly, "Nonlinear screening of charges induced in graphene by metal contacts," *Physical Review B*, vol. 82, no. 11, p. 115 437, 2010.

[190] T Mueller, F Xia, M Freitag, J Tsang, P. Avouris, *et al.*, "Role of contacts in graphene transistors: A scanning photocurrent study," *Physical Review B*, vol. 79, no. 24, p. 245 430, 2009.

[191] A. K. Geim and I. V. Grigorieva, "Van der waals heterostructures," *Nature*, vol. 499, no. 7459, pp. 419–425, 2013.

[192] D. M. Kennes *et al.*, "Moiré heterostructures as a condensed-matter quantum simulator," *Nature Physics*, vol. 17, no. 2, pp. 155–163, Feb. 2021.

[193] H.-P. Komsa and A. V. Krasheninnikov, "Electronic structures and optical properties of realistic transition metal dichalcogenide heterostructures from first principles," *Physical Review B*, vol. 88, no. 8, p. 085 318, Aug. 2013, Publisher: American Physical Society.

[194] H. Terrones and M. Terrones, "Bilayers of transition metal dichalcogenides: Different stackings and heterostructures," *Journal of Materials Research*, vol. 29, no. 3, pp. 373–382, Feb. 2014.

[195] A. Ebnonnasir, B. Narayanan, S. Kodambaka, and C. V. Ciobanu, "Tunable MoS2 bandgap in MoS2-graphene heterostructures," *Applied Physics Letters*, vol. 105, no. 3, p. 031 603, Jul. 2014, Publisher: American Institute of Physics.

[196] M. Bokdam, T. Amlaki, G. Brocks, and P. J. Kelly, "Band gaps in incommensurable graphene on hexagonal boron nitride," *Phys. Rev. B*, vol. 89, p. 201 404, 20 2014.

[197] S. Zhou, J. Han, S. Dai, J. Sun, and D. J. Srolovitz, "Van der Waals bilayer energetics: Generalized stacking-fault energy of graphene, boron nitride, and graphene/boron nitride bilayers," *Physical Review B*, vol. 92, no. 15, p. 155 438, Oct. 2015.

[198] E. Gerber, Y. Yao, T. A. Arias, and E.-A. Kim, "Ab Initio Mismatched Interface Theory of Graphene on $\ensuremath{\alpha}\text{\ensuremath{-}}{\mathrm{RuCl}}_{3}$: Doping and Magnetism," *Physical Review Letters*, vol. 124, no. 10, p. 106 804, Mar. 2020.

[199] M. K. Horton, S. Dwaraknath, and K. A. Persson, "Promises and perils of computational materials databases," *Nature Computational Science*, vol. 1, no. 1, pp. 3–5, Jan. 2021.

[200] I. Levin, *NIST Inorganic Crystal Structure Database (ICSD)*, 2020.

[201] D. D. Landis *et al.*, "The computational materials repository," *Computing in Science Engineering*, vol. 14, no. 6, pp. 51–57, 2012.

[202] S. Curtarolo *et al.*, "Aflowlib.org: A distributed materials properties repository from high-throughput ab initio calculations," *Computational Materials Science*, vol. 58, pp. 227–235, 2012.

[203] A. Jain *et al.*, "Commentary: The Materials Project: A materials genome approach to accelerating materials innovation," *APL Materials*, vol. 1, no. 1, p. 011 002, Jul. 2013.

[204] J. E. Saal, S. Kirklin, M. Aykol, B. Meredig, and C. Wolverton, "Materials design and discovery with high-throughput density functional theory: The open quantum materials database (oqmd)," *JOM*, vol. 65, no. 11, pp. 1501–1509, 2013.

[205] M. de Jong *et al.*, "Charting the complete elastic properties of inorganic crystalline compounds," *Scientific Data*, vol. 2, no. 1, p. 150 009, 2015.

[206] M. Ashton, J. Paul, S. B. Sinnott, and R. G. Hennig, "Topology-Scaling Identification of Layered Solids and Stable Exfoliated 2D Materials," *Physical Review Letters*, vol. 118, no. 10, p. 106 101, Mar. 2017.

[207] S. Haastrup *et al.*, "The Computational 2D Materials Database: High-throughput modeling and discovery of atomically thin crystals," *2D Materials*, vol. 5, no. 4, p. 042 002, Sep. 2018.

[208] J. Zhou *et al.*, "2DMatPedia, an open computational database of two-dimensional materials from top-down and bottom-up approaches," *Scientific Data*, vol. 6, no. 1, p. 86, Jun. 2019.

[209] C. Draxl and M. Scheffler, "The NOMAD laboratory: From data sharing to artificial intelligence," *Journal of Physics: Materials*, vol. 2, no. 3, p. 036 001, 2019.

[210] L. Talirz *et al.*, "Materials cloud, a platform for open computational science," *Scientific Data*, vol. 7, no. 1, p. 299, 2020.

[211] K. Choudhary *et al.*, "The joint automated repository for various integrated simulations (jarvis) for data-driven materials design," *npj Computational Materials*, vol. 6, no. 1, p. 173, 2020.

[212] K. Mathew *et al.*, "MPInterfaces: A Materials Project based Python tool for high-throughput computational screening of interfacial systems," *Computational Materials Science*, vol. 122, pp. 183–190, Sep. 2016.

[213] H. Ding, S. S. Dwaraknath, L. Garten, P. Ndione, D. Ginley, and K. A. Persson, "Computational Approach for Epitaxial Polymorph Stabilization through Substrate Selection," *ACS Applied Materials & Interfaces*, vol. 8, no. 20, pp. 13 086–13 093, May 2016.

[214] K. Choudhary, K. F. Garrity, G. Pilania, and F. Tavazza, "Efficient Computational Design of 2D van der Waals Heterostructures: Band-Alignment, Lattice-Mismatch, Web-app Generation and Machine-learning," Apr. 2020.

[215] T. M. Boland and A. K. Singh, "Computational synthesis of 2d materials: A high-throughput approach to materials design," *Computational Materials Science*, vol. 207, p. 111 238, 2022.

[216] A. G. Milnes and D. L. Feucht, *Heterojunctions and metal-semiconductor junctions*. New York: Academic Press, 1972, ISBN: 0-12-498050-3.

[217] L. D. Landau, E. M. Lifshitž, J. B. Sykes, and W. H. Reid, "Course of Theoretical Physics: Theory of Elasticity," in *Course of Theoretical Physics: Theory of Elasticity*, Butterworth-Heinemann, 1986, ch. 2, pp. 46–58.

[218] P. Muller, "Glossary of terms used in physical organic chemistry (iupac recommendations 1994)," *Pure and Applied Chemistry*, vol. 66, no. 5, pp. 1077–1184, 1994.

[219] E. Kaxiras, *Atomic and Electronic Structure of Solids*. Cambridge University Press, 2003.

[220] Y. Wang *et al.*, "Modulation Doping via a Two-Dimensional Atomic Crystalline Acceptor," *Nano Lett.*, vol. 20, no. 12, pp. 8446–8452, Dec. 2020.

[221] J. Mao *et al.*, "Evidence of flat bands and correlated states in buckled graphene superlattices," *Nature*, vol. 584, no. 7820, pp. 215–220, 2020.

[222] D. J. Rizzo *et al.*, "Nanometer-scale lateral p–n junctions in graphene/α-rucl3 heterostructures," *Nano letters*, vol. 22, no. 5, pp. 1946–1953, 2022.

[223] H. B. Heersche, P. Jarillo-Herrero, J. B. Oostinga, L. M. Vandersypen, and A. F. Morpurgo, "Bipolar supercurrent in graphene," *Nature*, vol. 446, no. 7131, pp. 56–59, 2007.

[224] A. Chernikov *et al.*, "Exciton binding energy and nonhydrogenic rydberg series in monolayer ws 2," *Physical review letters*, vol. 113, no. 7, p. 076 802, 2014.

[225] D. Xiao, G.-B. Liu, W. Feng, X. Xu, and W. Yao, "Coupled spin and valley physics in monolayers of mos 2 and other group-vi dichalcogenides," *Physical review letters*, vol. 108, no. 19, p. 196 802, 2012.

[226] K. F. Mak and J. Shan, "Photonics and optoelectronics of 2d semiconductor transition metal dichalcogenides," *Nature Photonics*, vol. 10, no. 4, pp. 216–226, 2016.